UV RESONANCE RAMAN STUDY OF SOLUTION ENVIRONMENT EFFECT ON POLY-L-LYSINE CONFORMATION AND RESOLUTION ENHANCEMENT MECHANISM OF TWO DIMENSIONAL CORRELATION SPECTROSCOPY

by

Lu Ma

B.S., Zhejiang University, 2001

M.S., Zhejiang University, 2004

Submitted to the Graduate Faculty of the Kenneth P. Dietrich

School of Arts and Sciences in partial fulfillment

of the requirements for the degree of

Doctor of Philosophy

University of Pittsburgh

2011

UNIVERSITY OF PITTSBURGH

THE KENNETH P. DIETRICH SCHOOL OF ARTS AND SCIENCES

This dissertation was presented

by

Lu Ma

It was defended on

November, 29, 2011

and approved by

Lillian T. Chong, Assistant Professor, Department of Chemistry

Michael Trakselis, Assistant Professor, Department of Chemistry

Ronald Wetzel, Professor, Department of Structural Biology

Dissertation Advisor: Sanford A. Asher, Distinguished Professor, Department of Chemistry

UV RESONANCE RAMAN STUDY OF SOLUTION ENVIRONMENT EFFECT ON POLY-L-LYSINE CONFORMATION AND RESOLUTION ENHANCMENT MECHANISM OF TWO DIMENSIONAL CORRELATION SPECTROSCOPY

Lu Ma, PhD

University of Pittsburgh, 2011

How proteins fold into compact, highly ordered and functional three-dimensional structures continues to challenge the modern science. UV resonance Raman (UVRR) is one of the advanced technologies used to study protein folding problem. In this thesis, by using UVRR spectroscopy, we examined solution environment effect on poly-L-lysine (PLL) conformation in great detail.

We investigated the sidechain electrostatic control of PLL conformation by examining the PLL conformational dependence on pH, the presence of NaCl and $NaClO_4$, and temperature. At pH value below 7, PLL adopts the extended polyproline II (PPII) and 2.5_1-helix conformations. Increasing pH and the addition of $NaClO_4$ induces PLL to form a high content of α-helix-like conformations (α-helix, π-bulge/helix and turn structures) by decreasing the sidechain electrostatic repulsion. In contrast to $NaClO_4$, we found that high concentrations of NaCl has negligible impact on the PLL conformation at low pH. Utilizing UVRR, we also quantitatively tracked temperature and $NaClO_4$ concentration induced conformation changes of PLL. We experimentally determined the conformational population distributions and the energy landscape of PLL along the Ramachandran Ψ angle under different solution conditions.

We measured the $NaClO_4$ concentration dependence of PLL amide hydrogen exchange kinetics at pH 2.8 using UVRR spectroscopy. We found $NaClO_4$ slows the hydrogen exchange rates for the extended conformations and conformational exchange rates between the extended and α-helix-like conformations. We proposed a $NaClO_4$ protection mechanism.

This thesis also includes the study of the resolution enhancement mechanism of generalized two-dimensional correlation spectroscopy (2D COS). Despite extensive study, the origin of the 2D COS spectral patterns for overlapping bands and the resolution enhancement mechanisms are not completely understood. By using the simulation method, we elucidated the origin of 2D COS spectral features and identified the conditions to resolve overlapping bands.

TABLE OF CONTENTS

LIST OF TABLES

LIST OF FIGURES

ACKNOWLEDGMENTS

I would like to express my sincere thanks to everyone who has contributed directly or indirectly to the successful completion of my graduate studies. I would like to start the list by thanking my advisor Professor Sanford Asher for his continuous support and insightful guidance. He has given me great flexibility and provided an excellent working environment for doing research. Dr. Asher is also such a serious and energetic scientist. What I have learned from him will continue to shape me for the rest of my life.

I would like to express my special thanks to Professor Michael Trakselis for his guidance on my proposal. He gave me a lot of helpful instructions and advices from which I will benefit in future. I would like to thank Professor David Pratt for his instructions and helpful discussions during my study. Many thanks for Professor Lillian Chong and her graduate student Reza Salari, who helped do the theoretical calculation.

Special thanks for Vitali Sikirzhytski and Professor Igor Lednev at SUNY Albany. Their help is critical for successful completion of my 2D COS paper. I would like to thank to Dr. Zeeshan Ahmed, Dr. Alexsandr Mikhonin, Dr. Bhavya Sharma, Dr. Sergei Bykov, Dr. Nataliya Myshakina, Dr. Sasha Tikhonov and Zhenmin Hong for their generous helps on my research. I have benefited so much from them. I would especially like to thank Sharon Mansfield and John Jockovitz who are always ready to help. I also want to thank our current

group members who provide a great research environment. It is very enjoyable to work with them.

Finally, I owe my deepest thanks to my husband, Dr. Luyan Sun. He has always been understanding and supportive of me and my work. Last, and most importantly, I would like to thank my parents, who give me unconditional support for my education and for my life.

1.0 THE PROTEIN FOLDING PROBLEM

Proteins are important biological macromolecules that are encoded in the DNA sequences. Proteins are involved in a wide range of fundamental biological processes such as biochemical catalysis, transport and energy transduction. Structurally, proteins are linear polymers composed of amino acids. Under physiological conditions of pH and temperature, most proteins fold into a unique, highly ordered, and compact structure. Despite more than half century of active study, the question of how and why proteins fold remains one of the major unsolved problems in biophysical chemistry. Interest in this problem has greatly increased since the realization that many diseases are caused by misfolded protein, such as Alzheimer, Parkinson, Creutzfeld Jakob syndrome, type II diabetes, mad cow disease and many others.[1-6] Understanding how proteins fold is also of fundamental importance for proteomic and structural genomics of proteins. As a result, protein folding problem remains one of the hot spots of current research. In 2005, *Science* named the protein folding problem one of the biggest unsolved problems in science.[7]

1.1 SECONDARY STRUCTURES OF PROTEINS

Four levels are considered to describe the protein structure. The primary structure of a polypeptide is the amino acid sequence from amino-terminus to carboxyl-terminus. The

secondary structure is the local spatial arrangement of its main-chain atoms without regard to the conformation of its side chains. Association of secondary structural elements in single protein molecule results the tertiary structure. Quaternary structure is a larger assembly of several protein molecules or polypeptide chains. The quaternary structure is stabilized by noncovalent interactions and disulfide bonds.

The conformation of a polypeptide backbone is specified by the torsion angle pairs (Φ,Ψ) for each residue. Because C-N bonds have partial double bond character due to resonance of O=C-N-, so the O=C-N are almost a planar, and rotation barrier about the (O)C-N bond is high. The only bonds which can rotate freely are the N-C_α bond and C_α-C bonds, whose rotation dihedral angels are denoted Φ and Ψ (Fig. 1.1), respectively. Thus, the Φ and Ψ dihedral angles are the two structural coordinators which determine the backbone conformation of a polypeptide. The plot of the favored Ψ, Φ combination in rectangular coordinates is called the conformational map, or the Ramachandran diagram. (Fig. 1.2) This representation is used principally in the studies of conformational restrictions and preferences.

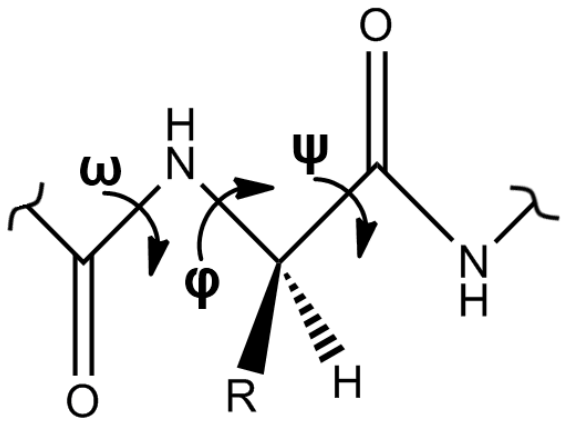

Figure 1.1. The schematic geometry of a polypeptide backbone. Reproduced from http://www.quora.com/Why-are-most-alpha-helices-in-proteins-right-handed.

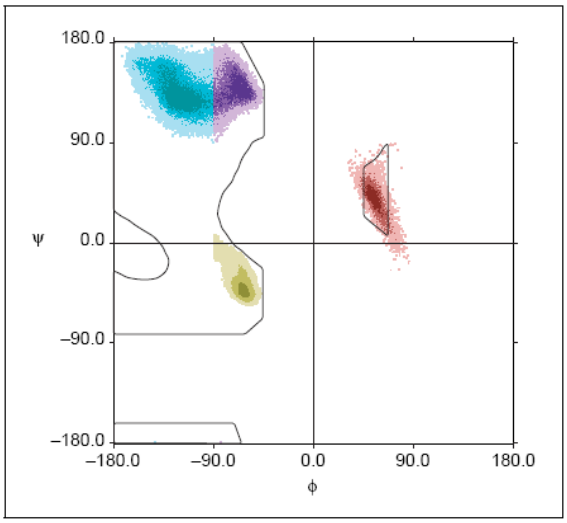

Figure 1.2. Ramachandran plot of alanine dipeptide. α, yellow; β, blue; PPII purple; αL, red. Reproduced from Fitzkee *et al.*[8]

There are three common secondary structures in proteins, namely helices, beta sheets, and turns. Secondary structure provides the information of protein backbone conformations, and the formation of secondary structure is one of the most important and fundamental element of the protein folding puzzle.

1.1.1 α, π, 3_{10}-Helix

Helix is one main group in all types of secondary structures. Originally, a number of possible helix types were proposed, including α (3.6_{13}), γ (5.1_{17}), π (4.4_{16}), 2.2_7, 3_{10}, and 4.3_{14}, where the format $\boldsymbol{r_m}$ denotes a structure having *r* residues and *m* atoms per turn. Of all the hypothesized helix types, only the α, 3_{10}, and π-helix have been observed in protein

structures. The main stabilizing factor for helical structures is the repeating hydrogen bonding between main chain carbonyl oxygen and amide hydrogen groups.

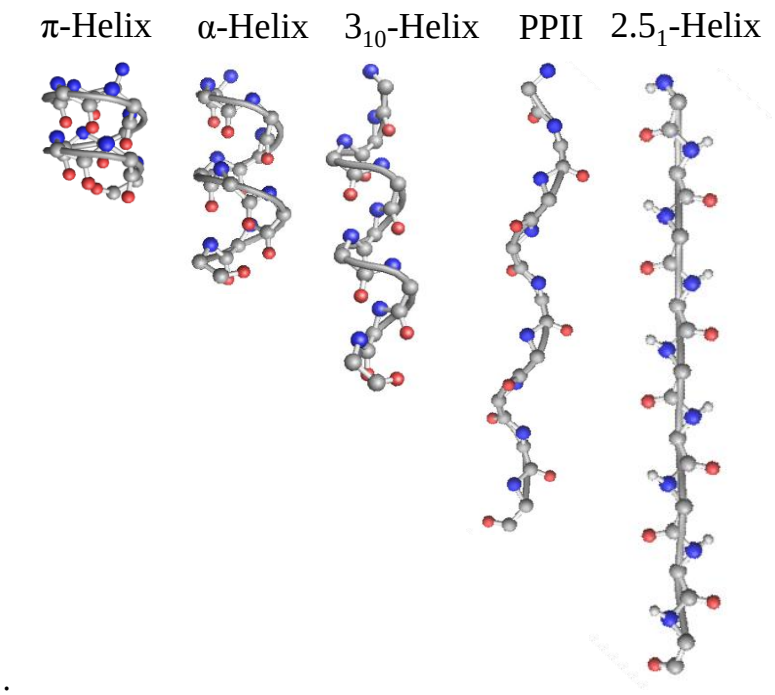

Figure 1.3. The backbone conformations of peptide.

The α-helices are the best known and most easily recognized structure. It was first described by Pauling, Corey and Branson.[9] Their model of the α-helix was soon supported by the X-ray analysis of hemoglobin by Perutz.[10] In protein crystals, ~31% of amino acid residues are in alpha helical structures. The i→i-4 backbone hydrogen bonding pattern is adopted by α-helix, which is defined by the amide hydrogen bond donor (i) and the carbonyl hydrogen bond acceptor (i-4). The average dihedral angles are Φ =-57° and Ψ =-47°.

3_{10}-helices, with i→i-3 hydrogen bonding, are much less common than α-helices, and ~3% of amino acid residues are in 3_{10}-helices.[11,12] The majority of 3_{10}-helices are very short, with 96% having no more than four residues. Survey of known protein crystal structures

shows that the 3_{10}-helix conformation is favorable for structures connecting two β-stands, but unfavorable for structures connecting α-helices and β-stands.[11] The 3_{10}-helices observed in proteins show a wide spread in the residue Φ, Ψ angles.[11,13] The standard Φ, Ψ angles of 3_{10}-helix are -49°, and -26°, respectively (Perutz).[10]

Recently, there has been renewed interest in the interconversion between 3_{10}-helix and α-helix.[14,15] Experimental work suggests that 3_{10}-helix is formed early in the folding of α-helix.[16,17] Some of the first evidence for 3_{10}-helix as a folding intermediate in the formation of an α-helix was suggested by Sundaralingam and Sekharudu.[18] Theoretical studies also provides support of the proposal of the 3_{10}-helix as a thermodynamic intermediate in a-helix folding.[19,20] Again, the transition between 3_{10}-helix and α-helix appears to play a role in the protein folding.

The third helical form is π-helix with Φ= -57°, Ψ= -70°. Early studies showed very limited experimental evidence for the existence of π-helix. The rarity of the π-helix has been attributed to its instability due to the following properties: (1) the dihedral angles are unfavorable, lying at the very edge of an allowed minimum energy region of the Ramanchandran plot; (2) the larger radius of the π-helix means that the main chain atoms are no longer in van der Waal contact along the helix axis; (3) a large entropic cost is required to form a helix in which five residues need to be aligned to permit the i→i-5 hydrogen bond.[21]

The existence of a left handed π-helical structure was inferred first from the infrared spectra of thin film of poly(beta phenetyl-L-aspartate).[22] It has been proposed that peptides in lipid vesicles or membranes might form π-helical structures.[23] Recently, Weaver identified 10 protein structures in which π-helical turns occur.[24] Fodje and Al-karadaghi

identified 104 π-helices in 936 high resolution structures.[21] Hence, these helices are not as rare as once thought.

Recently, the presence of the π-helix has been found in several molecular dynamic simulations.[25-27] For example, $(AAXAA)_3$ peptide forms π-helical hydrogen bonding patterns with a preference for particular amino acid.[28] The stabilization of the i→i-5 hydrogen bonds could be attributed to water bridged side chain interactions or hydrophobic interaction between stacked side chains. This suggests that the π-helix is not as unstable as previously believed.

1.1.2 PPII and Random Coil

The random coil is the state in which the conformation of any one peptide group is uncorrelated with any other in the chain, particularly its neighbours.[8,29,30] All polypeptide conformations are equally likely, equally accessible, and of equal energy. In a random coil, the energy difference among sterically accessible backbone conformers are on the order of kT. The energy landscape appears essentially featureless, and a Boltzmann-weighted ensemble of such polymers would populate this landscape uniformly.

Tanford's pioneering experiments on denatured proteins in 6 M guanidinium chloride were interpreted by using the random coil model, and they anchored a widespread belief that denatured proteins are structureless chains.[31] The random coil model has been applied to studies of backbone conformations in denatured states. However, one can imagine that the energy differences between major backbone conformations are sufficiently large to favor one conformation over others, and random coil state is almost certainly never found for any polypeptide in water. It has been now realized that random coil hypothesis or Flory's

isolated-pair hypothesis that each pair of side chains are sterically independent breaks down in parts of the dipeptide map.[32,33] And specifically, it has been found three or more residues in the α-helix region of Φ, Ψ space cannot be followed immediately by a residue from the β/PPII region without encountering a steric clash (Fig. 1.4).[34] Such local steric restrictions decrease the conformational space greatly.

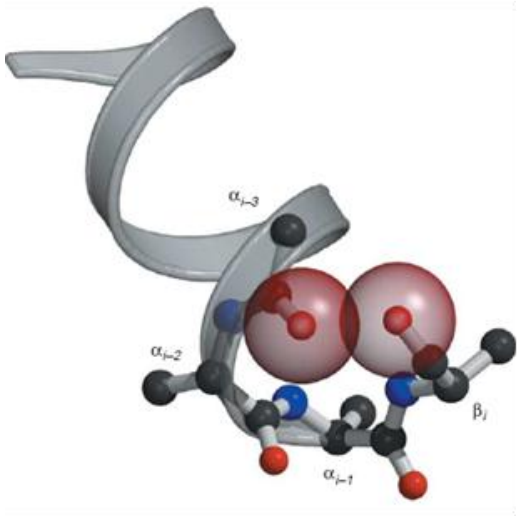

Figure 1.4. A β residue cannot follow three or more residues of α-helix without encountering a steric clash between the oxygen atoms at ith and i+3 positions. Reproduced from Fitzkee and Rose.[34]

The polyproline II (PPII) structure is a left-handed 3_1-helix with ideal backbone dihedral angles around Φ=-75° and Ψ=+145°, resulting in an axial translation of 3.20 Å. The name of 'polyproline helix' was motivated by the fact that collagen peptides, which are rich in proline, adopt this conformation, but PPII is certainly not restricted to proline residues.

Unlike α-helices, PPII helices do not participate in intra-segment or inter-segment hydrogen bonds. The stability of PPII conformation results from peptide-water hydrogen bonds, the chain entropy which is maximized in the PPII conformation, and the minimum disruption of the solvent structure.[35-39]

Recently, several lines of compelling evidence have converged to reveal that the backbone conformation of unfolded protein is predisposed to PPII conformation.[33,40-44] It has been shown using NMR and CD spectroscopy that seven-residue alanine peptide adopts the PPII conformation in an aqueous environment, which was believed to be random coil previously.[45,46] Moreover, it has been found that one-third of the coil library are composed of individual residues adopting PPII backbone conformation.[47]

The presence of defined localized structure in the backbone conformation of unfolded proteins has far-reaching implications for the protein folding problem. It suggests that the structure of unfolded protein is less heterogeneous than has been thought previously and that the backbone entropy in unfolded states is much lower than that implied by the random coil model.

1.2 PROTEIN FOLDING THEORIES

The impetus for protein folding research stems from two of the most well-known theories of protein folding: Anfinsen dogma and the Levinthal Paradox. In 1969, Anfinsen et al. demonstrated that ribonuclease A can spontaneously refold into its native conformation in the in vitro setting.[48] This remarkable observation implies that all of the protein folding information is encoded in the protein sequence. It was concluded that the energy of the system is lowest when a protein is in its native conformation, which has been an established principle for understanding protein folding. Anfinsen dogma makes the protein folding problem become a physical chemical problem.

Levinthal first recognized in 1969 that a random, unbiased search would involve an exponentially large number of local minima.[49-51] This is in stark contrast to the millisecond time scale that a protein typically takes to fold to its native conformation. This finding was called Levinthal Parodox: the folded state of a protein cannot be found by random search in a biologically feasible time scale. Levinthal concluded that there must be some sort of pathway for protein folding. Thus began the search for a theory of protein folding, and for knowledge of the folding pathway(s).

The implication from these theories triggered extensive research on the identification of folding intermediates, real-time folding studies, computation modeling and simulations, and energy landscape analysis. From these pioneering works, several models on protein folding mechanism were conceptualized, including a framework model, [52,53] a hydrophobic collapse model,[54] a diffusion collision adhesion model,[55] and a nucleation-condensation model.[56,57] These various theories were able to explain reasonably well particular pieces of experimental data associated with the folding of individual proteins. But none by themselves appeared to offer a universal description of the underlying principles of the folding process.[58,59] Energy landscape theory was proposed thereafter.

1.2.1 Energy Landscape Theory

Energy landscape is actually a mapping of potential energy defined by the structural coordinates. According to the principles of thermodynamics, if a system has *n* degrees of freedom $\mathbf{F}=(f_1, f_2, f_3 \ldots f_n)$, the stable state of the system can be found by determining the set of values that gives the minimum value of the free energy function $G(\mathbf{F})=G(f_1, f_2, f_3, \ldots. f_n)$ when explored over all possible values of *f*. Such functions are called energy landscapes.[60-62]

Fig. 1.5 shows a funnel shaped energy landscape. The overall folding kinetics are determined by the shape of energy landscape. The global minimum of the landscape corresponds to the native conformation. Local minima give rise to the formation of folding intermediates. We can see that the landscape shows the multiple folding pathways, and each pathway may have different local minimum and energy barrier. This shows the multiplicity and heterogeneity of the landscape. The nature of protein folding energy landscape suggests that any single molecule can take any of a number of routes through the landscape.

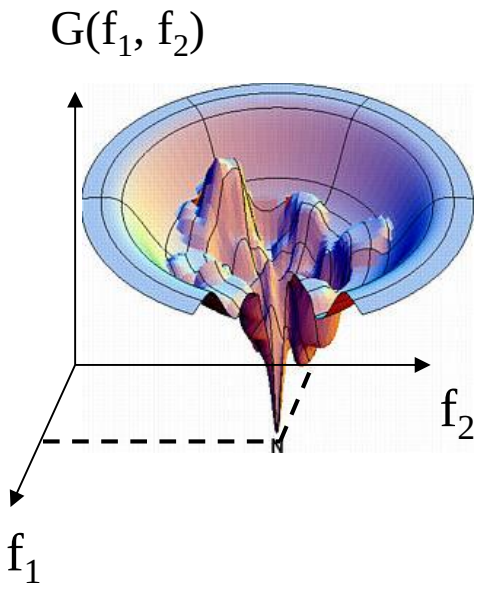

Figure 1.5. Funnel-shaped energy landscape. Reproduced from Borgia et al.[63]

Obviously, protein folding is clearly a very complex process, since this process could involve a large number of structural coordinates, the backbone and sidechain bond angles. The application of energy landscape theory to the protein folding problem provides a step toward depicting the complexity of the protein folding process by showing the interplay between structural coordinates and representing the degree of conformational heterogeneity

associated with various stages of folding.[64] Energy landscape has been developed to be a more general conceptual framework for understanding the mechanism of protein folding, which is believed to determine the thermodynamic stability and the folding process of proteins. Many experimental and theoretical studies are devoted to characterizing the energy landscape of protein folding.[64-68]

1.3 EXPERIMENTAL METHODS USED FOR STUDYING PROTEIN FOLDING

Many techniques have been used to study protein folding problem. In the following, we are going to discuss some of main techniques.

X-Ray diffraction is the gold-standard of structural probes.[69] Its main use is to determine static structures of hydrated solid crystal of peptides and proteins. These static X-ray structures give detailed information on conformation, bond lengths, and interresidue atomic distances. However, high-resolution studies of proteins are not always feasible. For example, crystallographic studies require high-quality single crystals which for many proteins are not available. X-ray diffraction is not able to probe dynamic information of protein.

Multidimensional NMR is also a powerful and routine tool to investigate protein structures.[70] NMR spectra can provide protein structure information with atomic resolution. Protein structure information can be obtained from the chemical shifts, spin-spin coupling constants, residual dipolar coupling, and cross-relaxation signals.[71,72] By the methodology Vuister and Bax proposed[73], $^{3}J_{HN\alpha} = 6.51\cos^2\theta - 1.76\cos\theta + 1.6$ with $\theta = |\Phi - 60°|$, NMR can provide quantitative Φ dihedral angle information of peptide secondary structure by

determining $^{3}J_{HN\alpha}$ coupling constant. The high resolution of NMR makes possible probing the protein structure dynamics.[74] Unfortunately, NMR is only able to probe protein dynamics at relatively long time scales.

Circular Dichroism (CD) spectroscopy measures the differential absorption of left-handed circularly polarized light and right-handed circularly polarized light in the ultraviolet region. Peptide bonds have intense absorption at ~190 nm due to the π-π^* transition. Different secondary structural elements in protein give rise to different characteristic CD spectra, so CD can be used to assess the presence of particular secondary structure. Employing basis datasets, the secondary structure composition of proteins can also be evaluated.[75]

IR spectroscopy has emerged as an important technique for studying protein structure and fast folding kinetics.[76] The frequency of the amide stretching vibration has been shown to be strongly correlated with protein secondary structure. The AmI band is one of valuable reporters of peptide structure and environment which mainly derives from C=O stretching vibration. However, there are two main shortcomings for IR spectroscopy: one arises from the overlap of water absorption; the other one arises from the contribution of side chain absorption in the AmI region. and the spectral subtraction reduces the S/N, and the diminishing the accuracy with which protein structure can be quantitative.[77]

UV Resonance Raman (UVRR) spectroscopy, as a vibrational technique, enjoys advantages similar to infrared in terms of structural specificity, but, unlike infrared, UVRR spectroscopy is not subject to interferences from water.[78,79] The resonance effect allows one to choose, through selection of the excitation frequency, to study specific UV chromophores. Resonance Raman scattering at ~200 nm provides directly information on the protein

secondary structure, since the vibrations coupled to the peptide bond electronic transition is selectively enhanced. ~229 nm excitation enhances the vibrations of aromatic amino acid side chains, such as tyrosine, tryptophan in protein and allows monitoring the aromatic amino acid environment. This selectivity dramatically simplifies the spectra, since there is no interference from the vibrational bands which are not resonantly enhanced. Also, as an optical technique, fast time resolved experiment can be carried out.

Fluorescence is one of the most frequently used techniques for protein dynamic study with high sensitivity and versatility.[80] Chromophore fluorescence intensity is sensitive to both global and local changes in protein conformation. The (un)folding of a protein can be studied by monitoring the fluorescence spectrum or intensity change, provided that the (un)folding processes change the environment of the chromophore used. Aromatic amino acids like Trp are the convenient intrinsic fluorophores because of the high quantum yield and low occurrence in sequence.

Since the strong quantum yield, fluorescence signal of single molecule can be detected. In Fluorescence resonance energy transfer (FRET) experiment, by engineering suitable donor and acceptor chromophores in the protein, it allows measurements of intramolecular distances and distance change during protein folding, which provides a detailed picture of the protein structure dynamics. Furthermore, FRET can be used to determine the distance distribution and thus conformational distribution and dynamics of proteins.[81-83]

Atomic force microscopy and **optical tweezers** are the most recently developed advanced single molecule force spectroscopy used to study protein folding problem.[84-87] In these experiments, the external force is exerted to single protein molecules, and denatures the

protein structure. Proteins are directly manipulated and their behavior under tension is described in terms of a well-defined reaction coordinate, namely their molecular end-to-end distance. These methods can monitor in real time the fluctuations between different molecular conformations and characterize directly the thermodynamics and kinetics of these processes, measure directly the potential of mean force of a molecule as a function of its extension, probe the protein folding intermediates, and explore the protein folding pathway and energy landscape.[85,88-90]

Hydrogen exchange is a widely used method to probe protein solution structures. Protein hydrogen exchange studies were initiated by Linderstrom-Lang and the Carlsberg group in the mid-1950s.[91] The basic idea is that hydrogens on main chain and polar side chain groups of protein could exchange with the hydrogen atoms of the solvent water readily.

The amide hydrogen exchange is both acid- and base-catalyzed. The pH dependence of the exchange rate has been well studied.[92] At a particular condition, such as pH and temperature et al., the amide proton exchange rate can slow down significantly when hydrogen involves hydrogen bonding or the solvent inaccessibility because of the formation of tertiary structure. Therefore, the rate of hydrogen exchange of a protein is related to the stability of secondary structure elements and to the tertiary structure of the protein. As a result, analysis of the kinetics of hydrogen exchange in proteins has been a powerful method for studying both protein structural and dynamic properties. The exchange rate also reflects the nature of the protein environment and yield insight into a major class of backbone fluctuations and intermediate structural information.

The hydrogen exchange method is usually combined with various spectroscopic methods. With increasing field strengths and multidimensional methods, NMR became the

instrument of choice for studying hydrogen isotope exchange in protein since the late 1970s and led to the resurgence of H/D method.[92-94] Following NMR, mass spectrometry (MS), particularly since the inception of ESI-MS at the beginning of the 1990s, has become an increasing popular for monitoring hydrogen isotope exchange to examine difficult biophysical systems.[95-97] Raman and IR spectroscopies combined with hydrogen exchange are widely used method to investigate protein structures.

1.4 REFERENCES

(1) Bucciantini, M.; Giannoni, E.; Chiti, F.; Baroni, F.; Formigli, L.; Zurdo, J.; Taddei, N.; Ramponi, G.; Dobson, C. M.; Stefani, M. *Nature* **2002**, *416*, 507-511.

(2) Dobson, C. M. *Philos. Trans. R. Soc. London, Ser. B* **2001**, *356*, 133-145.

(3) Dobson, C. M. *Nature* **2002**, *418*, 729-730.

(4) Ellis, R. J.; Pinheiro, T. J. T. *Nature* **2002**, *416*, 483-484.

(5) Lansbury, P. T., Jr. *Proc. Natl. Acad. Sci. U. S. A.* **1999**, *96*, 3342-3344.

(6) Walsh, D. M.; Klyubin, I.; Fadeeva, J. V.; Cullen, W. K.; Anwyl, R.; Wolfe, M. S.; Rowan, M. J.; Selkoe, D. J. *Nature* **2002**, *416*, 535-539.

(7) Seife, C. *Science* **2005**, *309*, 78.

(8) Fitzkee, N. C.; Fleming, P. J.; Gong, H.; Panasik Jr, N.; Street, T. O.; Rose, G. D. *Trends Biochem. Sci.* **2005**, *30*, 73-80.

(9) Pauling, L.; Corey, R. B.; Branson, H. R. *Proc. Natl. Acad. Sci. U. S. A.* **1951**, *37*, 205-211.

(10) Perutz, M. F. *Nature* **1951**, *167*, 1053-1054.

(11) Barlow, D., J.; Thornton, J. M. *J. Mol. Biol.* **1988**, *201*, 601-619.

(12) Toniolo, C.; Benedetti, E. *Trends Biochem. Sci.* **1991**, *16*, 350-353.

(13) Enkhbayar, P.; Hikichi, K.; Osaki, M.; Kretsinger, R. H.; Matsushima, N. *Proteins* **2006**, *64*, 691-699.

(14) Millhauser, G. L. *Biochemistry* **1995**, *34*, 3872-3877.

(15) Bolin, K. A.; Millhauser, G. L. *Acc. Chem. Res.* **1999**, *32*, 1027-1033.

(16) Millhauser, G. L.; Stenland, C. J.; Hanson, P.; Bolin, K. A.; van der Ven, F. J. M. *J. Mol. Biol.* **1997**, *267*, 963-974.

(17) Long, H. W.; Tycko, R. *J. Am. Chem. Sco.* **1998**, *120*, 7039-7048.

(18) Sundaralingam, M.; Sekharudu, Y. C. *Science* **1989**, *244*, 1333-1337.

(19) Scheinerman, F. B.; Brooks, C. L. *J. Am. Chem. Sco.* **1995**, *117*, 10098-10103.

(20) Sung, S. S. *Biophys. J.* **1995**, *68*, 826-834.

(21) Fodje, M. N.; Al-Karadaghi, S. *Protein Eng.* **2002**, *15*, 353-358.

(22) Sasaki, S.; Yasumoto, Y.; Uematsu, I. *Macromolecules* **1981**, *14*, 1797-1801.

(23) Musso, G. F.; Patthi, G. S.; Ryskamp, T. C.; Provov, S.; Kaiser, E. T.; Velicelebi, G. *Biochemistry* **1998**, *27*, 8174-8181.

(24) Weaver, T. D. *Protein Sci.* **2000**, *9*, 201-206.

(25) Mahadevan, J.; Lee, K.-H.; Kuczera, K. *J. Phys. Chem. B* **2001**, *105*, 1683-1876.

(26) Sudha, R.; Kohtani, M.; Breaux, G. A.; Jarrold, M. F. *J. Am. Chem. Soc.* **2004**, *126*, 2777-2784.

(27) Armen, R.; Alonso, D. O. V.; Daggett, V. *Protein Sci.* **2003**, *12*, 1145-1157.

(28) Shirley, W. A.; Brooks, C. L. I. *Proteins: Struct. Funct. Genet.* **1997**, *28*, 59-71.

(29) Flory, P. J. *Statistical Mechanics of chain molecules*; Interscience: New York, 1969.

(30) Ghelis, C.; Yon, J. *Academic Press* **1982**.

(31) Tanford, C. *Adv. Prot. Chem.* **1968**, *23*, 121-282.

(32) Ramachandran, G. N.; Sasisekharan, V. *Adv. Prot. Chem.* **1968**, *23*, 283-438.

(33) Pappu, R. V.; Srinivasan, R.; Rose, G. D. *Proc. Natl. Acad. Sci. U. S. A.* **2000**, *97*, 12565.

(34) Fitzkee, N. C.; Rose, G. D. *Protein Sci.* **2004**, *13*, 633-639.

(35) Shi, Z.; Chen, K.; Liu, Z.; Kallenbach, N. R. *Chem. Rev.* **2006**, *106*, 1877-1897.

(36) Shi, Z.; Olson, C. A.; Kallenbach, N. R.; Sosnick, T. R. *J. Am. Chem. Sco.* **2002**, *124*, 13994-13995.

(37) Eker, F.; Griebenow, K.; Cao, X.; Nafie, L. A.; Schweitzer-Stenner, R. *Proc. Natl. Acad. Sci. U. S. A.* **2004**, *101*, 10054-10059.

(38) Eker, F.; Griebenow, K.; Schweitzer-Stenner, R. *J. Am. Chem. Sco.* **2003**, *125*, 8178-8185.

(39) Chellgren, B. W.; Creamer, T. P. *J. Am. Chem. Soc.* **2004**, *126*, 14734-14735.

(40) Mezei, M.; Fleming, P. J.; Srinivasan, R.; Rose, G. D. *Proteins* **2004**, *55*, 502-507.

(41) Pappu, R. V.; Rose, G. D. *Protein Sci.* **2002**, *11*, 2437.

(42) Chellgren, B. W.; Creamer, T. P. *Biochemistry* **2004**, *43*, 5864-5869.

(43) Kaiser, E. T.; Mezei, M.; Gindin, T.; Osman, R. *Proteins* **2004**, *55*, 493-501.

(44) Makowska, J.; Rodziewicz-Motowidlo, S.; Baginska, K.; Vila, J. A.; Liwo, A.; Chmurzynski, L.; Scheraga, H. A. *Proc. Natl. Acad. Sci. U. S. A.* **2006**, *103*, 1744-1749.

(45) Shi, Z.; Olson, C. A.; Rose, G. D.; Baldwin, R. L.; Kallenbach, N. R. *Proc. Nat. Acad. Sci. U. S. A.* **2002**, *99*, 9190-9195.

(46) Woody, R. W. *Adv. Biophys. Chem* **1992**, *2*, 37-79.

(47) Hovmoller, S.; Zhou, T.; Ohilson, T. *Acta Crystallogr., D: Biol. Crystallogr.* **2002**, *58*, 768.

(48) Anfinsen, C. B. *Science* **1973**, *181*, 223-230.

(49) Levinthal, C. *J. Chim. Phys.* **1968**, *65*, 44-45.

(50) Levinthal, C. *In Mossbauer Spectroscopy in Biological systerms* **1969**, 22-24.

(51) Karplus, M. *Fold. Des.* **1997**, *2*, 569-576.

(52) Ptitayn, O. B.; Rashin, A. A. *Biophys. Chem* **1975**, *3*, 1-20.

(53) Kim, P. S.; Baldwin, R. L. *Ammu. Rev. Biochem.* **1990**, *59*.

(54) Dill, K. A. *Biochemistry* **1985**, *24*, 1501-9.

(55) Karplus, M.; Weaver, D. L. *Protein Sci.* **1994**, *3*, 650-668.

(56) Fersht, A. R. *Proc. Natl. Acad. Sci. U. S. A.* **2000**, *97*, 1525-1529.

(57) Osterhout, J., J. *Protein Pept. Lett.* **2005**, *12*, 159-164.

(58) Schymkowitz, W. H.; Rousseau, F.; Serrano, L. *Proc. Natl. Acad. Sci. U. S. A.* **2002**, *99*, 15846-15848.

(59) Daggett, V.; Fersht, A. R. *Trends Biochem. Sci.* **2003**, *28*, 18-25.

(60) Onuchic, J. N.; Nymeyer, H.; Garcis, A. E.; Chahine, J.; Socci, N. D. *Adv. Prot. Chem* **2002**, *53*, 87.

(61) Wales, D. J. *Energy landscape -- With application to clusters, biomolecules and glasses*; Cambridge University: Cambridge, 2003.

(62) Dinner, A. R.; Sali, A.; Smith, L., J.; Dobson, C. M.; Karplus, M. *Trends Biochem. Sci.* **2000**, *25*, 331-339.

(63) Borgia, A.; Williams, P. M.; Clarke, J. In *Annu. Rev. biochem.*, 2008; Vol. 77; pp 101-125.

(64) Dill, K. A.; Chan, H. S. *Nature Struct. Biol.* **1997**, *4*, 10-19.

(65) Dill, K. A.; Ozkan, S. B.; Shell, M. S.; Weikl, T. R. *Annu. Rev. Biophys.* **2008**, *37*, 289-316.

(66) Gruebele, M. *Curr. Opin. Struct. Biol.* **2002**, *12*, 161-168.

(67) Lyubovitsky, J. G.; Gray, H. B.; Winkler, J. R. *J. Am. Chem. Soc.* **2002**, *124*, 5481.

(68) Mello, C. C.; Barrick, D. *Proc. Natl. Acad. Sci. U. S. A.* **2004**, *39*, 14102-14107.

(69) Dickerson, R. E. *Annu. Rev. Biochem.* **1972**, *41*, 815-842.

(70) Bax, A.; Grzesiek, S. *Accounts Chem. Res.* **1993**, *26*, 131-8.

(71) Kumar, T. K. S.; Yu, C. *Acc. Chem. Res.* **2004**, *37*, 929-936.

(72) Dyson, H. J.; Wright, P. E. *Annu. Rev. Phys.l Chem.* **1996**, *47*, 369-395.

(73) Vuister, G. W.; Bax, A. *J. Am. Chem. Sco.* **1993**, *115*, 7772-7777.

(74) Felitsky, D. J.; Lietzow, M. A.; Dyson, H. J.; Wright, P. E. *Proc. Natl. Acad. Sci. U. S. A.* **2008**, *105*, 6278-6283.

(75) Kelly, S. M.; Jess, T. J.; Price, N. C. *Biochim. Biophys. Acta* **2005**, *1751*, 119-139.

(76) Williams, S.; Causgrove, T. P.; Gilmanshin, R.; Fang, K. S.; Callender, R. H.; Woodruff, W. H.; Dyer, R. B. *Biochemistry* **1996**, *35*, 691-7.

(77) Surewicz, W. K.; Mantsch, H. H.; Chapman, D. *Biochemistry* **1993**, *32*, 389-394.

(78) Asher, S. A. *Anal. Chem.* **1993**, *65*, 201A-210A.

(79) Asher, S. A. *Handbook of Vibrational Spectroscopy, John Whiley & Sons, Ltd.* **2001**, *1*, 557-571.

(80) Royer, C. A. *Chem. Rev.* **2006**, *106*, 1769-1784.

(81) Brockwell, D. J.; Smith, D. A.; Radford, S. E. *Curr. Opin. Struct. Biol.* **2000**, *10*, 16-25.

(82) Rhoades, E.; Gussakovsky, E.; Haran, G. *Proc. Nat. Acad. Sci. U. S. A.* **2003**, *100*, 3197-3202.

(83) Schuler, B. *ChemPhysChem* **2005**, *6*, 1206-1220.

(84) Borgia, A.; Williams, P. M.; Clarke, J. *Annu. Rev. Biochem.* **2008**, *77*, 101-125.

(85) Cecconi, C.; Shank, E. A.; Bustamante, C.; Marqusee, S. *Science* **2005**, *309*, 2057-2060.

(86) Liphardt, J.; Onoa, B.; Smith, S. B.; Tinoco, I., Jr.; Bustamante, C. *Science* **2001**, *292*, 733-737.

(87) Forman, J. R.; Clarke, J. *Curr. Opin. Struct. Biol.* **2007**, *17*, 58-66.

(88) Neuman, K. C.; Nagy, A. *Nature Methods* **2008**, *5*, 491-505.

(89) Fernandez, J. M.; Li, H. *Science* **2004**, *303*, 1674-1678.

(90) Shank, E. A.; Cecconi, C.; Dill, J. W.; Marqusee, S.; Bustamante, C. *Nature* **2010**, *465*, 637-640.

(91) Berger, A. K. L.-L. *Arch. Biochem. Biophys.* **1957**, *69*, 106-118.

(92) Dempsey, C. E. *Prog. Nucl. Magn. Reson. Spectrosc.* **2001**, *39*, 135-170.

(93) Englander, S. W. *Annu. Rev. Biophys. Biomol. Struct.* **2000**, *29*, 213-238.

(94) Krishna, M. M. G.; Hoang, L. L., Y.; ; Englander, S. W. *Methods* **2004**, *34*, 51-64.

(95) Miranker, A.; Robinson, C. V.; Radford, S. E.; Aplin, R. T.; Dobson, C. M. *Science* **1993**, *262*, 896-900.

(96) Hoofnagle, A. N.; Resing, K. A.; Ahn, N. G. *Annu. Rev. Biophys. Biomol. Struct.* **2003**, *32*, 1-25.

(97) Kheterpal, I.; Cook, K. D.; Wetzel, R. *Method Enzymol* **2006**, *413*, 140-166.

2.0 UV RESONANCE RAMAN SPECTROSCOPY

2.1 INTRODUCTION TO RAMAN SPECTROSCOPY

Raman scattering effect arises from the interaction of the incident light with the electrons in the illuminated molecule, which leads to the energy transfer between the photon and molecule. As a result, the light is scattered in frequency shifted by the energy of its characteristic molecular vibrations. The analysis of scattered light provides the rich information about molecular structure of sample.

Raman effect was first discovered by Raman and Krishnana by studying the light scattering of water and alcohol vapors in 1927.[1,2] Since then, the effect has attracted attention from a basic research point of view as well as a powerful spectroscopic technique with many practical applications. There are two major milestones in the history of Raman spectroscopy which results in dramatic development of Raman techniques. The first is the advent of the laser in the 1960s, which provides an intense monochromatic light source. The second one is the technique advances in detector and tunable lasers in the 1980s.

Beside normal Raman, various special Raman spectroscopy techniques have been developed, including Resonance Raman (RR), surface enhanced Raman (SERS), tip enhanced Raman (TERS), nonlinear Raman such as Coherent anti-stokes Raman (CARS), stimulated Raman (SRS), and hyper-Raman spectroscopy.

In normal Raman, the energy of the incident light is not sufficient to excite the molecule to a higher electronic energy state, but a "virtual state", which falls between the ground and an electronically excited state. The spectral intensity in normal Raman is very weak. When incident light energy is high enough to excite the molecule to the excited electronic state, the vibrational modes which coupled with the electronic transition would be selectively enhanced. The effect is called RR scattering. In RR, the Raman signal can be enhanced in ~10^6 order. Therefore, RR spectroscopy can be used to probe different chromophores in the molecule by changing the excitation wavelength.

Surface enhanced Raman arises from the enhanced local field in the close proximity of nanostructured metal surfaces, typically silver or gold, when the incident and scattered radiation is resonant with the local plasmonic resonance of the metal surface.[3] This technique is one of the fast growing areas of Raman spectroscopy. TERS is a new developed area of SERS, which introduces the use of a metallic tip brought into close proximity of surface-bound molecule.[4] CARS and SRS, in recent years, have been gaining importance as a practical nonlinear method of spectroscopic investigation. Because of their high spatial and time resolution, and using vibrational contrast instead of labeling, CARS and SRS microscopy techniques have been developed and is becoming more and more popular for investigating biological problems.[5-10]

Raman spectroscopy is currently experiencing tremendous growth and has been applied in studying various problems. Non-laboratory application triggers the rapid development of handful Raman instrumentation. Recent advances in Raman spectroscopy have been reviewed recently in Journal of Raman spectroscopy.[4,11-13]

2.2 LIGHT SCATTERING THEORY[14]

If a molecule interacts with light, the electric field of photons will exert oppositely directed forces on the electrons and the nuclei. As a result, the electrons will be displaced relative to the nuclei, and the polarized molecules will have an induced dipole moment caused by the external field, which can be expressed by equation:

$$P = \alpha E \quad (2.1)$$

where P is the induced dipole moment, α is the polarizability of the molecule, a measure of the ability to respond to an electric field and acquire an electric dipole moment. E is the electric field of the incident light:

$$E = E_0 \cos 2\pi \nu_0 t \quad (2.2)$$

In classical theory, the polarizability α is a function of nuclear coordinates Q_j whose variation with vibration of the molecule can be expressed as follows:

$$\alpha = \alpha_0 + (\frac{\delta\alpha}{\delta Q_j})Q_j + ... \quad (2.3)$$

The time dependence of Q_j is given by

$$Q_j = Q_j^0 \cos 2\pi \nu_j t \quad (2.4)$$

If we just consider first order term, we can get:

$$P = \alpha_0 E_0 \cos 2\pi \nu_0 t + E_0 Q_j{}^0 (\frac{\delta\alpha}{\delta Q_j}) \frac{\cos 2\pi(\nu_0 + \nu_j)t + \cos 2\pi(\nu_0 - \nu_j)t}{2} \quad (2.5)$$

The above induced dipole moment derived from classical treatment of interaction of the molecule and the incident radiation field gives the following useful information: (1) It demonstrates the light is scattered at three frequencies: Rayleigh scattering; Stokes Raman scattering, and anti-Stokes Raman scattering; (2) It provides the primary selection rule for

Raman scattering is the change of polarizability ($\frac{\delta\alpha}{\delta Q_j} \neq 0$); (3) $\frac{\delta\alpha}{\delta Q_j}$ may vary for different molecules and for different vibration modes in a given molecules, which leads to a wide variation in Raman scattering intensity; (4) $\frac{\delta\alpha}{\delta Q_j}$ is generally much smaller than α_0, so Raman scattering is much weaker than Rayleigh scattering. However, classical theory cannot provide reasonable explanation of resonance Raman scattering.

The Raman resonance enhancement can be explained by quantum mechanical theory.[14] The quantum theory of spectroscopic processes treats the external electronic field as a perturbation, and explores how energy may be transferred between the radiation and molecules as a result of their interaction. According to quantum theory, radiation is emitted or absorbed as a result of a system making a transition between two discrete energy levels. The induced transition dipole moment associated with the initial and final molecular states is defined by $P_{fi} = \left\langle \psi_f^{'} \middle| \hat{P} \middle| \psi_i^{'} \right\rangle$. Where $\hat{P}$ is the dipole moment operator, and $\psi_f^{'}$ and $\psi_i^{'}$ is the perturbed the time-dependent wavefunctions for the final and initial states.

The general expression of transition polarizability $(\alpha)_{fi}$ with components $\rho\sigma$ is:

$$(\alpha_{\rho\sigma})_{fi} = \frac{2\pi}{h} \sum_{r \neq i,f} \left\{ \frac{\left\langle f \middle| \hat{P}_\rho \middle| r \right\rangle \left\langle r \middle| \hat{P}_\sigma \middle| i \right\rangle}{\omega_{ri} - \omega_1 - i\Gamma_r} + \frac{\left\langle f \middle| \hat{P}_\sigma \middle| r \right\rangle \left\langle r \middle| \hat{P}_\rho \middle| i \right\rangle}{\omega_{ri} + \omega_1 + i\Gamma_r} \right\} \quad (2.6).$$

f, *r*, *i* refer to the wavefunction of final, initial and virtual states, as shown in Fig. 2.1. ω is the frequency at a specific state shown at subscript. ω_1 is the frequency of incident radiation. Γ comes from the *r* state wavefunction: $\Psi_r = \psi_r \exp - i(\omega_r - i\Gamma_r)t$, which relates to the lifetime of the *r* state. $\omega_{ri} = \omega_r - \omega_i$. The above equation shows the relationship between the polarizability to the energy levels and wavefunctions of the scattering system. Let us

consider the frequency denominators: when $\omega_1 \approx \omega_{ri}$, the first denominator tends to $-i\Gamma_r$, the second denominator cannot become small, and the first term will dominate in the sum over *r*, and the resonance Raman scattering occurs. The intensity of resonance Raman scattering can be expected to 10^6 orders of magnitude greater than normal Raman scattering because of the first denominator becomes very small.

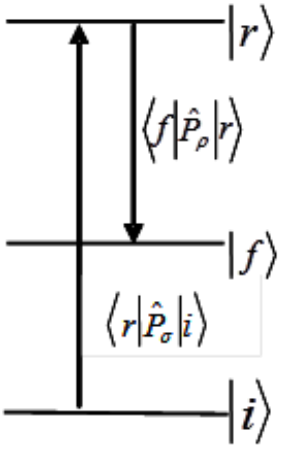

Figure 2.1. Energy transition diagram.

From the induced dipole moment, the intensity of scattering can be determined according to the equation:

$$I_{fi} = C(\omega_1 + \omega_{fi})^4 P_{fi}^{\ 2} \qquad (2.7)$$

C is a constant equal to $64\pi^2/(3c^2)$, where *c* is the velocity of light.

So the following points are addressed: which types of electronic transition give rise to significant Raman intensity enhancement? Which bands are enhanced in a resonance Raman spectrum? In order to answer these questions, simplification of polarizability expression is needed. In resonance Raman scattering, the terms with non-resonant denominators is relative small so that it can be neglected. It is convenient to apply Born-Oppenheimer approximation to separate the vibronic states into products of vibrational and electronic states. The

electronic transition moments which depend on the molecular vibrational coordinates Q_k, can be expressed in term of the Herzberg-Teller expansion using perturbation theory. Finally, the $\rho\sigma$ component of the polarizability tensor associated with the vibrational transition from $e^g v^f$ to $e^g v^i$ is given by:

$$(\alpha_{\rho\sigma})_{e^g v^f : e^g v^i} = A + B + C + D \qquad (2.8)$$

where $$A = \frac{1}{\hbar}(p_\rho)^0_{e^g e^r}(p_\sigma)^0_{e^r e^g} \sum_{v_k^r} \frac{\left\langle v_k^{f(g)} \middle| v_k^{r(r)} \right\rangle \left\langle v_k^{r(r)} \middle| v_k^{i(g)} \right\rangle}{\omega_{e^r v_k^r : e^g v_k^i} - \omega_1 - i\Gamma_{e^r v_k^r}} \qquad (2.9)$$

$$B = \frac{1}{\hbar^2}(p_\rho)^0_{e^g e^s} \frac{h^k_{e^s e^r}}{\omega_{e^r} - \omega_{e^s}} (p_\rho)^0_{e^r e^g} \sum_{v_k^r} \frac{\left\langle v_k^{f(g)} \middle| Q_k \middle| v_k^{r(r)} \right\rangle \left\langle v_k^{r(r)} \middle| v_k^{i(g)} \right\rangle}{\omega_{e^r v_k^r : e^g v_k^i} - \omega_1 - i\Gamma_{e^r v_k^r}} +$$
$$\frac{1}{\hbar^2}(p_\rho)^0_{e^g e^r} \frac{h^k_{e^r e^s}}{\omega_{e^r} - \omega_{e^s}} (p_\sigma)^0_{e^s e^g} \sum_{v_k^r} \frac{\left\langle v_k^{f(g)} \middle| v_k^{r(r)} \right\rangle \left\langle v_k^{r(r)} \middle| Q_k \middle| v_k^{i(g)} \right\rangle}{\omega_{e^r v_k^r : e^g v_k^i} - \omega_1 - i\Gamma_{e^r v_k^r}} \qquad (2.10)$$

$$C = \frac{1}{\hbar^2}(p_\rho)^0_{e^t e^r} \frac{h^k_{e^g e^t}}{\omega_{e^g} - \omega_{e^t}} (p_\rho)^0_{e^r e^g} \sum_{v_k^r} \frac{\left\langle v_k^{f(g)} \middle| Q_k \middle| v_k^{r(r)} \right\rangle \left\langle v_k^{r(r)} \middle| v_k^{i(g)} \right\rangle}{\omega_{e^r v_k^r : e^g v_k^i} - \omega_1 - i\Gamma_{e^r v_k^r}} +$$
$$\frac{1}{\hbar^2}(p_\rho)^0_{e^g e^r} \frac{h^k_{e^t e^g}}{\omega_{e^g} - \omega_{e^t}} (p_\sigma)^0_{e^s e^g} \sum_{v_k^r} \frac{\left\langle v_k^{f(g)} \middle| v_k^{r(r)} \right\rangle \left\langle v_k^{r(r)} \middle| Q_k \middle| v_k^{i(g)} \right\rangle}{\omega_{e^r v_k^r : e^g v_k^i} - \omega_1 - i\Gamma_{e^r v_k^r}} \qquad (2.11)$$

$$D = \frac{1}{\hbar^2}(p_\rho)^0_{e^g e^s} \frac{h^k_{e^s e^r} h^k_{e^r e^{s'}}}{(\omega_{e^r} - \omega_{e^s})(\omega_{e^r} - \omega_{e^{s'}})} (p_\sigma)^0_{e^{s'} e^g} \sum_{v_k^r, v_{k'}^r} \frac{\left\langle v_k^{f(g)} \middle| Q_k \middle| v_k^{r(r)} \right\rangle \left\langle v_{k'}^{r(r)} \middle| Q_{k'} \middle| v_{k'}^{i(g)} \right\rangle}{\omega_{e^r v_k^r : e^g v_k^i} - \omega_1 - i\Gamma_{e^r v_k^r}}$$

(2.12)

where e^g and e^r are the electronic quantum number at ground and r (virtual) states, respectively. $v_k^{f(g)}$ is the vibrational quantum number at the ground final state for kth vibrational mode. $h^k_{e^s e^e}$ is a coupling integral defined by $h^k_{e^s e^e} = \left\langle \psi_{e^s}(Q_0) \middle| (\partial \hat{\mathrm{H}} / \partial Q_k)_0 \middle| \psi_{e^r}(Q_0) \right\rangle$. $(p_\rho)^0_{e^g e^r}$ is the pure electronic transition dipole moment

associated with the electronic transition $\left|e^g\right\rangle \leftarrow \left|e^r\right\rangle$, and the superscript 0 indicates the transition involves the unperturbed states.

The above equations show the transition polarizability arises from four factors: the pure electronic transition moment and vibrational overlap integrals named A-term (Eq 2.9), vibronic coupling of the resonant electronic state to one or more other excited states named B-term (Eq 2.10); vibronic coupling of the ground electronic state to one or more excited states named C-term (Eq. 2.11), vibronic coupling of the resonant excited state to one or more other excited states named D-term (Eq. 2.12). Here we just discuss the properties of A-term which is the most common case in strongly allowed transitions to show the vibrational enhancement mechanisms.

To attain A-term to be non-zero, two conditions must be fulfilled: (1) the transition dipole moments $(p_\rho)^0_{e^g e^r}$ and $(p_\rho)^0_{e^r e^g}$ are both non-zero, which is fulfilled if the resonant electronic transition is electric-dipole allowed; (2) the products of the vibrational overlap integrals (Franck-Condon factor), $\left\langle \nu_k^{f(g)} \middle| \nu_k^{r(r)} \right\rangle \left\langle \nu_k^{r(r)} \middle| \nu_k^{i(g)} \right\rangle$ are non-zero for at least some values of the excited state vibrational quantum number *v*. The vibrational overlap integrals are zero unless the wavefunctions are non-orthogonal. Non-orthogonality can arise in two ways. One is that there is a difference of vibrational frequency between the ground and excited states $\omega_k^r \neq \omega_k^g$, or the potential energy surface is different in the two electronic states. The second way is that there is a displacement ΔQ_k of the potential energy minimum along the normal coordinate Q_k between the electronic states $\left|e^g\right\rangle$ and $\left|e^r\right\rangle$ and the non-zero overlap integrals can be calculated using the Manneback recursion formulae.[15] Fig 2.2 shows two cases which generate different A-term values. In the first case (the top diagram), the

wavefunction would be orthogonal and there would be no A-term contribution. In the second case (the bottom diagram), a displacement of the potential energy minimum occurs, which lead to significant A-term contribution.

Thus far, if the geometric distortions occur on electronic excitation, which leads to a displacement of the excited state potential surface along the Raman active normal coordinate, the intensity of the vibrational mode will be enhanced greatly (Eq. 2.4). A-term is dominant for the totally symmetric vibrations, while B-term enhancement will dominate only for the non-symmetric vibrations. The C and D-terms give rise to overtones and combination tones, and are normally to be very small.

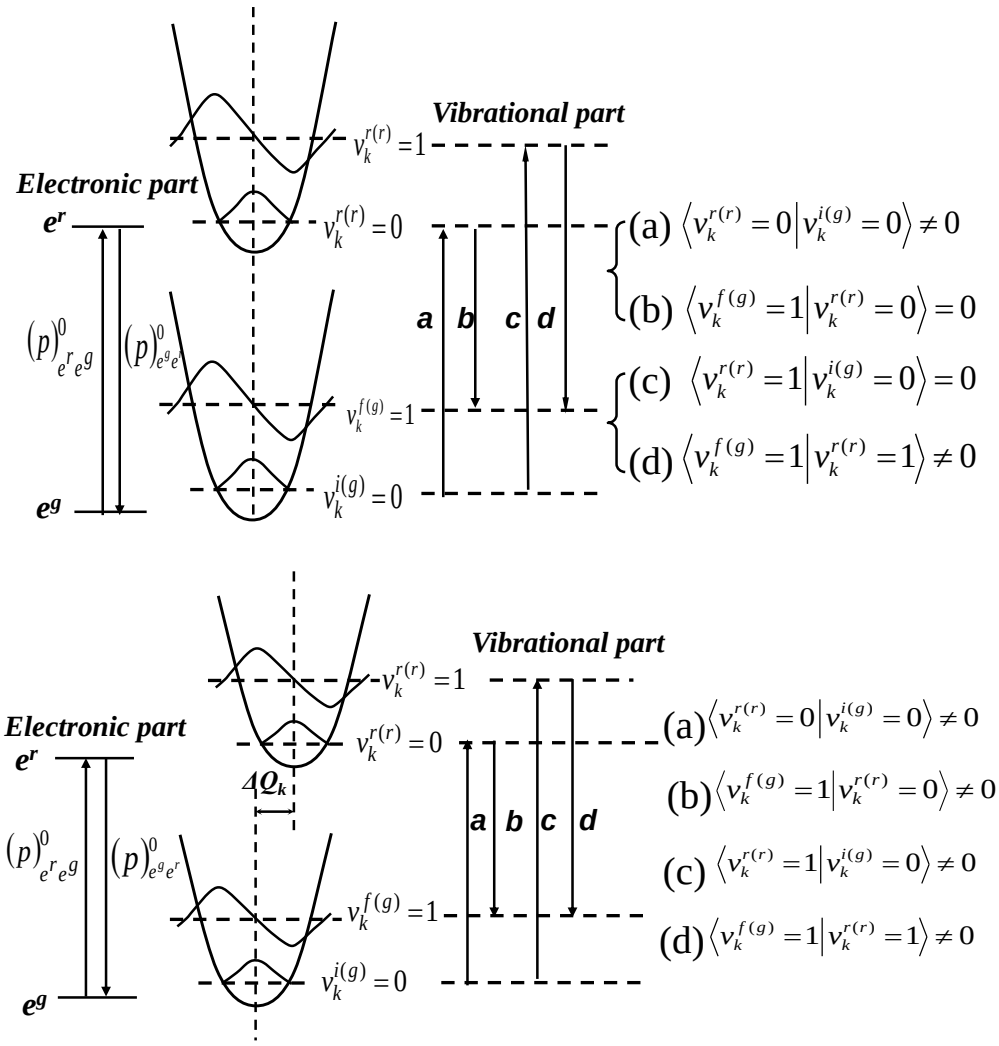

Figure 2.2. The dipole electronic transition and vibrational overlap integrals involved in A-term. The wavefunction would be orthogonal in the top case and there would be no A-term contribution in the top case. Potential energy minimum displacement occurs in the bottom case which leads to significant A-term contribution.

2.3 UV RESONANCE RAMAN CHARACTERISTIC SPECTRA OF PEPTIDE BACKBONE

UV Resonance Raman (UVRR) spectroscopy is known as a very powerful tool for studying protein secondary structure.[16-18] When UV excitation ~200 nm is used to illuminate the peptide/protein, vibrations which are coupled with peptide backbone π-π* electronic transition are selectively enhanced. Extensive research has been done on developing methodology to extract the protein structure information from UVRR spectrum in Sanford Asher's group at the University of Pittsburgh over the past ~10 years, and there have been great advances.[16,19-21]

Fig. 2.3 shows the 204 nm UVRR spectra of aqueous PLL solutions at different pH values where the extended PLL was converted to helical PLL as pH increases. The UV resonance Raman spectra shows characteristic bands which mainly include AmI, AmII, AmIII, and C_α-H bending bands. It can be seen that these band shapes, band intensities and band positions are very sensitive to protein conformation transitions.

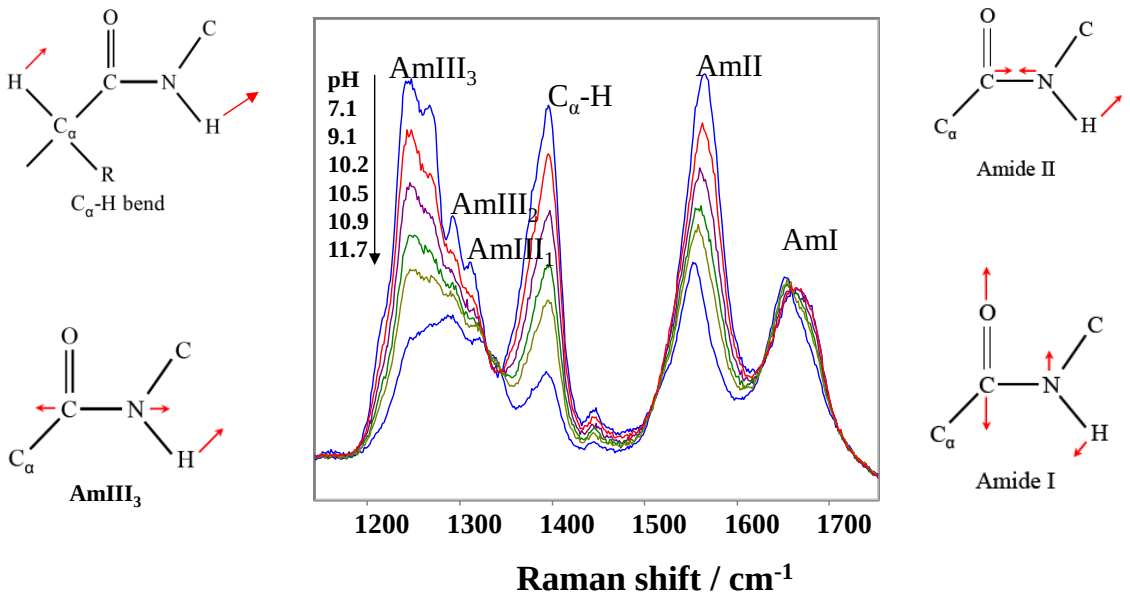

Figure 2.3. 204 nm UVRR spectra of poly-L-lysine at various pH values.

AmI band (~1660 cm^{-1}) is mainly contributed from the peptide carbonyl stretching vibration, although there is a small contribution form the N-H in plane bending vibrations. The wavenumber is lower (~1651 cm^{-1}) for α-helix than for β-turn (1652 cm^{-1}), PPII (1664 cm^{-1}), or β-sheet (1670 cm^{-1}), reflecting the influence of intrahelical H bonds.

AmII band (~1560 cm^{-1}) derives from the C-N stretching and N-H in-plane bending band. This band is very weak in classical Raman but very strong in far UV spectrum. The enhancement with UV excitation can be understood in terms of the geometry changes associated with excitation of the peptide chromophore to its π-π* state. Deuteration will lead the AmII band to lose N-H in-plane bending component and leave an almost pure C–N s AmII' vibration at 1470 cm^{-1}. Previously, it was believed that the AmII band frequency is much less sensitive to structure. However, Huang et al[22] found AmII components at 1522 cm^{-1} for α-helix and 1543 cm^{-1} for β-sheet. Krimm and Bandekar[23] computation result shows the AmII band frequency dependence on peptide conformations . Also, Asher[24] group found

that the UV Raman AmII band of the extended PPII conformation has the largest temperature dependence with ~-0.14 cm^{-1}/°C indicating the AmII band position is sensitive to H-bonding state of the amide bonds.

C_α-H bending band (~1400 cm^{-1}) is of great interest because it is conformational sensitive. The C_α–H b bands that are resonantly enhanced in the extended PPII, β-sheet, and β-strand-like conformations, are not enhanced in the α-helix-like conformations. As a result, as shown in Fig. 2.3, the C_α–H b band shows a large intensity decrease relative to that of the AmII and AmIII bands. Resonance enhancement of C_α-H b band in non-α-helical conformations was suggested to arise from a conformational dependent mixing of the C_α-H bending coordinate with the amide III coordinate, which is absent in α-helices.[19] Using the C_α–H b band intensity to indicate the extended PLL concentration content, the conformational fraction can be calculated.[16,19,25]

AmIII band is the most complicated band but very informative.[26,27] Until now, there is an incomplete understanding of the amide vibrational modes, despite years of excellent experimental and theoretical studies. Diem et al.[28] used IR VCD isotopic substitution and identified that the AmIII bands originate from coupling of N-H in-plane, (N)C_α-H and (C)C_α-H bending vibrations. Lee and Krimm's[29] theoretical and experimental studies of α-helical poly(alanine) also revealed that the AmIII normal-modes of observed AmIII region bands derive from C-N stretch , N-H in-plane bending, C_α-H b, and C_α-C s modes. Sieler *et al*[30] identified two amide III in the UV resonance Raman spectra of glycylglycine.

It is has been shown that the frequency of the amide III band is sensitive to the peptide backbone conformational changes. In 1977, Lord[31] published his classical paper about 'strategy and Tactics in the Raman Spectroscopy of Biomolecules', in which he

postulated that the frequency of the amide III band in the Raman spectra of peptides and proteins is a well-defined function of the dihedral angle Ψ. In a most recent study, Asher et al.[19] investigated in more detail the conformational sensitivity of amide III for alanylalanine, its isotopic derivatives and some acetylated amino acids and found that the NH in-plane bending mode of the peptide group and the respective (C)C_α-H bending mode are coupled. The eigenvector of amide III exhibits an in-phase combination of (C)C_α-H and NH in plane bending, in agreement with earlier suggestions by Jordan and Spiro.[32] Results of normal mode calculations for minimized structures with different constrained Ψ angles suggest that the coupling between the two bending modes exhibits a sinusoidal dependence on Ψ and a linear dependence on the distance between the hydrogen atoms of (C)C-H and N-H: $\nu \approx \nu_0 + A\sin(\Psi - \delta)$, where ν is the calculated AmIII frequency, ν_0 is the AmIII frequency constant, *A* is the amplitude of the frequency dependence on Ψ, and δ is the relative phase of the sine curve with respect to Ψ.[19]

The above vibrational mixing is maximal for Ψ~ 120°, which corresponds to the β-sheet region of the Ramachandran plot and minimal for right-handed α-helical conformations where Ψ~ 60°. This explains the much higher amide III frequency in the UV-Raman spectrum of the helical structures. They also carefully examined and reassigned the bands in the amide III region. They found $AmIII_3$ band is the most sensitive to the peptide bond conformation.

Most recently, by using and ala-based AP peptide, ignoring very modest Φ Ramachandran angle dependence, after examining the hydrogen bonding state of the peptide bonds and temperature dependence in detail, Mikhonin et al.[33] developed a quantitative methodology which calculates the Ψ angle distribution from the $AmIII_3$ band frequency

distributions (Fig. 2.4). The importance of this result is that, Raman spectroscopy can be used to determine the distribution of Ψ angles among the peptides linkages of a protein.

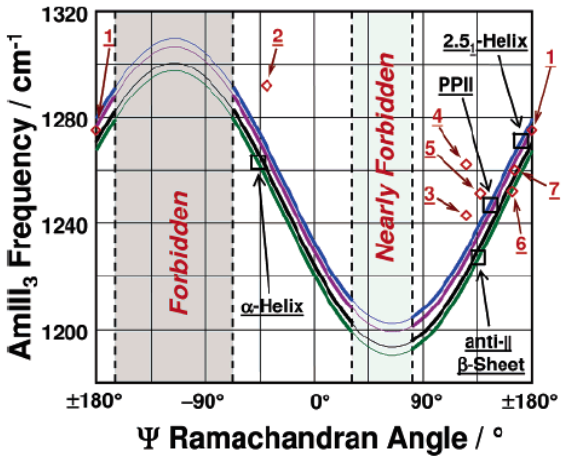

Figure 2.4. Correlation between $AmIII_3$ frequency and Ψ Ramachandran angle. Reproduced form Mikhonin *et al.*[33]

As the discussion above, the vibrational spectrum of proteins contains a wealth of information that can be exploited to learn about the structure and function of proteins. UVRR spectra of proteins have provided a reliable method for secondary structure analysis of proteins and peptides.

2.4 REFERENCES

(1) Raman, C. V.; Krishnan, K. S. *Nature* **1928**, *121*, 501-2.

(2) Raman, C. V. *Indian J. Phys.* **1928**, *2*, 387-98.

(3) Kneipp, K.; Kneipp, H.; Itzkan, I.; Dasari, R. R.; Feld, M. S. *Chem. Rev.* **1999**, *99*, 2957-2975.

(4) Nafie, L. A. *J. Raman Spectrosc.* **2010**, *41*, 1276-1296.

(5) Burkacky, O.; Zumbusch, A.; John Wiley & Sons, Inc., 2008; pp 209-220.

(6) El-Diasty, F. *Vib. Spectrosc.* **2011**, *55*, 1-37.

(7) Evans, C. L.; Xie, X. S. *Annu. Rev. Anal. Chem.* **2008**, *1*, 883-909.

(8) Kano, H.; Huang, Y.-S.; Naito, Y.; Shimada, R.; Hamaguchi, H.-o.; John Wiley & Sons, Inc., 2010; pp 301-312.

(9) Pezacki, J. P.; Blake, J. A.; Danielson, D. C.; Kennedy, D. C.; Lyn, R. K.; Singaravelu, R. *Nat. Chem. Biol.* **2011**, *7*, 137-145.

(10) Min, W.; Freudiger, C. W.; Lu, S.; Xie, X. S. *Annu. Rev. Phys. Chem.* **2011**, *62*, 507-530.

(11) Kiefer, W. *J. Raman Spectrosc.* **2007**, *38*, 1538-1553.

(12) Kiefer, W. *J. Raman Spectrosc.* **2008**, *39*, 1710-1725.

(13) Kiefer, W. *J. Raman Spectrosc.* **2009**, *40*, 1766-1779.

(14) Long, D. A. *The Raman Effect: A Unified Treatment of the Theory of Raman Scattering by Molecules*; John Wiley & Sons: New York, 2002.

(15) Manneback, C. *Physica* **1951**, *17*, 1001.

(16) Chi, Z.; Chen, X. G.; Holtz, J. S. W.; Asher, S. A. *Biochemistry* **1998**, *37*, 2854-2864.

(17) Bykov, S. V.; Lednev, I. K.; Ianoul, A.; Mikhonin, A. V.; Asher, S. A. *Appl. Spectrosc.* **2005**, *59*, 1541-1552.

(18) Asher, S. A. *Anal. Chem.* **1993**, *65*, 201A-210A.

(19) Asher, S. A.; Ianoul, A.; Mix, G.; Boyden, M. N.; Karnoup, A.; Diem, M.; Schweitzer-Stenner, R. *J. Am. Chem. Soc.* **2001**, *123*, 11775-11781.

(20) Lednev, I. K.; Karnoup, A. S.; Sparrow, M. C.; Asher, S. A. *J. Am. Chem. Soc.* **1999**, *121*, 4076-4077.

(21) Mikhonin, A. V.; Ahmed, Z.; Ianoul, A.; Asher., S. A. *J. Phys. Chem. B* **2004**, *108*, 19020-19028.

(22) Huang, C.-Y.; Balakrishinan, G.; Spiro, T. G. *J. Raman Spec.* **2006**, *37*, 277-282.

(23) Krimm, S.; Bandekar, J. *J. Adv. Protein Chem.* **1986**, *38*, 181.

(24) Asher, S. A.; Mikhonin, A. V.; Bykov, S. B. *J. Am. Chem. Soc.* **2004**, *126*, 8433-8440.

(25) Wang, Y.; Purrello, R.; Jordan, T.; Spiro, T. C. *J. Am. Chem. Soc.* **1991**, *113*, 6359-6368.

(26) Schweitzer-Stenner, R.; Eker, F.; Huang, Q.; Griebenow, K.; Mroz, P. A.; Kozlowski, M. *J. Phys. Chem. B* **2002**, *106*, 4292-4304.

(27) Oboodi, M. R.; Alva, C.; Diem, M. *J. Phys. Chem.* **1984**, *88*, 501-505.

(28) Diem, M.; Lee, O.; Roberts, G. M. *J. Phys. Chem.* **1992**, *96*, 548-554.

(29) Lee, S.-H.; Krimm, S. *Biopolymers* **1998**, *46*, 283.

(30) Sieler, G.; Schweitzer-Stenner, R.; Holtz, J. S. W.; Pajcini, V.; Asher, S. A. *J. Phys. Chem. B* **1999**, *103*, 372-384.

(31) Lord, A. C. *Appl. Spectrosc.* **1977**, *31*, 187.

(32) Jordan, T.; Spiro, T. G. *Raman Spectrosc.* **1994**, *25*, 537.

(33) Mikhonin, A. V.; Bykov, S. V.; Myshakina, N. S.; Asher, S. A. *J. Phys. Chem. B* **2006**, *110*, 1928-1934.

CHAPTER 3

UV Resonance Raman Measurements of Poly-L-Lysine's Conformational Energy Landscape: Dependence of perchlorate Concentration and Temperature

This Chapter was published in *Journal of Physical Chemistry B.* 2007, *111*, 7675-7678.The co-authors are Lu Ma, Zeeshan Ahmed, Aleksandr Mikhonin, Sanford Asher.

3.0 UV RESONANCE RAMAN MEASUREMENTS OF POLY-L-LYSINE'S CONFORMATIONAL ENERGY LANDSCAPE: DEPENDENCE OF PERCHLORATE CONCENTRATION AND TEMPERATURE

UV resonance Raman spectroscopy has been used to determine the conformational energy landscape of poly-L-lysine (PLL) in the presence of $NaClO_4$ as a function of temperature. At 1 °C, in the presence of 0.83 M $NaClO_4$, PLL shows an ~86% α-helix-like content, which contains α-helix and π-bulge/helix conformations. The high α-helix-like content of PLL occurs because of charge screening due to strong ion-pair formation between ClO_4^- and the lysine side chain $-NH_3^+$. As the temperature increases from 1 ºC to 60 ºC, the α-helix and π-bulge/helix conformations melt into extended conformations (polyproline II and 2.5_1-helix). We calculate the Ψ Ramachandran angle distribution of the PLL peptide bonds from the UV Raman spectra which allows us to calculate the PLL (un)folding energy landscapes along the Ψ reaction coordinate. We observe a basin in the Ψ angle conformational space associated with α-helix and π-bulge/helix conformations and another basin for the extended PPII and 2.5_1-helical conformations.

3.1 INTRODUCTION

The most important outstanding problem in enzymology involves the elucidation of the mechanism whereby proteins fold into their native states.[1-9] It is still impossible to accurately predict protein conformations from their primary sequences, unless these sequences were previously observed. Recently, the first steps in protein folding have been examined in a series of kinetic studies of small peptides in beta hairpins[10-13] and in α-helices.[14-23] Theoretical simulations of (un)folding processes have also elucidated mechanisms of peptide folding dynamics.[24-27] Most recently, sophisticated vibrational spectroscopic kinetic measurements have been used to probe the earliest steps in the secondary structure (un)folding process.[15,28-30]

Poly-L-lysine (PLL) is a useful model system for studying protein conformational changes because it can adopt multiple conformations.[31-43] Its secondary structure has been characterized by numerous spectroscopic methods such as CD, [44] IR,[35] NMR,[45-47] vibrational Raman optical activity,[48-50] VCD,[51] and most recently by UV resonance Raman spectroscopy.[36,38,52] At neutral and low pH values, the lysine side chains are positively charged, and electrostatic repulsions between the side chains make PLL adopt extended conformations. For example, Mikhonin *et al* recently examined the low pH conformations of PLL by using UV resonance Raman spectroscopy (UVRS),[53] and demonstrated that the unfolded PLL peptides exist in an equilibrium between polyprolin II (PPII) and extended 2.5_1-helix conformations. The PPII conformation is stabilized by peptide-water hydrogen bonds,[54-56] whereas the 2.5_1-helix conformation is forced by electrostatic repulsions between neighboring lysine side chains.[53] These electrostatic repulsions can be decreased by adding salt,[32,35,57] or by raising the pH which neutralizes the side chain charges.[31,35,36,38,52,58] The

decreased repulsions alter the PLL conformational equilibrium, and allow the formation of additional conformations.

Previous studies show that ClO_4^- is especially effective in lowering electrostatic repulsions and stabilizing the PLL helical content at low pH.[32,35,57] In this work, we use UVRS to examine the temperature and $NaClO_4$ concentration dependence of the conformations of PLL. We determine the PLL (un)folding energy landscape along the Ψ reaction coordinate by utilizing the methodology developed by Mikhonin *et al*.[59] This energy landscape defines the stability and distribution of PLL between PPII, 2.5_1-helix and α-helix-like conformations.

3.2 MATERIAL AND METHODS

3.2.1 Materials

Poly-L-Lysine HCl was purchased from Sigma (MW_{vis} = 25200, DP_{vis}= 153, MW_{MALLS} = 44000, DP_{MALLS} = 267. Here DP_{vis} and DP_{MALLS} refer to the degree of polymerization measured by viscosity and multi-angle laser light scattering, respectively), and used without further purification. Small aliquots of HCl and sodium hydroxide were used to adjust the solution pH. $NaClO_4$ was purchased from Sigma Chemical Co.

3.2.2 UV Resonance Raman Instrument

The UV resonance Raman (UVRR) instrumentation has previously been described in detail.[60,61] A Coherent Infinity Nd: YAG laser (Coherent, infinity) produced 355 nm, 3-ns pulses at 100 Hz. This beam was Raman shifted to 204 nm (5^{th} anti-Stokes) by using a 1-m tube filled with hydrogen gas (60 psi). The sample was circulated in a free surface, temperature controlled stream. The Raman scattered light was imaged into a subtractive double spectrometer and the UV light was detected by a CCD camera (Princeton Instruments Co.). The UVRR spectra were measured at 1.2 mg/ml peptide concentrations.

3.2.3 CD Measurements

Circular dichroism (CD) spectra were measured by using a Jasco J-710 spectropolarimeter. The spectra were measured by using a temperature controlled 0.2 mm path length cell at 0.64 mg/ml PLL concentrations.

3.3 RESULTS AND DISCUSSION

3.3.1 CD Spectra of PLL in the Absence and Presence of $NaClO_4$

The CD spectrum of PLL (Fig. 3.1A) in the absence of $NaClO_4$ shows a positive band at ~218 nm and a strong negative band centered below 200 nm, which are hallmarks of PPII-like conformations in water.[62,63] However, in the presence of 0.1 M and 0.5 M $NaClO_4$

concentrations, the CD spectra show significant α-helical-like content, as indicated by the negative band at 222 nm. The increasing at 222 nm molar ellipticity indicates that the α-helix-like conformations melt as the temperature increases from 1 to 50 ºC (Fig. 3.1A). The difference in the two melting curves shown in Fig. 3.1B clearly demonstrates that $NaClO_4$ stabilizes α-helix-like structures. In 0.1 M $NaClO_4$, the α-helix-like conformations are almost fully melted by 20 ºC, whereas in presence of 0.5 M $NaClO_4$, they persist until 50 ºC. Previously, it was believed that this increased stability of α-helix-like conformations appears to derive from the electrostatic screening caused by increase ion strength. However, it was found that the ClO_4^- induced α-helix stabilization has been shown to be much larger than other singly charged anions such as Cl^-.[35] So the electrostatic repulsion decrease involves the neutralization by specific ion-pairing of ClO_4^- anions with the lysine $-NH_3^+$ groups.[64-66] This stabilization is consistent with the mechanism Goto *et al*.[65]

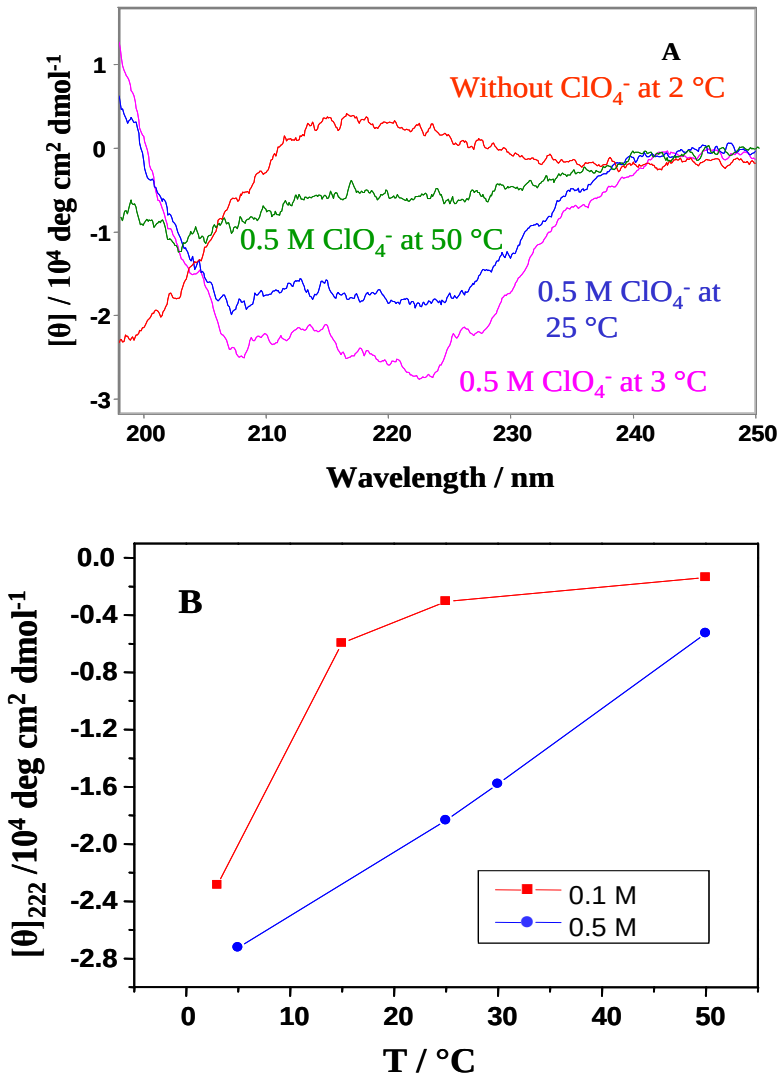

Figure 3.1. (A) CD spectra of PLL (0.64 mg/ml) at PH 6.1 containing 0.5 M $NaClO_4$ at 3 ºC (pink) , 25 ºC (blue), 50 ºC (green); in the absence of $NaClO_4$ at pH 5.5 at 2 ºC (red). (B) Temperature dependence of the molar ellipticities of PLL at 222 nm containing 0.1M and 0.5 M (blue) $NaClO_4$.

3.3.2 204 nm UV Raman Spectra of Unfolded PLL

We examined the unfolded state of PLL at pH 5.5 by measuring the 204 nm UV resonance Raman spectra in the absence of $NaClO_4$. At these conditions, lysine side chains

are fully ionized, so the electrostatic repulsion prevents the formation of α-helix-like conformations. As shown in Fig. 3.2, at pH 5.5 PLL spectra shows an AmI band at 1665 cm^{-1} (predominantly a C=O stretching vibration), while the AmII band is located at 1560 cm^{-1} (C-N stretching coupled with N-H b). The resonance enhancement of the C_α-H b band at ~ 1395 cm^{-1}, results from the coupling between C_α–H b and N-H b motions.[58,67] This coupling is largest for extended β-strand/PPII conformations, and is negligible for α-helix-like conformations. Hence, the C_α-H b band intensity is indicative of conformations other than α-helix, 3_{10}-helix, and π-helix.[38,67]

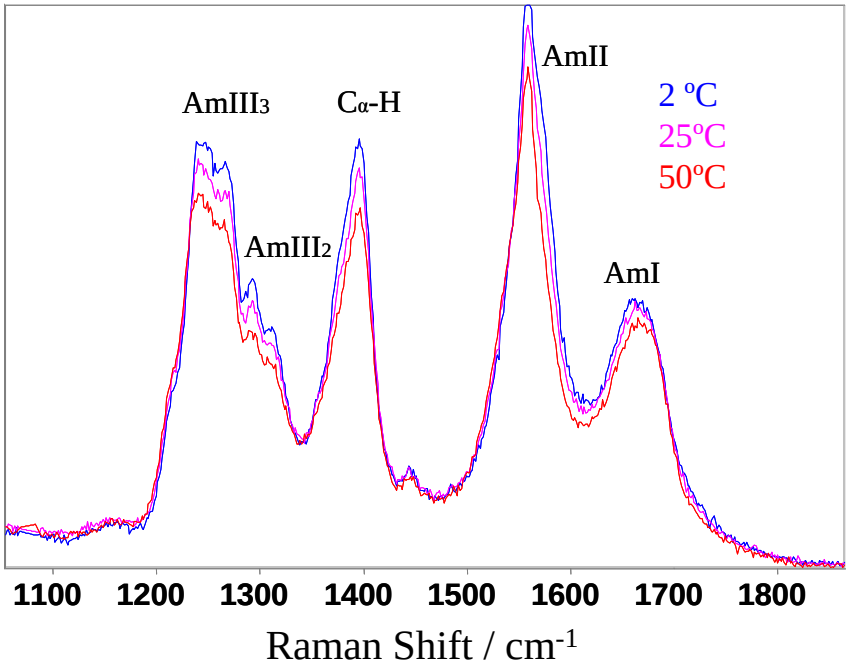

Figure 3.2. 204 nm UVRR spectra of PLL in the absence of $NaClO_4$ at pH 5.5 at 2, 25, and 50 °C.

The conformation sensitive AmIII region between ~1200 cm^{-1} and 1350 cm^{-1} mainly involves N-H bending and C-N stretching motions. This region is complicated and we recently reassigned it in detail.[68-70] The PLL $AmIII_2$ region shows a doublet at 1312 and

1293 cm^{-1}, while the $AmIII_3$ region shows peaks at ~1270, and 1243 cm^{-1}, and a shoulder at 1212 cm^{-1}. Our pH 5.5 PLL spectra are similar to Mikhonin et al's PLL spectra at pH 2.[53] Hence, we conclude that the 1270 cm^{-1} band derives from a 2.5_1-helix conformation, while the 1243 cm^{-1} band derives from the PPII conformation.

3.3.3 Spectral Changes Associated with $NaClO_4$ Induced Folding of PLL

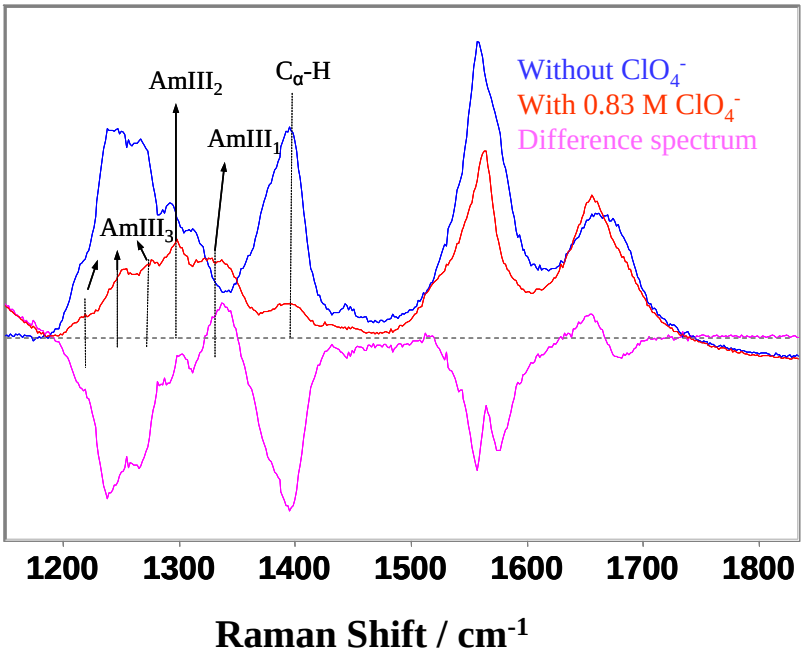

Figure 3.3. 204 nm Raman spectra of PLL in the presence and absence of $NaClO_4$ and their difference spectrum at 1 °C. The AmII band doublet in the difference spectrum results from over-subtraction of the O_2 Raman band.

The Fig. 3.3 Raman spectra show that at 1 ºC, addition of 0.83 M $NaClO_4$ induces the formation of α-helix-like conformations.[58] The PLL spectrum in the presence of $NaClO_4$ shows an AmI band at 1657 cm^{-1}, and an AmII band at 1563 cm^{-1}. A much weaker C_α-H b

band occurs at ~ 1395 cm^{-1}, while the $AmIII_1$ and $AmIII_2$ bands are located at ~1332 and 1297 cm^{-1}, respectively. The conformation sensitive $AmIII_3$ band is decreased in intensity and shows a shoulder at 1218 cm^{-1} and peaks at 1253 and 1276 cm^{-1} with greatly decreased intensities. The difference spectrum (Fig. 3.3) shows troughs at the C_α-H b band position and in the AmIII region which derive from the loss of the PPII and 2.5_1-helix conformations.[58,60,70]

3.3.4 The Assignment of the AmIII Region Bands

We can calculate the pure α-helical PLL spectrum by subtracting the appropriate amount of PPII and 2.5_1-helical PLL from the measured spectrum containing $NaClO_4$.[60,70] The AmIII region of this calculated α-helical-like PLL spectrum can be well modeled by five Gaussian bands (Fig. 3.4). The $AmIII_1$ and $AmIII_2$ bands are located at ~1332 cm^{-1} and ~1300 cm^{-1}, respectively. The $AmIII_3$ region shows three peaks at 1276, 1253, and 1218 cm^{-1} indicating the presence of multiple conformations in equilibrium.

According to the method developed by Mikhonin et al,[59] which calculates the Ψ angle distribution from the $AmIII_3$ band frequency distributions, given the known hydrogen bonding state of the peptide bonds,[14,59,67] the 1276 cm^{-1} and 1253 cm^{-1} $AmIII_3$ bands derive from conformations with average Ramanchandran Ψ angles of -62° and -36°, respectively. The Ψ angles values most likely derive from π-bulge/helix conformation (Ψ = -70° for an ideal π-helix) and an α-helix conformation (Ψ = -47°). It has been found that the Ψ dihedral value of π-bulges, a common deformation of α-helices, shows a distribution of values.[71] Mikhonin et al[72] found Ψ values of π-bulges/helices for the ala-based AP peptide of -58°,

very close to our result. Our Ψ dihedral values also are consistent with numerous recent reports of the π-bulges/helices in model peptides.[22,71,73-76]

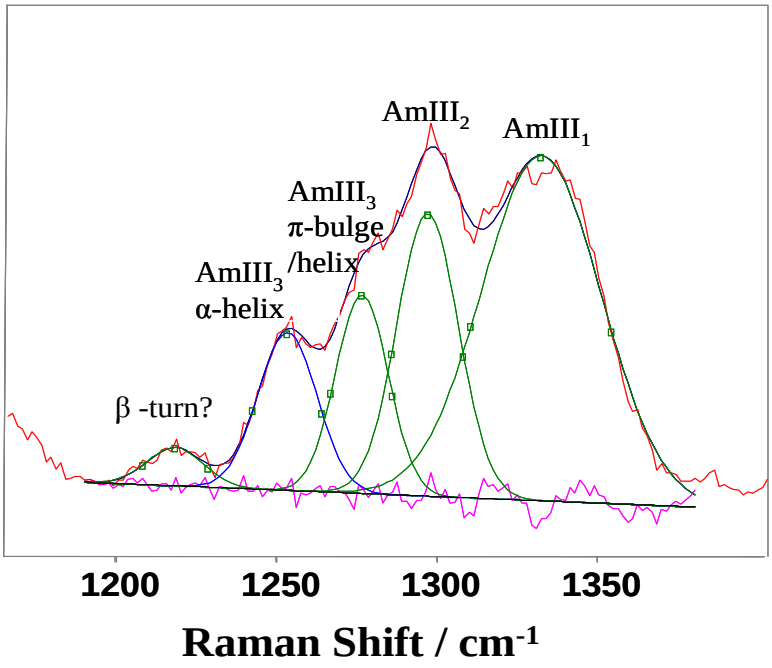

Figure 3.4. Deconvolution of the AmIII region of the calculated helical PLL spectrum into a sum of 5 Gaussian bands. The helix spectrum is calculated by subtracting the appropriate amounts of the spectra with the extended PLL conformation from the measured spectrum.

Table 3.1. Spectral AmIII band assignment of PLL peptide.

Band	Frequency (cm^{-1})
$AmIII_1$	1332
$AmIII_2$	1296
$AmIII_3$ (π-bulge/helix)	1276
$AmIII_3$ (α-helix)	1253
$AmIII_3^t$ (β-turn)	1218

The 1218 cm^{-1} band, which also appears in the spectra of extended PLL (Fig. 3.2), probably derives from β-turn conformations.[59] It could derive from either type I, I', II or II' β-turns et al.[59] These AmIII band assignments are listed in Table 3.1.

3.3.5 Thermal Melting of α-Helix and π-Bulge/Helix Conformations

We examined the temperature dependence of PLL's $NaClO_4$-induced α-helix-like conformations by measuring the 204 nm UV resonance Raman spectra between 1 and 60 ºC (Fig. 3.5). As the temperature increases, we observe a continuous increase in the C_α-H b band intensity and $AmIII_3$ band intensities of the 1270, 1240, and 1220 cm^{-1} bands, indicating melting of the α-helix and π-bulge/helix conformations. The high temperature PLL spectra are similar to PLL spectra in the absence of $NaClO_4$ (Fig. 3.5A). The thermally unfolded conformational equilibrium of PLL in the presence of $NaClO_4$ are similar to the conformational equilibrium for the charged side chains at low ionic strength which are dominated by PPII and 2.5_1-helix conformations.[53] The Raman spectra in Fig. 3.5A show multiple isosbestic points which suggest that the melting of the α-helix-like conformations is a 'two-state' transition from a mixture of α-helix and π-bulge/helix conformations to a mixture of PPII and 2.5_1-helix conformations.

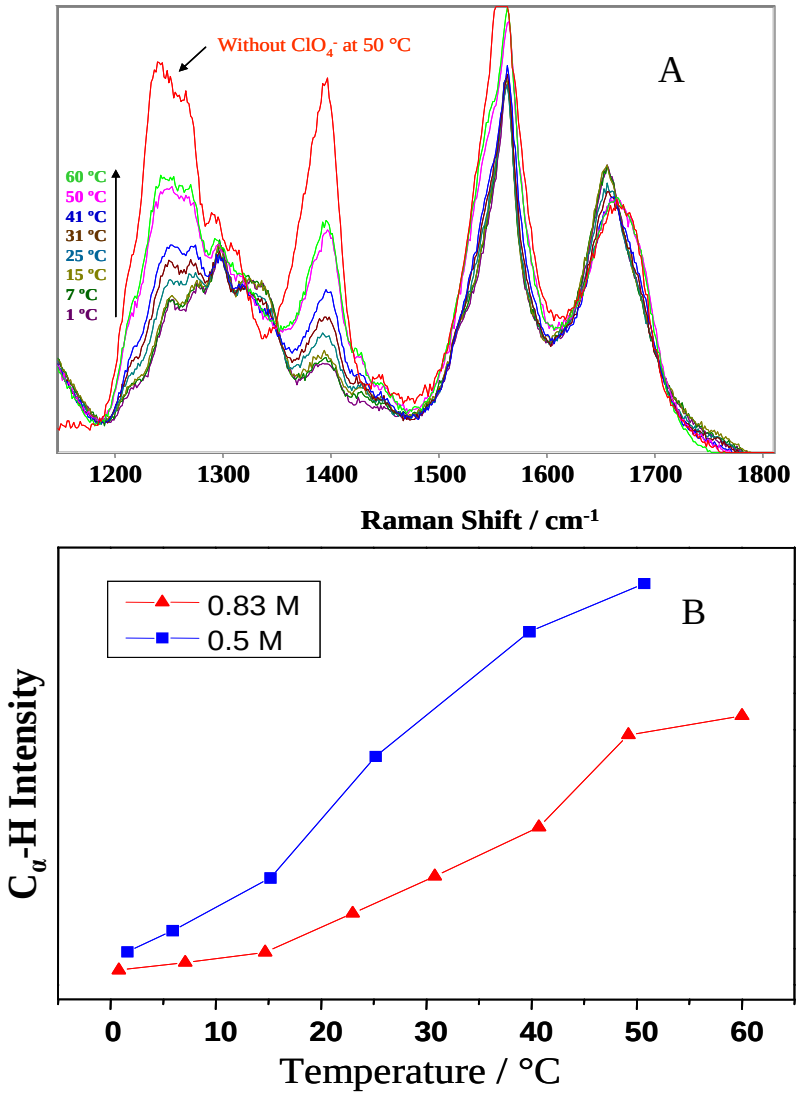

Figure 3.5. (A) Temperature dependence of the UVRR spectra of PLL containing 0.83 M $NaClO_4$ at pH 5.2. The red spectrum is the PLL Raman spectrum without $NaClO_4$ at 50 °C. The temperature induced melting of PLL in the presence of 0.5 M $NaClO_4$ is similar to that in 0.83 M $NaClO_4$. (B) Temperature dependence of C_α-H b band Raman intensity. The spectra were normalized using the ClO_4^- band intensity.

Fig. 3.5B shows the temperature dependence of the C_α-H b band Raman intensity which is a non-α-helical conformational marker.[38,67] The melting curve for the 0.5 M

$NaClO_4$ PLL solution shows a T_m ~35 ºC, while the 0.83 M $NaClO_4$ solution T_m is increased to ~65 ºC. These Raman results agree with the CD results discussed above.

We can estimate the change in the number of α-helical-like amide bonds from the observed increased intensity of the C_α-H b band. For PLL sample containing ClO_4^-, we normalized the amide band intensities with respect to the known Raman cross sections of ClO_4^-. Using Dudik *et al*'s data[77] for the absolute Raman cross section of the 932 cm^{-1} band of ClO_4^- at 204 nm excitation, we calculated the Raman cross sections for the amide bands of PLL in the presence of ClO_4^-:

$$\sigma_A = (I_{Am}\, N_{ClO4^-}\, \sigma_{ClO4^-}) / (n_A\, N_P\, I_{ClO4^-}) \qquad (3.1)$$

where, σ_A and σ_{ClO4^-} are the Raman cross sections of an amide band and the 932 cm^{-1} ClO_4^- band, respectively. N_{ClO4^-} and N_P are number of ClO_4^- and PLL molecules in the scattering volume, respectively. I_{ClO4^-} and I_{Am} are the integrated intensity of the ClO_4^- (932 cm^{-1}) and the amide bands, respectively. n_A is the number of amide peptide bonds in PLL contributing to the intensity of the Amide band.

In cases where ClO_4^- is not present, the amide band intensities of the unfolded state were normalized to the AmI band intensity, which we earlier showed was the least sensitive to secondary structura; changes.[58,60,67,70] Using the AmI band cross section, we can calculate the C_α-H b band cross sections in the absence of $NaClO_4$. The calculated cross sections of PLL amide bands in the extended conformations are listed in Table 3.2.

From the C_α-H b band cross sections we can calculate the number of non-α-helical amide bonds in PLL as:

$$n_A = (I_{C\alpha H}\, N_{ClO4^-}\, \sigma_{ClO4^-}) / (\sigma_{C\alpha H}\, N_P\, I_{ClO4^-}) \qquad (3.2)$$

We calculate that at 1 ºC, in the presence of 0.83 M $NaClO_4$, PLL has an 86% α-helix-like content.

We can calculate the number of α-helix and π-bulge/helix peptide bonds which melt as:

$$\delta n_A = (-\delta I_{C\alpha H}\, N_{ClO4}\text{-}\, \sigma_{ClO4}\text{-}) / (\sigma_{C\alpha H}\, N_P\, I_{ClO4}\text{-}) \qquad (3.3)$$

Where δn_A is number of α-helix and π-bulge bonds lost or gained and $\delta I_{C\alpha H}$ is the change in the normalized integrated C_α-H bending band intensity. In 0.83 M $NaClO_4$, the integrated intensity of the C_α-H b band at 50 ºC is 32% larger than that at 1 ºC. The helix melting curves are displayed in Fig. 3.6.

Table 3.2. The calculated cross section of PLL peptide in extended conformations.

Band	Cross section (mbarn molecule^{-1} sr^{-1})
C_α-H bending	60
AmI	75

Our results agree with Jiji *et al*'s[52] data that at pH 11.6 at 10 °C, PLL shows a ~85% α-helical content. At pH 11.6, the lysine side chains are neutralized, which eliminates the electrostatic repulsions which destabilize the α-helices at lower pH. The fact that at pH 5.2 addition of 0.83 M $NaClO_4$ results in ~86% α-helical-like content suggests that the charged side chains are neutralized by $NaClO_4$.[65,66,78,79]

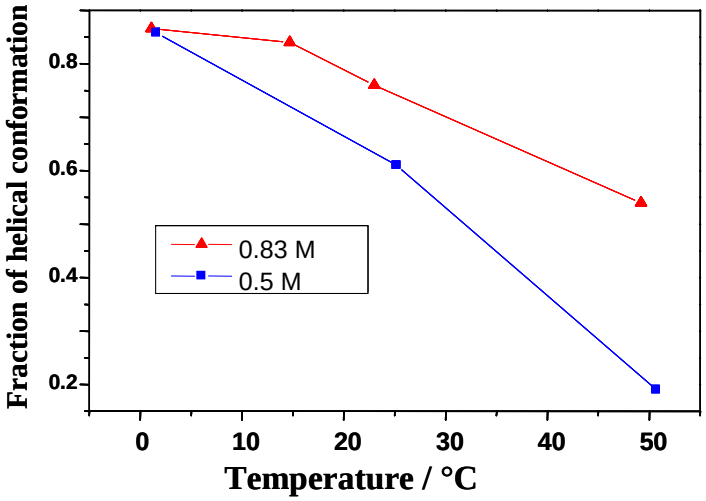

Figure 3.6. Temperature dependence of the fraction of α-helix-like conformations in the presence of 0.83 and 0.5 M $NaClO_4$ at pH 5.2.

3.3.6 Temperature Dependence of Ψ Population Distributions of PLL

The $AmIII_3$ bands are significantly broadened comparing to the $AmIII_3$ band of peptide crystals.[14] The band breadth is largely due to an inhomogeneous distribution of Ψ angles. The intrinsic homogeneous line width of the band was estimated from UV Raman spectra of crystal of Gla-Ala-Leu.[38] We calculated the inhomogeneous frequency distributions of the observed $AmIII_3$ bands and the Ψ dihedral angle distributions of the PLL peptide bonds (Fig. 3.7) was calculated by using the methodology developed by Mikhonin et al.[14,53,59] (We assume equal Raman cross sections for two α-helix-like conformations, PPII and 2.5_1-helix conformations.)

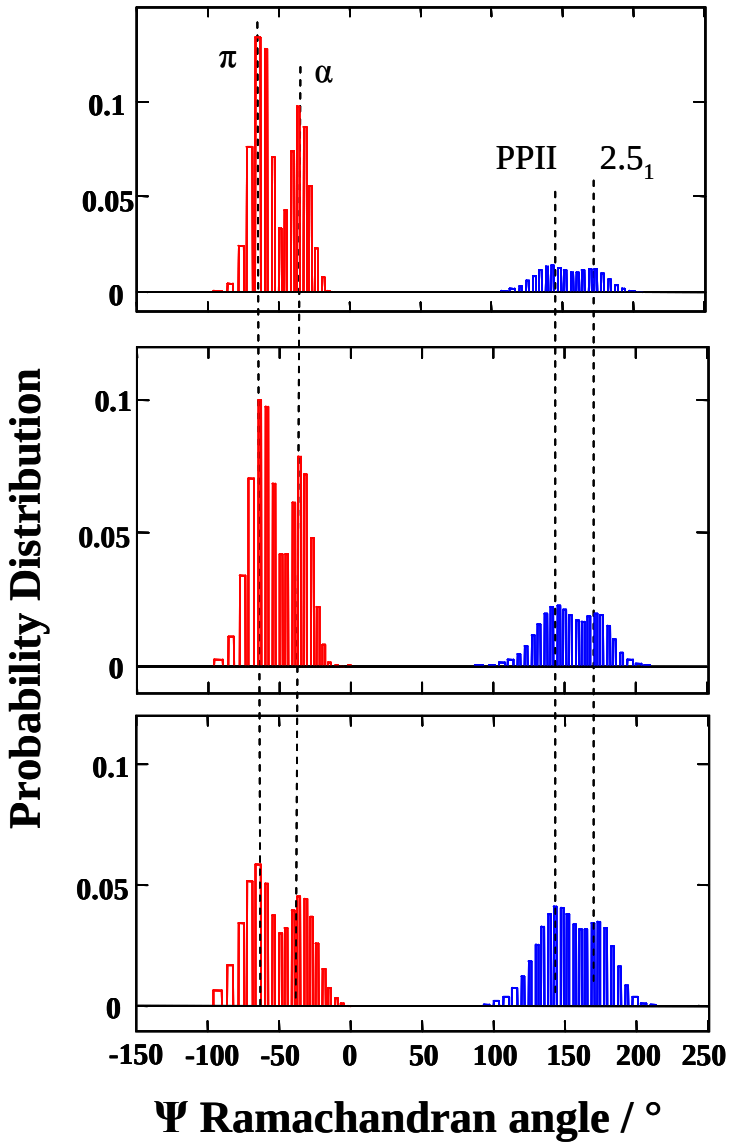

Figure 3.7. Temperature dependence of Ψ angle distribution of PLL containing 0.83 M $NaClO_4$ at 1 °C, 25 °C, and 50 °C.

In the helical region (red), we calculate high concentrations of π-helical (Ψ = -80 to -50˚) and α-helical (Ψ = -50 to -15˚) conformations. Similarly, in the extended, non-helical region (blue) we observe significant populations of PPII (Ψ = 110 to 160˚) and 2.5_1-helix (Ψ = 150 to 200˚) conformations.

As discussed above, the 1218 cm^{-1} $AmIII_3$ band likely derives from a β-turn conformation. β-turns, which result from water inserted hydration of α-helices, was proposed by Sundaralingam et al to be intermediates in the helix-coil transition pathway.[80] Unfortunately, a lack of suitable models limits our ability to quantitate the contributions of β-turn at 1218 cm^{-1}.

As the temperature increases from 1 to 50 ˚C, the concentrations of the α-helix-like conformations decrease, while the PPII and 2.5_1-helix conformations increase. However, the relative population ratios of the PPII to 2.5_1-helix, and the α-helix to π-bulge/helix conformations show little change. This suggests that these pairs of conformationally similar structures are separated by small energy differences. This result further confirms that PLL unfolds by a 'two-state' mechanism where it goes from compact α-helix and π-bulge/helix conformations to extended PPII and 2.5_1-helices.

3.3.7 Conformational Free Energy Landscapes for PLL (un)Folding

The probability that the PLL peptide bond is found at a particular Ψ_i angle state depends on the Gibbs free energy (G_i) of this Ψ_i dihedral angle. Assuming equal degeneracies of the different conformations, the energy difference between a conformation at Ψ_i angle and another conformation at Ψ_0 angle is

$$\Delta G_{i-0} = -N_A k_B T \ln \frac{n(\psi_i)}{n(\psi_0)} \qquad (3.4)$$

where N_A is the Avogadro's number, and k_B is the Boltzmann constant, T is the temperature, $\frac{n(\psi_i)}{n(\psi_0)}$ is the ratio of populations with Ramachandran angles Ψ_i and Ψ_0.

Using eq. (3.4), we calculate the Gibbs free energies of the populated equilibrium conformations relative to that of the π-bulge conformation (Fig. 3.8). We find an energy landscape with two basins. One is associated with the α-helix and π-bulge/helix conformations, while the other is associated with the PPII and 2.5_1-helix conformations.

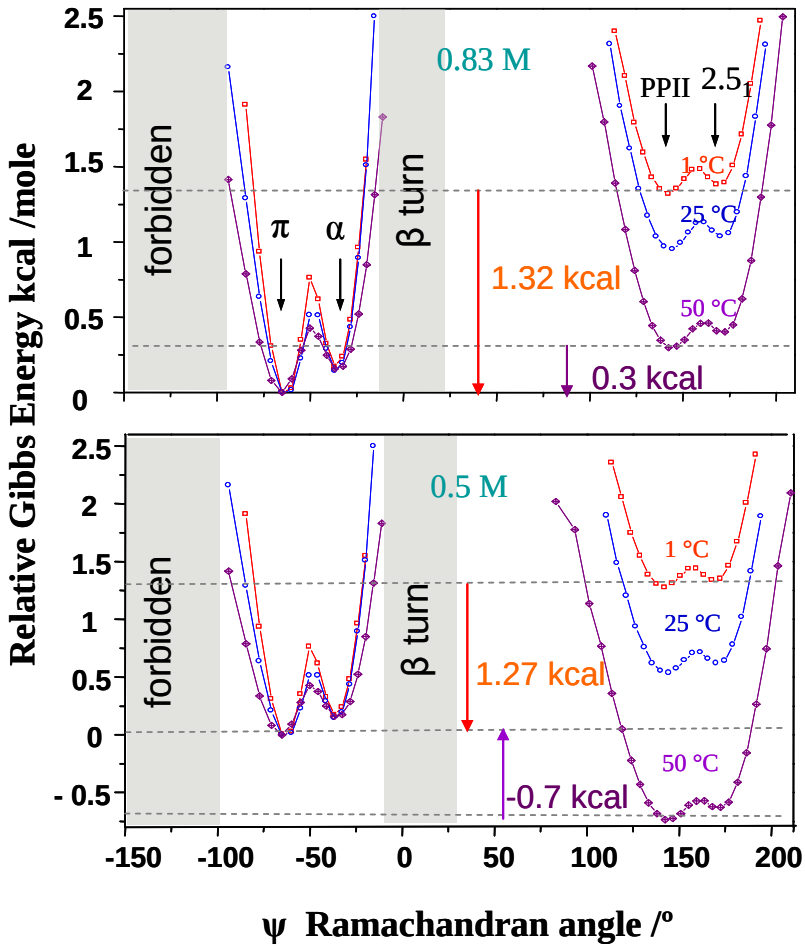

Figure 3.8. Estimated Gibbs free energy landscape for PLL (1.2 mg/ml) at 0.83 M and 0.5 M $NaClO_4$ concentration at 1°C (red), 25°C (blue) and 50°C (purple).

At 1 ˚C, in the presence of 0.83 M $NaClO_4$, the α-helix conformational energy lies above that of the π-bulge/helix by only ~170 cal/mol, and the energy barrier between the α-helix and the π-bulge/helix is ~760 cal/mol higher than the π-bulge minimum. This barrier decreases somewhat as the temperature increases.

Similarly, at 1 ˚C the 2.5_1-helix conformational energy lies ~64 cal/mol above that of PPII conformation. Previously, Mikhonin et al found at pH 2 a similar energy difference of ~74 cal/mol between the PPII and 2.5_1-helix conformations.[53]

At 1 ˚C, the π-bulge is stabilized over the PPII conformation by ~1.32 kcal/mol and ~1.27 kcal/mol energy in the presence of 0.83 M $NaClO_4$ and 0.5 M $NaClO_4$, respectively. As the temperature increases from 1 to 50 ˚C, the PLL PPII and 2.5_1-helix conformational energy decrease relative to that of the π-bulge. For 0.83 M $NaClO_4$, we observe that the PPII/2.5_1-helix conformational energy is greater than that of α-helix-like conformation until the temperature increases to 50 ˚C. In contrast, the energy of the extended PPII conformation at 50 ˚C in 0.5 M $NaClO_4$ is ~0.7 kcal/mole below that of the α-helix conformation.

3.3.8 Thermodynamic Parameters for PLL 'Two-State' Transition

Assuming that the enthalpy difference is independent of temperature, we can estimate the enthalpy and entropy changes for the α-helix-like conformations melting which are $\Delta H = 12 \pm 1.6$ kcal/mole, $\Delta S = 39 \pm 5$ cal/mol·K in the presence of 0.5 M $NaClO_4$, and $\Delta H = 6.1 \pm 0.8$ kcal/mol, $\Delta S = 19 \pm 3$ cal/mol·K in the presence of 0.83 M $NaClO_4$.

The change in the slope of the melting curve as the $NaClO_4$ concentration increases from 0.5 to 0.83 M allows us to calculate that the magnitude of both ΔH and ΔS for melting

decreases ~2-fold. We observe an apparent loss of cooperativity in the thermal unfolding transition at high $NaClO_4$ concentrations.

We expect that much of this change derives from the water solvent. Surprisingly, little change is observed in water activity between these $NaClO_4$ cconcentraion.[81] Thus, the change in the thermodynamic parameters must derive from energetic perturbations in the conformations of the two states. To have additional insight, we need additional structural insights into determine the origin of these changes.

3.4 CONCLUSIONS

The presence of $NaClO_4$ induces a conformational change in PLL from extended PPII/2.5_1-helix conformations to folded α-helix and π-bulge/helix conformations. As the temperature increases, the compact helical conformations melt to extended conformations. Increasing the $NaClO_4$ concentrations shifts the T_m of the unfolding transition to higher values indicating an increased stability of the helical conformations at higher $NaClO_4$ concentration. The Raman isosbestic points suggest that the PLL melting is a 'two-state' transition from a mixture of compact helical conformations to extended PPII and 2.5_1-helix conformations. We were able to roughly estimate the enthalpy and entropy change of the melting transition. We also calculated the energy landscape along the Ψ folding coordinate. The neutralization of the lysine $-NH_3^+$ groups by efficient ion pairing with ClO_4^- dramatically impacts the energy landscape which changes the equilibrium peptide conformations.

3.5 REFERENCES

(1) Creighton, T. E. *Protein Folding*; W. H. Freeman: New York, 1992.

(2) Baldwin, R. L.; Rose, G. D. *Trends Biochem. Sci.* **1999**, *24*, 26-33.

(3) Baldwin, R. L.; Rose, G. D. *Trends Biochem. Sci.* **1999**, *24*, 77-83.

(4) Dill, K. A. *Protein Sci.* **1999**, *8*, 1166-1180.

(5) Dobson, C. M.; Sali, A.; Karplus, M. *Angew. Chem. Int. Ed.* **1998**, *37*, 868-893.

(6) Oliveberg, M.; Tan, Y.-J.; Silow, M.; Fersht, A. R. *J. Mol. Biol.* **1998**, *277*, 933-943.

(7) Wright, P. E.; Dyson, H. J. *J. Mol. Biol.* **1999**, *293*, 321-331.

(8) Myers, J. K.; Oas, T. G. *Annu. Rev. Biochem.* **2002**, *71*, 783-815.

(9) Alm, E.; Baker, D. *Proc. Natl. Acad. Sci. U. S. A.* **1999**, *96*, 11305-11310.

(10) Blanco, F. J.; Jimenez, M. A.; Herranz, J.; Rico, M.; Santoro, J.; Nieto, J. L. *J. Am. Chem. Soc.* **1993**, *115*, 5887-5888.

(11) Colley, C. S.; Griffiths-Jones, S. R.; George, M. W.; Searle, M. S. *Chem. Commun.* **2000**, 593-594.

(12) Dinner, A. R.; Lazaridis, T.; Karplus, M. *Proc. Natl. Acad. Sci. U. S. A.* **1999**, *96*, 9068-9073.

(13) Fesinmeyer, R. M.; Hudson, F. M.; Andersen, N. H. *J. Am. Chem. Soc.* **2004**, *126*, 7238-7243.

(14) Asher, S. A.; Mikhonin, A. V.; Bykov, S. B. *J. Am. Chem. Soc.* **2004**, *126*, 8433-8440.

(15) Huang, C.-Y.; Klemke, J. W.; Getahun, Z.; DeGrado, W. F.; Gai, F. *J. Am. Chem. Soc.* **2001**, *123*, 9235-9238.

(16) Lednev, I. K.; Karnoup, A. S.; Sparrow, M. C.; Asher, S. A. *J. Am. Chem. Soc.* **2001**, *123*, 2388-2392.

(17) Ramajo, A. P.; Petty, S. A.; Starzyk, A.; Decatur, S. M.; Volk, M. *J. Am. Chem. Soc.* **2005**, *127*, 13784-13785.

(18) Mikhonin, A. V.; Asher, S. A. *J. Phys. Chem. B* **2005**, *109*, 3047-3052.

(19) Thompson, P. A.; Munoz, V.; Jas, G. S.; Henry, E. R.; Eaton, W. A.; Hofrichter, J. *J. Phys. Chem. B* **2004**, *104*, 378-389.

(20) Fesinmeyer, R. M.; Peterson, E. S.; Dyer, R. B.; Andersen, N. H. *Protein Sci.* **2005**, *14*, 2324-2332.

(21) Luo, P.; Baldwin, R. L. *Proc. Natl. Acad. Sci. U. S. A.* **1999**, *96*, 4930-4935.

(22) Shirley, W. A.; Brooks, C. L. I. *Proteins: Struct. Funct. Genet.* **1997**, *28*, 59-71.

(23) Millhauser, G. I.; Stenland, C. J.; Hanson, P.; Bolin, K. A.; van de Ven, F. J. M. *J. Mol. Biol.* **1997**, *267*, 963-974.

(24) Shakhnovich, E. I. *Curr. Opin. Struct. Biol.* **1997**, *7*, 29-40.

(25) Karplus, M.; Sali, A. *Curr. Opin. Struct. Biol.* **1995**, *5*, 58-73.

(26) Dill, K. A.; Chan, H. S. *Nature Struct. Biol.* **1997**, *4*, 10-19.

(27) Bryngelson, J. D.; Onuchic, J. N.; Socci, N. D.; Wolynes, P. G. *Proteins: Struct. Funct. Genet.* **1995**, *21*, 167.

(28) Munoz, V.; Thompson, P. A.; Hofrichter, J.; Eaton, W. A. *Nature* **1997**, *390*, 196-199.

(29) Williams, S.; Causgrove, T. P.; Gilmanshin, R.; Fang, K. S.; Callender, R. H.; Woodruff, W. H.; Dyer, R. B. *Biochemistry* **1996**, *35*, 691-697.

(30) Lednev, I. K.; Karnoup, A. S.; Sparrow, M. C.; Asher, S. A. *J. Am. Chem. Soc.* **1999**, *121*, 4076-4077.

(31) Davidson, B.; Fasman, G. D. *Biochemistry* **1967**, *6*, 1616-1629.

(32) Dearborn, D. G.; Wetlaufer, D. B. *Biochem. Biophys. Res. Commun.* **1970**, *39*, 314-320.

(33) Drake, A. F.; Siligardi, G.; Gibbons, W. A. *Biophys. Chem.* **1988**, *31*, 143-146.

(34) Makarov, A. A.; Adzhubel, I. A.; Protasevich, I. I.; Lobachov, V. M.; Fasman, G. D. *Biopolymers* **1994**, *34*, 1123.

(35) Painter, P. C.; Koenig, J. L. *Biopolymers* **1976**, *15*, 229-240.

(36) Song, S.; Asher, S. A. *J. Am. Chem. Soc.* **1989**, *111*, 4295-4305.

(37) Tiffany, M. L.; Krimm, S. *Biopolymers* **1969**, *8*, 347-359.

(38) Wang, Y.; Purrello, R.; Jordan, T.; Spiro, T. C. *J. Am. Chem. Soc.* **1991**, *113*, 6359-6368.

(39) Yaron, A.; Katchalski, E.; Berger, A.; Fasman, G. D.; Sober, H. A. *Biopolymers* **1971**, *10*, 1107.

(40) Yu, N. T. *Crit. Rev. Biochem.* **1977**, *4*, 229.

(41) Yu, T. J.; Lippert, J. L.; Peticolas, W. L. *Biopolymers* **1973**, *12*, 2161-2176.

(42) Vorobjev, Y. N.; Scheraga, H. A. *J. Phys. Chem.* **1995**, *99*, 7180-7187.

(43) Ashton, L.; Barron, L. D.; Czarnik-Matusewicz, B.; Hecht, L.; Hyde, J.; Blanch, E. W. *Mol. Phys.* **2006**, *104*, 1429-1445.

(44) Tiffany, M. L.; Krimm, S. *Biopolymers* **1968**, *6*, 1379-1382.

(45) Darke, A.; Finer, E. G. *Biopolymers* **1975**, *14*, 441.

(46) Joubert, F. J. L., N. Scheraga, H. A *Physiol. Chem. Phys. Med. NMR* **1969**, *1*, 348.

(47) Perly, B.; Chevalier, Y.; Chachaty, C. *Macromolecules* **1981**, *14*, 969.

(48) McColl, I. H.; Blanch, E. W.; Gill, A. C.; Rhie, A. G. O.; Ritchie, M. A.; Hecht, L.; Nielsen, K.; Barron, L. D. *J. Am. Chem. Soc.* **2003**, *125*, 10019-10026.

(49) Barron, L. D.; Hecht, L.; Blanch, E. W.; Bell, A. F. *Prog. Biophys, Mol. Biol.* **2000**, *73*, 1-49.

(50) Wilson, G.; Hecht, L.; Barron, L. D. *J. Chem. Soc., Faraday Trans.* **1996**, *92*, 1503-1510.

(51) Keiderling, T. A.; Silva, R. A.; Yoder, G.; Dukor, R. K. *Bioorg. Med. Chem.* **1999**, *7*, 133.

(52) JiJi, R. D.; Balakrishnan, G.; Hu, Y.; Spiro, T. G. *Biochemistry* **2006**, *45*, 34-41.

(53) Mikhonin, A. V.; Myshakina, N. S.; Bykov, S. V.; Asher, S. A. *J. Am. Chem. Soc.* **2005**, *127*, 7712-7720.

(54) Shi, Z.; Chen, K.; Liu, Z.; Kallenbach, N. R. *Chem. Rev.* **2006**, *106*, 1877-1897.

(55) Eker, F.; Griebenow, K.; Schweitzer-Stenner, R. *J. Am. Chem. Sco.* **2003**, *125*, 8178-8185.

(56) Poon, C. D.; Samulski, E. T. *J. Am. Chem. Soc.* **2000**, *122*, 5642-5643.

(57) Bello, J. *Biopolymers* **1992**, *32*, 185-188.

(58) Chi, Z.; Chen, X. G.; Holtz, J. S. W.; Asher, S. A. *Biochemistry* **1998**, *37*, 2854-2864.

(59) Mikhonin, A. V.; Bykov, S. V.; Myshakina, N. S.; Asher, S. A. *J. Phys. Chem. B* **2006**, *110*, 1928-1934.

(60) Lednev, I. K.; Karnoup, A. S.; Sparrow, M. C.; Asher, S. A. *J. Am. Chem. Soc.* **1999**, *121*, 8074-8086.

(61) Bykov, S. V.; Lednev, I. K.; Ianoul, A.; Mikhonin, A. V.; Asher, S. A. *Appl. Spectrosc.* **2005**, *59*, 1541-1552.

(62) Tiffany, M. L.; Krimm, S. *Biopolymers* **1972**, *11*, 2309-2316.

(63) Woody, R. W. *Adv. Biophys. Chem* **1992**, *2*, 37-79.

(64) Shibue, M.; Mant, C. T.; Hodges, R. S. *J. Chromatogr. A* **2005**, *1080*, 49-57.

(65) Goto, Y.; Takahashi, N.; Fink, A. L. *Biochemistry* **1990**, *29*, 3480-3488.

(66) Ebert, G.; Kuroyanagi, Y. *Polymer* **1982**, *23*, 1154-1158.

(67) Asher, S. A.; Ianoul, A.; Mix, G.; Boyden, M. N.; Karnoup, A.; Diem, M.; Schweitzer-Stenner, R. *J. Am. Chem. Soc.* **2001**, *123*, 11775-11781.

(68) Lee, S.; Krimme, S. *Biopolymers* **1998**, *46*, 283-317.

(69) Diem, M.; Lee, O.; Roberts, G. M. *J. Phys. Chem.* **1992**, *96*, 548-554.

(70) Mikhonin, A. V.; Ahmed, Z.; Ianoul, A.; Asher., S. A. *J. Phys. Chem. B* **2004**, *108*, 19020-19028.

(71) Cartailler, J.-P.; Luecke, H. *Structure* **2004**, *12*, 133-144.

(72) Mikhonin, A. V.; Asher, S. A. *J. Am. Chem. Soc.* **2006**, *Accepted*.

(73) Sudha, R.; Kohtani, M.; Breaux, G. A.; Jarrold, M. F. *J. Am. Chem. Soc.* **2004**, *126*, 2777-2784.

(74) Armen, R.; Alonso, D. O. V.; Daggett, V. *Protein Sci.* **2003**, *12*, 1145-1157.

(75) Mahadevan, J.; Lee, K.-H.; Kuczera, K. *J. Phys. Chem. B* **2001**, *105*, 1683-1876.

(76) Fodje, M. N.; Al-Karadaghi, S. *Protein Eng.* **2002**, *15*, 353-358.

(77) Dudik, J. M.; Johnson, C. R.; Asher, S. A. *J. Chem. Phys.* **1985**, *82*, 1732.

(78) Hoshino, M.; Goto, Y. *J. Biochem* **1994**, *116*, 910-915.

(79) Ebert, G.; Kuroyanagi, Y. *Polymer* **1982**, *23*, 1147-1153.

(80) Sundaralingam, M.; Sekharudu, Y. C. *Science* **1989**, *244*, 1333-1337.

(81) Dutkiewicz, E.; Jakubowska, A. *ChemPhysChem* **2002**, *3*, 221-224.

CHAPTER 4

UV Resonance Raman Study of Sidechain Electrostatic Control of Poly-L-Lysine Conformation

This Chapter was published in *Journal of Physical Chemistry B*, 2011, *115*, 4252-4258. The co-authors are Lu Ma, Zeeshan Ahmed, Sanford Asher.

4.0 UV RESONANCE RAMAN STUDY OF SIDE CHAIN ELECTROSTATIC CONTROL OF POLY-L-LYSINE CONFORMATION

We used 204 nm excitation UV Resonance Raman (UVRR) spectroscopy to examine the role of side chain electrostatic interactions in determining the conformation of poly-L-lysine (PLL). We examined the pH and ionic strength dependence of the UVRR. The pH dependence of PLL UVRR spectra between pH 7.1 and 11.7 cannot be described by a two-state model, but requires at least one additional state. The $AmIII_3$ region fitting with pH 7.1 and 11.7 basis spectra reveals a small pH induced decrease in the relative fraction of the 2.5_1-helix conformation compared to the PPII conformation. We performed a 2D general correlation analysis on the PLL pH dependence UVRR spectra. The asynchronous spectrum shows enhanced spectral resolution. The 2D asynchronous spectrum reveals multiple components in the C_α-H b band and the AmII band whose origins are unclear. The cross peaks in the 2D asynchronous spectrum between the AmIII band and the other bands reveals that increasing pH induces three new structures: π-helix, α-helix and some turn structure. We find that 2.5 M NaCl does not change the equilibrium between the PPII and 2.5_1-helix conformations by screening sidechain electrostatic repulsion. The result indicates that NaCl does not penetrate the region between the sidechain and the peptide backbone. We also compared PLL conformations induced by high pH to that induced by 0.8 M ClO_4^-. Both conditions induce α-helix-like conformations. 0.8 M ClO_4^- induces 6% more α-helix-like

conformations than at pH 12.4. Higher pH gives rise to longer α-helices and less turn structures.

4.1 INTRODUCTION

Developing an understanding of the mechanism of protein folding is one of the most important unsolved problems in structural biology.[1-5] The major underlying assumption is that the protein native structure is the thermodynamically most stable structure.[6-8] Further, this, native structure is thought to be defined by the primary amino acid sequence and the protein solution environment. Thus, the protein primary sequence is expected to contain all of the information necessary to specify the protein native structure and its folding mechanisms.

Determining the mechanism of protein folding involves determining the energy landscape along the folding coordinates and determining the folding process intermediates.[9] Computational modeling has made important contributions to the understanding of protein folding mechanisms.[10-12] The conformational space accessible to a peptide can now be searched by molecular dynamics. The mechanisms of protein folding have been probed experimentally by techniques such as CD, NMR, IR, Raman and a variety of temperature jump spectroscopies.

In the work here we are studying the conformational transitions of poly-L-lysine (PLL) induced by solution pH and salt concentration changes. At neutral and low pH values, the lysine side chains are positively charged. We previously demonstrated that under these conditions PLL exists in an unfolded state in an equilibrium between a PPII and 2.5_1-helix

conformation.[13] The PPII conformation is mainly stabilized by peptide-water hydrogen bonding,[14] whereas the 2.5_1-helix conformation is stabilized by electrostatic repulsion between lysine side chains.[13,15] Raising the pH neutralizes the side chains, and PLL folds into compact α-helix-like conformations.

Charged PLL also forms α-helix-like conformations in the presence of ClO_4^-; Ma et al. observed that in the presence of ClO_4^-, PLL adopts multiple α-helix-like conformations including pure α-helix and π-bulge/helix conformations.[16] High temperature converts the high pH folded PLL to a β-sheet conformation.[17] Recently, Jiji et al's temperature-jump UVRR spectroscopy study of PLL indicated that the PPII and extended β-strand conformations may be involved as intermediates in the α-helix to β-sheet conformational transition.[18]

In our UVRR studies of the salt concentration dependence of PLL conformations we surprisingly find that high concentrations of NaCl negligibly impact the low pH PLL conformations. This indicates that NaCl does not effectively screen PLL sidechain repulsions. We discuss the impact of this result on the partitioning of salt in the region between the sidechains and the peptide backbone.

4.2 EXPERIMENTS AND METHODS

4.2.1 Materials

Poly-L-Lysine HCl (MW_{vis} = 20900, DP_{vis}= 127, MW_{MALLS} = 11400, DP_{MALLS} = 69, where DP_{vis} and DP_{MALLS} refer to the degree of polymerization measured by viscosity and multi-angle laser light scattering, respectively) was obtained from Sigma and used without

further purification. $NaClO_4$ and NaOD (40% wt. solution in D_2O, 99 + atom %D), purchased from Sigma, were used without further purification. The Ac-KKKKKKKKKK-NH_2 peptide (K10) was obtained from the Pittsburgh Peptide Synthesis Facility (>98% pure). Small aliquots of concentrated fresh NaOH and NaOD solutions were used to adjust the solution pH and pD values.

4.2.2 UVRR Instrument and Experiment

We used a Coherent Infinity Nd: YAG laser (Coherent, Inc.) to produce 355 nm light pulses (3^{rd} harmonic) at a 100 Hz repetition rate with a pulse width of 3 ns. This beam was Raman shifted to 204 nm (5^{th} anti-Stokes) by using a 1-m tube filled with hydrogen (60 psi), giving 2 mW average power.[19,20] A Pellin Broca prism was used to select the 204 nm excitation. The sample was circulated in a free surface, temperature controlled stream to avoid heating or accumulation of photochemical degradation products formed by the high peak power laser pulses. The Raman scattered light was imaged into a subtractive double spectrometer.[19] The dispersed UV light was detected by the liquid nitrogen cooled, Unichrome coated back-thinned CCD with a reported >30% quantum efficiency in the deep UV (Princeton Instruments Spec-10:400B).

The UVRR spectra of 1 mg/ml PLL and K10 H_2O solution were measured at various pH values at 10 ºC. ClO_4^- could not be used as an internal standard, since it induces α-helical conformations.[16] Instead, all Raman spectra were normalized to the integrated intensities of the AmI bands, because they show the least sensitivity to secondary structural changes.[21]

The D_2O PLL solutions utilized 2 mg/ml concentrations. The UVRR spectra of PLL in D_2O were measured at pD 6.5 and 11.5 at 10 ºC. Spectra were normalized to the integrated intensity of the AmI' band.

4.2.3 2D Correlation Analysis

The measured UVRR spectra at different pH values were fit by using the peak fitting routine in GRAMS software (Thermo Galactic, Grams version 8). The fit spectra were used to construct the data matrices for the 2D correlation analysis. Synchronous and asynchronous correlation intensities were computed from the fitted spectra at different pH values by using a Matlab program that we wrote that utilized Noda's generalized 2D correlation algorithm.[22,23]

4.3 RESULTS AND DISCUSSION

4.3.1 pH Dependence of PLL UVRR Spectra in H_2O

Fig. 4.1A shows the pH dependence of the 204 nm UVRR spectrum of PLL. The spectra show the four characteristic UVRR bands of the peptide bond: the AmI band located at ~ 1660 cm^{-1}(mainly C=O s), the AmII band at ~ 1567 cm^{-1} (mainly out of phase combination of C-N s and N-H b), the ~1400 cm^{-1} C_α-H b band (complex vibration involving C_α-H b and N-H b motions), and the AmIII bands occurring in the range of 1200 to 1350 cm^{-1} (mainly involving N-H b and C-N s).

As the pH increases, the AmII, the C_α-H b and the AmIII band intensities decrease, which indicates formation of α-helical-like conformations. For 204 nm excitation, the α-helix UVRR cross sections are smaller than for extended conformations, due to the hypochromism that results from α-helix excitonic interactions between the peptide bond π-π* electronic transitions.[24,25] The C_α-H b band shows an additional intensity decrease relative to the AmII and AmIII bands because the C_α-H b bands are only resonantly enhanced for PPII-like, β-sheet, and β-strand-like conformations, but not for α-helix-like conformations.

As the pH increases, the AmI band downshifts by 14 cm^{-1} and its bandshape narrows and it becomes more symmetric. The AmI band shows a clear isosbestic point, presumably indicating a transition between only two different carbonyl hydrogen bonding states. The smaller AmI high pH α-helix bandwidths result from the better defined α-helix conformation hydrogen bonding, while the AmI frequency decrease results from stronger α-helix carbonyl hydrogen bonding.

The AmII band downshifts 12 cm^{-1} as the pH increases and the α-helix conformation becomes dominant. Similar AmII band frequency shifts have previously been observed in peptides and proteins upon the conformational shift from PPII-like to α-helix conformations.[20,21] Although there have been numerous studies of the conformation frequency dependence of the AmII band, there is as yet no simple explanation of the origin of these AmII band downshifts.[26-29]

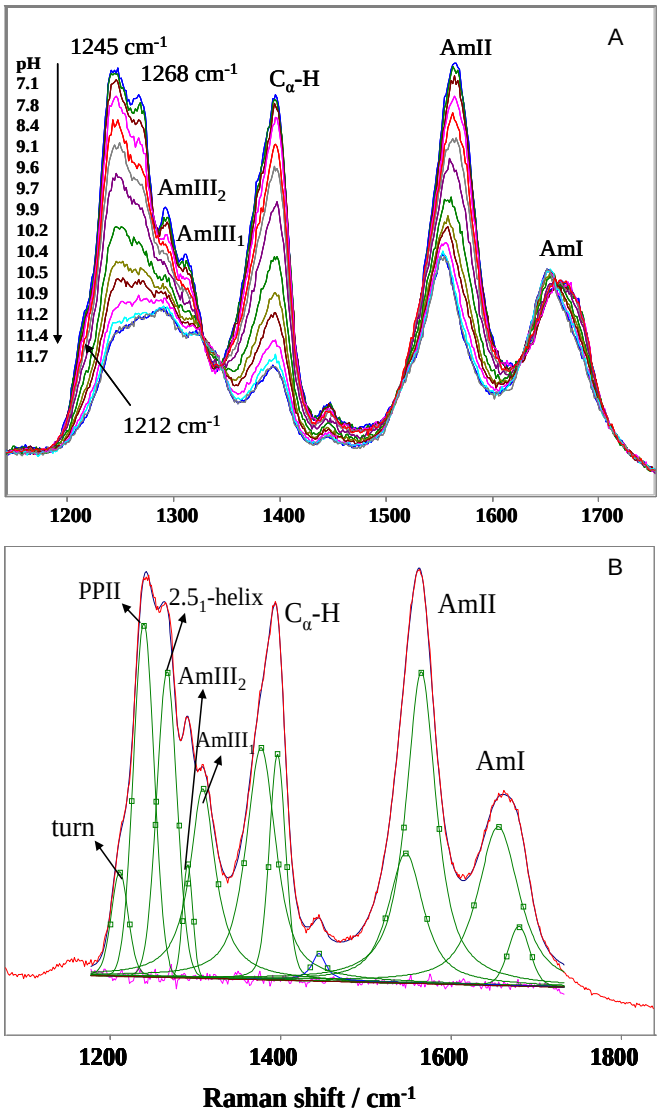

Figure 4.1. (A) pH dependence of the 204 nm UVRR spectra of PLL at 10 ºC. The spectra were normalized to the AmI band integrated intensities.[16] (B) Spectral deconvolution of the 10 ºC 204 nm UVRR PLL spectrum at pH 7.1. The excellence of the fit is evident from the flat residuals shown below.

The AmIII region is the most sensitive to peptide backbone conformational changes.[30] Fig. 4.1B shows the spectral deconvolution of the UVRR spectrum of PLL at pH 7.1. The $AmIII_1$ and $AmIII_2$ bands are located at ~1313 cm^{-1} and 1293 cm^{-1}. The $AmIII_3$ band region between 1190 cm^{-1} and 1285 cm^{-1} resolves into two peaks at ~1245 cm^{-1}, ~1268 cm^{-1} and a

shoulder at 1212 cm^{-1}. The $AmIII_3$ band frequencies can differentiate α-helix-like structures from extended structures, as well as differentiate between similar α-helix-like structures and extended structures, e.g., between the α-, 3_{10}-, π-helix structures and the PPII and 2.5_1-helix structures.[13]

We used the method of Mikhonin et al. to determine the peptide bone Ramachandran Ψ angles from the $AmIII_3$ band frequencies.[30] The ~1245 cm^{-1} and ~1268 cm^{-1} $AmIII_3$ bands derive from extended PPII and 2.5_1-helix conformations, respectively.[13,16] The shoulder probably derives from a turn structure, whose type we cannot as yet specify.

As the pH increases, the AmIII bandshape changes significantly. This occurs because the concentrations of the PPII and 2.5_1-helix conformations that have large Raman cross sections decrease, while the concentration of the α-helix-like conformation with a low Raman cross section increases. Little spectral changes occur between pH 11.4 and 11.7, indicating the lack of additional pH induced PLL conformational changes. There are two isosbestic points between the $AmIII_1$ and C_α-H b bands.

4.3.2 pD Dependence of PLL UVRR Spectra

Fig. 4.2A shows that the pH 7.1 UVRR spectrum of PLL changes dramatically in D_2O. The AmIII, AmII and C_α-H b bands disappear and are replaced with a very strong AmII' band at 1470 cm^{-1}, and a much weaker AmIII' band at 994 cm^{-1}. These spectral changes result from the deuteration of the peptide bond N-H. The AmII, AmIII and C_α-H b bands involve significant N-H bending; deuteration removes the N-H in plane bending component leaving an almost pure C-N s AmII' vibration and an AmIII' vibration which has a large N-D b component.

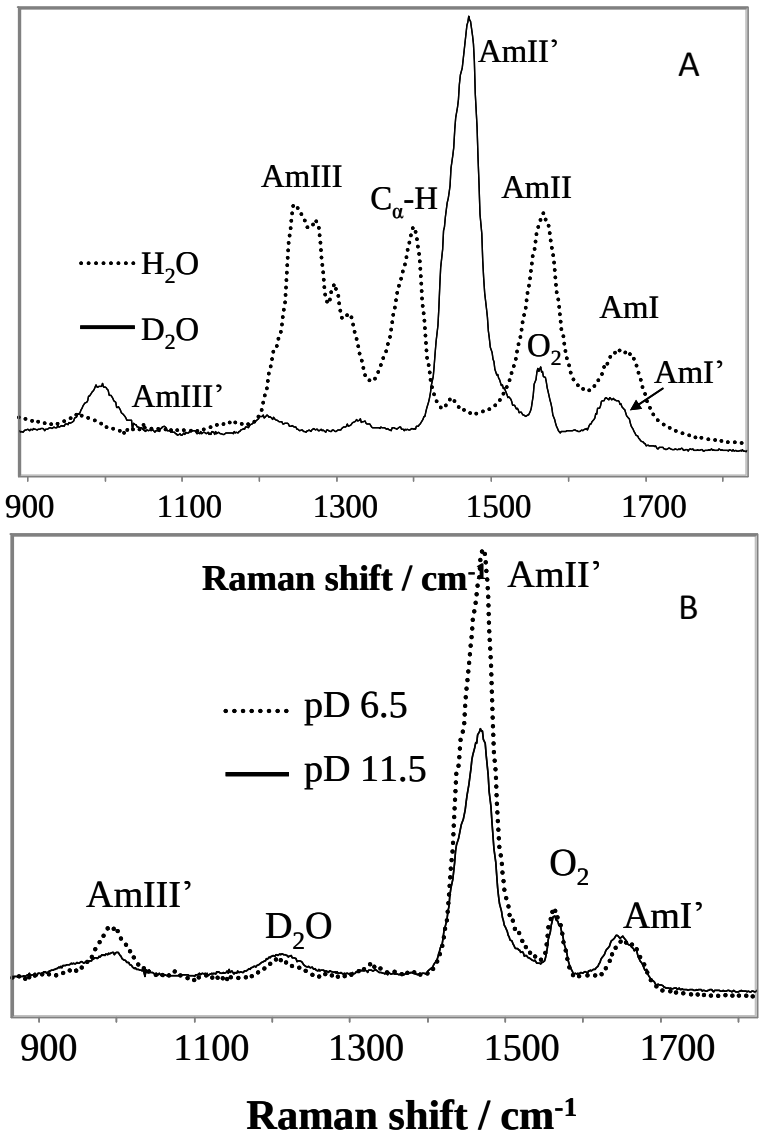

Figure 4.2. (A) 204 nm UVRR spectra of PLL at pH 7.1 in H_2O and D_2O. (B) 204 nm UVRR spectra of PLL in D_2O at pD 6.5 and 11.5. The spectra were normalized to the integrated AmI' band intensity.

Fig. 4.2B shows that as the pD increases from 6.5 to 11.5, the AmI' band downshifts ~ 8 cm^{-1}, which is less than the observed 14 cm^{-1} AmI band downshift. This indicates that part of the AmI band downshift results from non C=O stretching components.

The AmII' band of PLL shows only a ~2 cm^{-1} downshift, much less than the AmII band 12 cm^{-1} downshift. This smaller AmII' band shift indicates that the larger AmII band frequency shift mainly derives from changes in N-H hydrogen bonding. The loss of the N-H b component induced by deuteration results in a decreased AmII' band downshift. This is consistent with the theoretical study of N-methylacetamide by Myshakina et al,[28] who proposed that hydrogen bonding to the N-H causes an electron redistribution that dominates the AmII band upshift. The intensities of the AmII' and AmIII' bands decrease significantly as the pH increases due to the α-helix hypochromism.

4.3.3 Non-Two-State Conformational Transition of PLL

The pH induced PLL conformational transition previously studied by CD showed an isodichroic point.[31] All the CD spectra could be fit by two basis CD spectra measured at the extreme pH values. These results argued for a two-state conformational transition, from an unfolded conformation to an α-helix conformation.

We examined this pH dependence by modeling the observed Raman spectra by linearly adding the two PLL Raman spectra at the extreme pH values using a least-squares method.[32] The pH 9.1 to 10.5 spectra cannot be fit well by the use of the pH 11.7 and pH 7.1 (or at any pH < 8.4) basis spectra (Fig. 4.3A). The modeled results using the pH 7.1 basis spectrum always shows a stronger 2.5_1-helix band at ~ 1268 cm^{-1} than is observed between pH 9.1 and 10.5, indicating that the 2.5_1-helix content decreases relative to that of the PPII as the pH increases. However, the entire pH range between 9.1 to 11.7 can be fit well by using the pH 9.1 and pH 11.7 basis spectra, as shown in Fig. 4.3B. These results indicate that the pH induced conformational transitions between pH 7.1 to 11.7 involve more than two states,

whereas the conformational transition between pH 9.1 to 11.7 involves only two conformation or an equilibrium between two state of multiple conformations whose stoichiometry is constant within the sets.

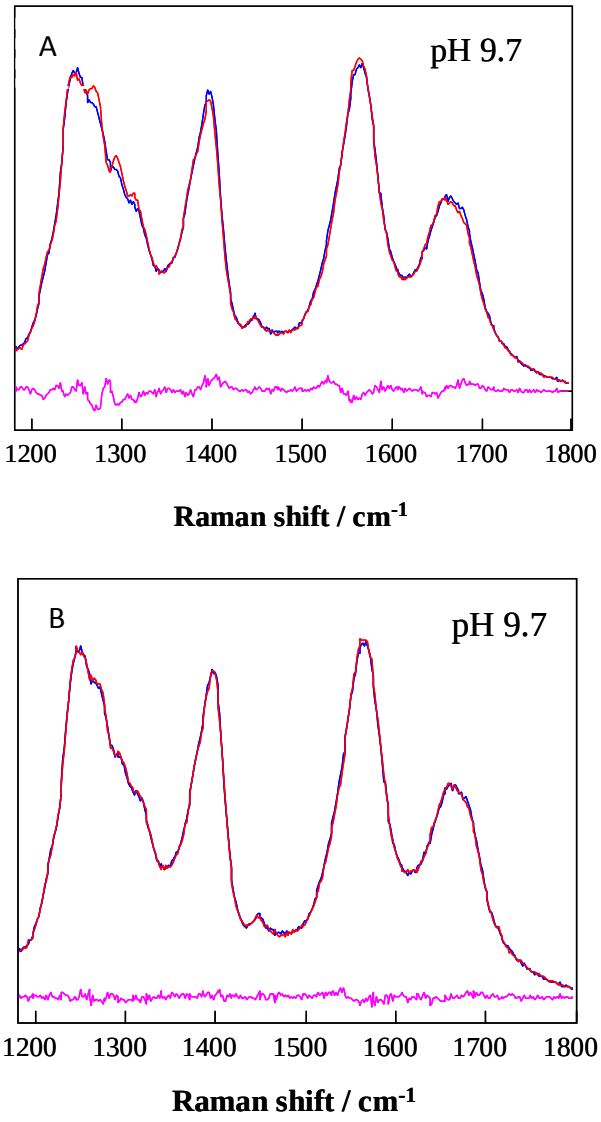

Figure 4.3. Comparison between observed (blue) and modeled (red) 204 nm UVRR of PLL at pH 9.7. (A) Using PLL UVRR pH 7.1 and 11.7 basis spectra. (B) Using PLL UVRR pH 9.1 and 11.7 basis spectra. The residuals show the differences between the modeled and observed spectra

Our UVRR two-state fitting of the PLL spectra demonstrates the high sensitivity of the $AmIII_3$ band region to peptide conformation, which allows us to discover that the relative fraction of 2.5_1-helix conformation to the PPII conformation decreases somewhat as the pH increases. These results also demonstrate that the appearance of isosbestic points is not always a reliable indicator of a two-state transition.

4.3.4 2D Correlation Spectroscopy

Generalized two-dimensional (2D) correlation spectroscopy was developed by Noda in 1986 to study the response of a system to an applied external perturbation.[23] The 2D correlation analysis produces two resulting plots where the correlation intensity is plotted as a function of two independent spectral axes: a 2D synchronous spectrum and a 2D asynchronous spectrum which represent the similarity and dissimilarity of spectral variations as a function of the perturbation. These spectra enhance spectral resolution. This increased resolution may enable discrimination of highly overlapped spectral peaks.

We performed a 2D correlation analysis on the pH dependent UVRR spectra of PLL. The 2D synchronous spectrum shown in Fig. 4.4 is characterized by strong and broad autopeaks and cross peaks for the AmIII band, the C_α-H b band and the AmII band. The color scale shows the correlated intensity variation spanned by the 2D contours. The large correlation intensities in the 2D synchronous plot indicate that the AmIII band, the C_α-H b band and the AmII band intensities of PLL vary with pH. The AmI band clearly resolves into two components at ~1650 cm^{-1} and 1665 cm^{-1}. The correlation magnitudes for the AmI band are smaller than for the other peaks, because its pH induced intensity variations are much smaller than for the other bands. Essentially, no additional information is gained from the

synchronous spectrum compared to the conventional analysis of UVRR spectra described above.

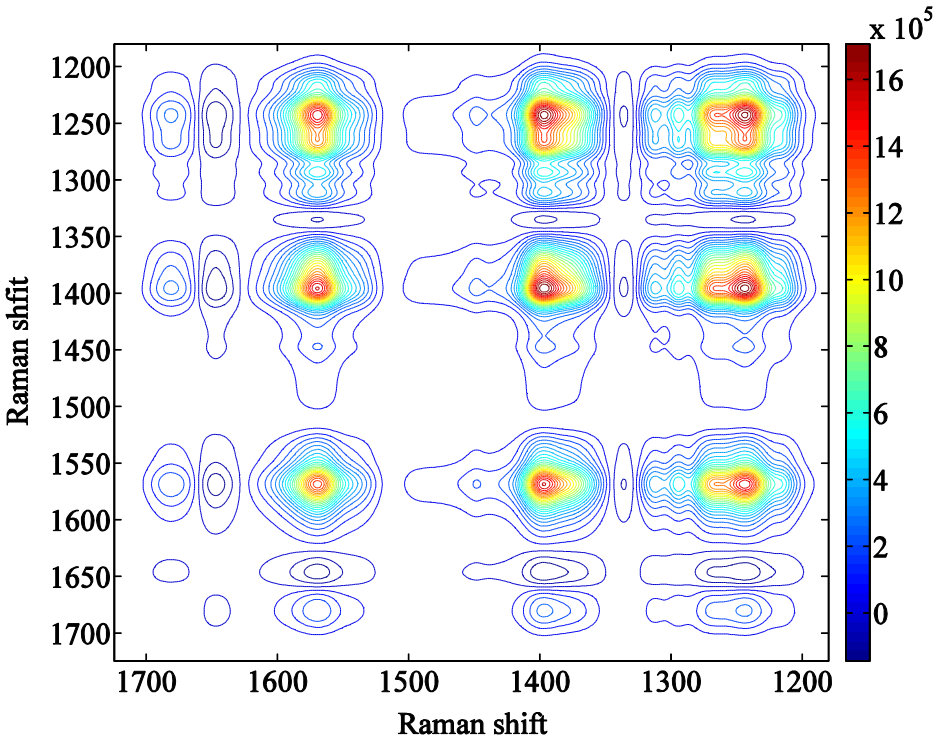

Figure 4.4. Synchronous pH dependence 2D UVRR spectrum of PLL.

Fig. 4.5 shows the 2D asynchronous correlation spectrum of PLL. The cross peaks occur when the intensities of two bands change at different rates or vary out of phase with respect to each other. No asynchronous cross peak occurs in the AmI region (1620-1700 cm^{-1}), which indicates that the correlation intensities in this region are weak. However, the cross peaks between the AmI and other bands resolve into two AmI band components that derive from extended and α-helix-like conformations.

The asynchronous contour in the AmII region (1500-1600 cm^{-1}) shows three out-of-phase cross peaks appearing at ~1530, 1553, 1573 cm^{-1} indicating that there are three components in the AmII region. As seen in Fig. 4.1B, the AmII band of PLL at pH 7.1 contains two subbands at ~ 1549 and 1567 cm^{-1}. The third AmII subband at ~1530 cm^{-1}, resolved in the 2D asynchronous spectrum, derives from the high pH α-helix-like PLL conformation. The C_α-H b band resolves into two components at ~1373 and 1396 cm^{-1}, respectively, whose origin is not yet clear.

The asynchronous contour in the AmIII region (1200-1320 cm^{-1}) is very complex. The complexity comes, in part, from the occurrence of the multiple conformations of PLL as the pH changes. It is very difficult to carry out band assignments based on just the AmIII cross peaks. Fortunately, the cross correlation regions of the AmIII band with the AmII and C_α-H b bands shed light on the analysis of the existence of multiple conformations.

As seen in Fig. 4.5, five AmIII subbands are observed at ~1316, 1294, 1270, 1241 and 1213 cm^{-1},that correlate to the C_α-H b 1396 cm^{-1} subband, and the AmII 1530 and 1573 cm^{-1} subbands; three AmIII peaks at ~1283, 1252, and 1225 cm^{-1} correlate with the 1373 cm^{-1} C_α-H b subband and the 1553 cm^{-1}AmII subbands. Therefore, 8 subbands resolve in the AmIII region at ~1316, 1294, 1283, 1270, 1252, 1241, 1225 and 1213 cm^{-1}.

The 1316 and 1394 cm^{-1} subbands come from the $AmIII_2$ and $AmIII_1$ bands, while the other six are associated with the the $AmIII_3$ bands that derive from PLL different secondary structures. The subbands at 1270 and 1241 cm^{-1} derive from the 2.5_1-helix and PPII conformation, respectively. The subband at 1213 cm^{-1} may result from the 1212 cm^{-1} shoulder observed in the Fig. 4.1 low pH PLL spectra. The other three subbands at 1283, 1252, and 1225 cm^{-1} result from high pH induced conformations. By using the method of

Mikhonin et al.,[30] we calculate that the subband at 1283 cm^{-1} most likely derives from π-helix/bulge conformations with an average Ramanchandran Ψ angle of -72º. The subband at 1252 cm^{-1} derives from an α-helix conformation with an average Ψ = -35 º, and the 1225 cm^{-1} subband may derive from a β-turn structure.

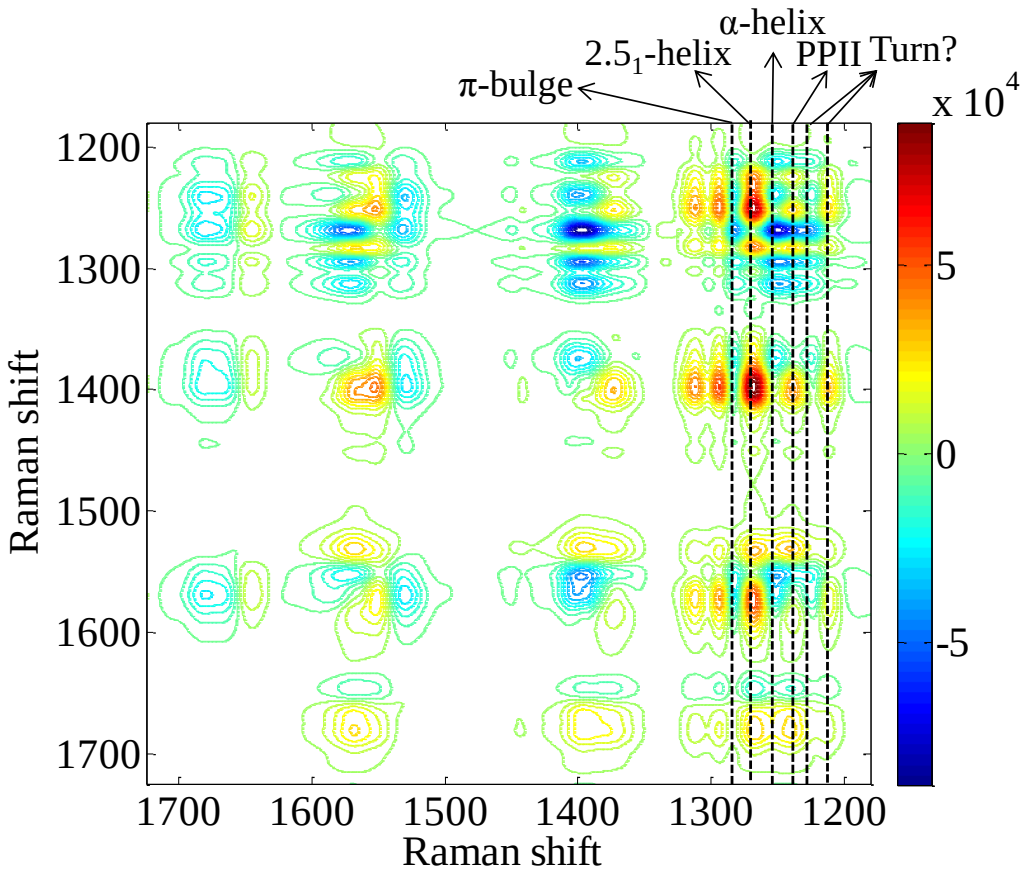

Figure 4.5. Asynchronous pH dependence 2D UVRR spectrum of PLL.

Thus, the asynchronous spectrum shows greatly enhanced spectral resolution. It reveals two components in the C_α-H b band and three components in the AmII band. The cross peaks in asynchronous spectrum, between the $AmIII_3$ band and the other bands, resolves into six $AmIII_3$ subbands which represents six PLL conformations including three new structures induced by increasing pH: the π-helix, α-helix and some turn structure.

A widely used application of 2D correlation spectroscopy is to determine the sequential order of reaction events based on the analysis of the sign of the peaks in the synchronous and asynchronous spectra. Generally, this analysis utilizes the sequential order rule proposed by Noda, which was originally developed from periodic perturbation 2D correlation spectroscopy.[33,34] The reliability of this sequential order rule for analyzing nonperiodic data set was recently questioned.[35,36] The work showed that synchronous and asynchronous spectra in the generalized 2D correlation spectroscopy of nonperiodic data cannot be simply interpreted identically to that of 2D correlation spectroscopy of periodic data. We conclude that we cannot determine the pH sequence of PLL conformational changes directly from these 2D synchronous and asynchronous results.

4.3.5 NaCl Concentration Dependence of PLL UVRR

It has long been known that salts can significantly impact peptide and protein conformations mainly due to Debye-Hückel screening, ion binding and ion modulation of water structure.[37,38] However, there appears to be little impact of high NaCl concentrations on the PLL conformation. For example, Fig. 4.6 shows the NaCl concentration dependence of the PLL UVRR spectra. Increasing the NaCl concentration causes the AmII, the C_α-H b and the AmIII band intensities to decrease slightly. The apparently large intensity increase of the AmI band actually results from a dramatic intensity increase of the overlapping water bending band due to the formation of a Cl^--water complex that has a strong charge transfer transition.[39]

The AmII band downshifts ~ 3 cm^{-1} in 2.5 M NaCl. Surprisingly, the presence of 2.5 M NaCl does not change the relative intensity of the PPII to 2.5_1-helix bands, even though

the 2.5_1-helix conformation is stabilized by electrostatic sidechain repulsions. Further, the expected large NaCl screening does not induce α-helix conformations. It should be noted that Xiong et al. also found that 2 M NaCl and KCl concentrations does not impact the PPII, 2.5_1-helix and α-helix conformational equilibrium of unfolded poly-L-glutamate (PLG).[40]

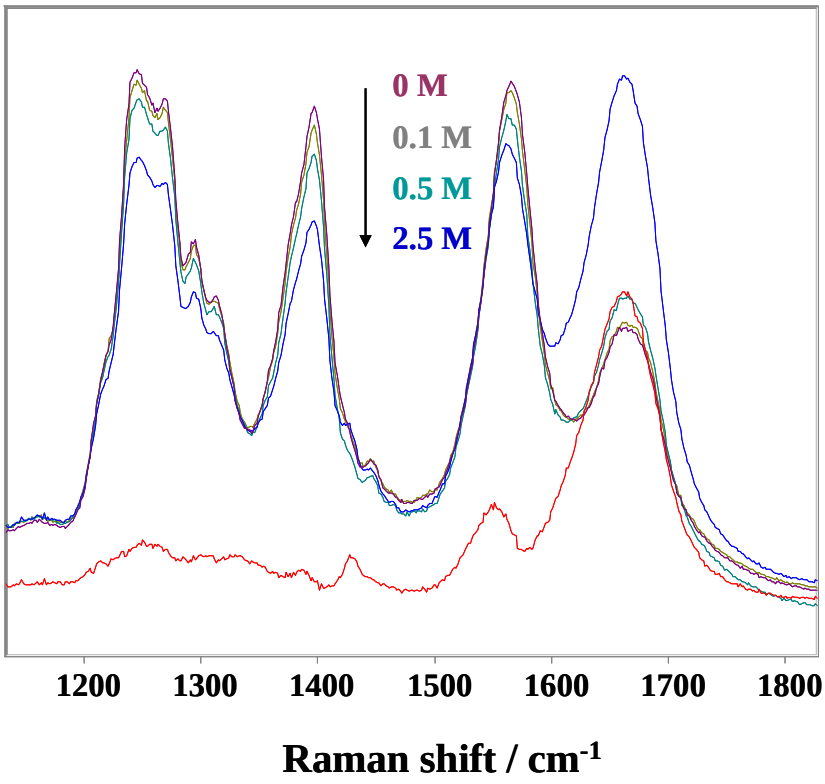

Figure 4.6. NaCl concentration dependence of the 204 nm PLL UVRR spectra at pH 6.1 (0.0, 0.1, 0.5 and 2.5 M NaCl). Also shown is a difference spectrum of PLL in the presence and absence of 2.5 M NaCl.

This surprising lack of NaCl impact on PLL and PLG conformations triggered us to reconfirm our assignment of 2.5_1-helix $AmIII_3$ band assignment. We examined the pH dependence of the 204 nm UVRR spectrum of K10 (Fig. 4.7A). At neutral or low pH K10 shows UVRR very similar to those of low pH PLL (Fig. 4.1). Fig. 4.7B displays three resolved $AmIII_3$ peaks at ~1216 cm^{-1}, 1247 cm^{-1} and 1268 cm^{-1}, that derive from the turn, the

PPII and the 2.5_1-helix conformations. The $AmIII_2$ band occurs at ~1293 cm^{-1}, the $AmIII_1$ band at ~1313 cm^{-1}, the C_α-H band at ~1395 cm^{-1}, the AmII band at ~1563 cm^{-1} and the AmI band at ~1665 cm^{-1}. As the pH increases to 11.52, the C_α-H band integrated intensity decreases by ~ 20%. The decrease in K10 intensity is reminiscent of the intensity loss of high pH PLL which results from a conversion to the α-helical conformation. The intensity loss for K10 is much less because the propensity for the α-helical conformation is decreased due to its short length.[41,42] K10 remains in ~80% extended conformation even at pH 11.9 where the sidechains are neutral. PLL is mainly α-helical structure at pH 11.7.

In K10, the 2.5_1-helix 1268 cm^{-1} $AmIII_3$ peak intensity significantly decreases relative to the PPII 1247 cm^{-1} peak as the pH increases, the 1247 cm^{-1} peak dominates at high pH. Thus, for K10, that 2.5_1-helix becomes destabilized as the sidechain electrostatic repulsion decrease. This result is consistent with our previous band assignment, that the 1268 cm^{-1} band derives from the 2.5_1-helix.

We can estimate the electrostatic repulsion decrease induced by salt screening by calculating the Debye lengths of the 0.1, 0.5, and 2.5 M NaCl solutions which are ~ 9.7, 4.3 and 1.9 Å. In PLL PPII and 2.5_1-helix conformation, the nearest neighbor sidechain spacings are 9.2 Å and 10.1 Å,[13] respectively. Thus, we expect strong charge screening at these salt concentrations. We can estimate the expected solution sidechain electrostatic repulsion decrease induced by NaCl screening from: $\psi(l) = \psi_0 e^{-l/\lambda_D}$, where $\psi(l)$ is the electrostatic potential at distance l and λ_D is the Debye length. We estimate that for the 2.5_1-helix conformation the electrostatic repulsion between the nearest neighboring side chains spaced by 10.1 Å would decrease by about 3-fold, 10-fold and nearly 200-fold for 0.1, 0.5 and 2.5 M NaCl, respectively.

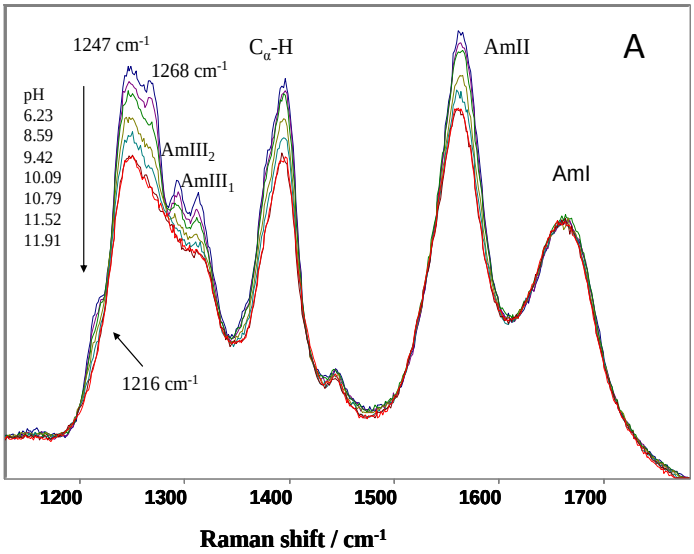

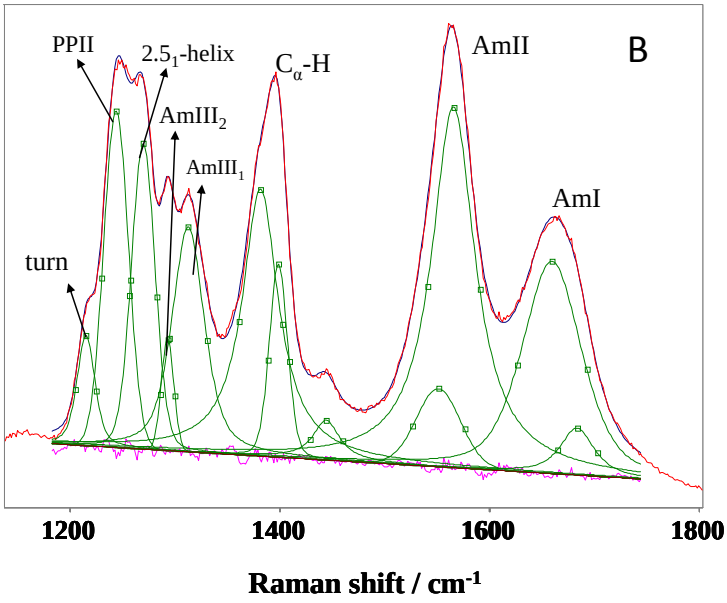

Figure 4.7. (A) pH dependence of 204 nm UVRR spectra of K10 at 10 ºC. The spectra were normalized to the AmI band integrated intensity. (B) Spectral deconvolution of 10 ºC 204 nm UVRR K10 spectrum at pH 6.2.

Based on our Raman data, PLL is ~ 50% α-helix-like structure at pH 10.1. The average pKa value of the PLL sidechains determined by Dos et al. using N^{15} NMR is 9.85±0.2.[43] Thus, the degree of ionization of PLL at pH 10.1 is about 36% giving an average sidechain charge of ~ 0.36 esu. Since the electrostatic interaction is proportional to the square of the charge, the resulted average sidechain electrostatic repulsion at pH 10.1 decreases about 8-fold compare to that at low pH if the salt distributed uniformly throughout the peptide solution.

The electrostatic repulsion decrease induced by 2.5 M NaCl screening should be much larger than that induced by pH 10.1 sidechain neutralization. It is surprising that 2.5 M NaCl does not induce α-helix-like structures. Even more surprising is that is does not decrease the 2.5_1-helix fraction compared to the PPII conformation. At pH 10.1 PLL adopts ~50% α-helix-like content, and the relative fraction of the 2.5_1-helix conformation to the PPII conformation decreases compared to that at low pH. This result indicates that NaCl does not penetrate the sidechain backbone region of PLL.

4.3.6 α-Helix-Like Conformations of PLL Induced by High pH and ClO_4^-

In contrast, $NaClO_4$ converts unfolded PPII and 2.5_1-helix charged sidechain PLL to the α-helix conformation.[16] Addition of 0.8 M $NaClO_4$ at pH 5.5 2.5 ºC converts PLL to an ~86% α-helix-like content. The lack of NaCl impact on PLL conformation indicates specific ClO_4^- interactions with the PLL sidechains probably involving ion pairing. The 'law of matching water affinities' predicts a high ion pairing propensity between the $-NH_3^+$ sidechains and ClO_4^- because both ions are weakly hydrated.

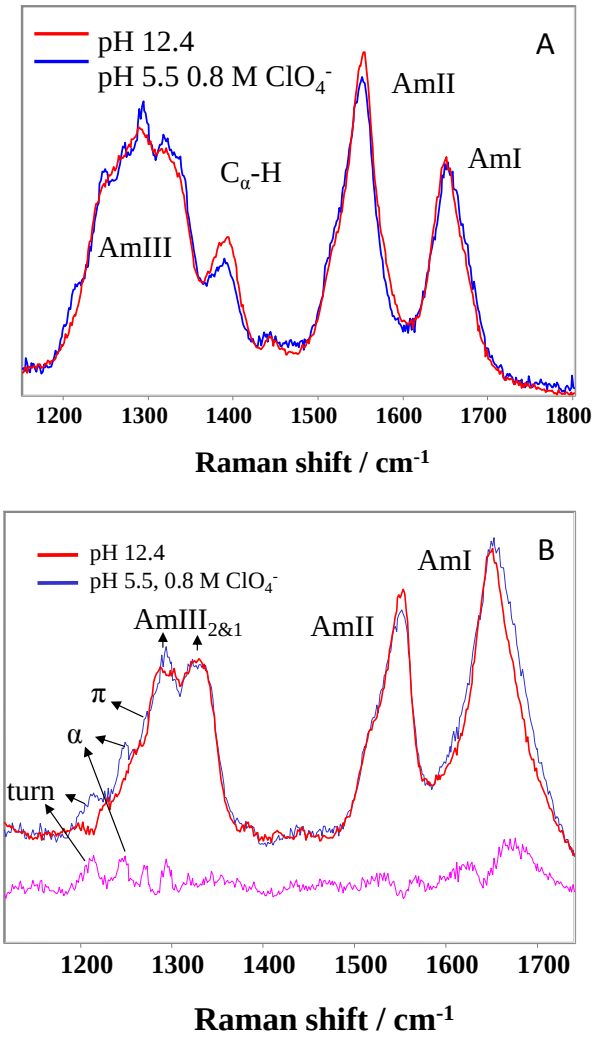

Figure 4.8. (A) Comparison of PLL 204 nm UVRR spectra at pH 12.4 in pure water to that at pH 5.5 in the presence of 0.8 M ClO_4^- at 2.5 ºC. The spectra are normalized to the AmI band integrated intensity. (B) Calculated pure α-helix-like PLL UVRR spectra at pH 12.4 in water and at pH 5.5 in the presence of 0.8 M ClO_4^-. Shown below is their difference spectrum. The α-helix-like UVRR spectra are calculated by subtracting the appropriate amount of the measured unfolded PLL conformation spectra (UVRR PLL spectra at pH 9.1) such that the C_α-H band disappears.

Fig. 4.8A compares the PLL UVRR spectra at pH 12.4 and 2.5 ºC in the absence of ClO_4^- to that at pH 5.5 in the presence of 0.8 M ClO_4^-. Since the C_α-H b band only occurs in the PPII, 2.5_1-helix, β-sheet-like conformations, we can use the C_α-H band intensity to

calculate the α-helix-like content. We assume that the unfolded PLL conformation UVRR spectra in ClO_4^- are identical to the low pH unfolded conformation UVRR in the absence of ClO_4^-. We also assume identical C_α-H b band cross sections of the PPII and 2.5_1-helix conformation. This calculation indicates that at pH 5.5 at 2.5 ºC PLL contains ~80% α-helix-like content at pH 12.4 , almost 6% less than that in 0.8 M ClO_4^-.

We previously found that $NaClO_4$ increases the α-helix concentration of an ala-based, 21-residue peptide. Molecular dynamic simulation carried by Asciutto et al[44] reveals that ClO_4^- binds strongly to the peptide backbone and excludes water from the peptide surface, thus, stabilizing the α-helix. We expect a similar phenomenon in PLL, where water would be excluded from PLL peptide surface, which results in a stabilization of the α-helix structure.

The spectra of the pure α-helix-like conformations of PLL can be obtained by subtracting appropriate amounts of the extended PLL conformation spectra from the observed UVRR. The calculated α-helix-like conformation spectra of PLL at pH 12.4 versus at pH 5.5 in 0.8 M ClO_4^- at 2.5 ºC are compared in Fig. 4.8B. At pH 12.4, the AmI band is slightly narrower, the intensity of the AmII band is slightly higher, the $AmIII_3$ peak intensities of turn and α-helix conformation are slightly weaker than that at pH 5.5 in 0.8 M ClO_4^-.

The narrower pH 12.4 PLL spectrum AmI bandwidth suggests that the α-helix-like conformation hydrogen bonding state is better defined than that of pH 5.5 0.8 M ClO_4^- conformation. The weaker turn and α-helix $AmIII_3$ bands at pH 12.4 compared to that in 0.8 M ClO_4^- indicates that the high pH solution has less turn content and longer α-helices than at 0.8 M ClO_4^-, since a longer α-helix will result in a smaller Raman cross section due to more

extensive hypochromism. This longer α-helix would result in more intramolecular hydrogen bonding which would narrow the AmI bandwidth.

We do not expect any intermolecular peptide interactions to influence the pH dependence of the PLL conformation at neutral and low pH values due to the repulsion between the charged peptide sidechains. This expectation is confirmed by our measured essentially identical pH 6.2, 204 nm UVRR spectra of PLL at 1 mg/ml and 2 mg/ml concentrations (not shown). In addition, a comparison of the recent Polavarapu et al.[45] 10 mg/ml pH 8.8 PLL CD spectrum to that of our Fig. 4.1 0.64 mg/ml, pH 5.5 CD spectrum[16] indicates very similar conformations. Although the pH values are not identical, Fig. 4.1 in the present manuscript shows very modest UVRR changes for increasing pH values up until pH 9.1. Finally, Meyers[31] measured 0.44 mg/ml, pH 8.35 CD PLL spectra that are very close to the 10 mg/ml Polavarapu et al.[45] CD spectra.

In contrast, Polavarapu et al.[45] demonstrated that at the higher pH value of 11.4 where the sidechains are mainly neutral PLL concentration increases from 1 mg/ml to 10 mg/ml induces conformational changes due to α-helix-like to a transition to β-sheet conformations. This conformational change is not observed by Meyer at pH 11.7 for the lower 0.44 mg/ml concentration. Further, we do not see any β-sheet contributions in the pH 11.5, 0.72 mg/ml PLL CD spectra (not shown). Thus, we conclude that there is a negligible interpeptide associations in the pH dependence of the 1 mg/ml PLL samples measured in the study here.

4.4 CONLUSIONS

The pH dependence of PLL UVRR spectra between pH 7.1 and 11.7 cannot be described by a two-state model. The $AmIII_3$ region fitting with pH 7.1 and 11.7 basis spectra reveals a small pH induced decrease in the relative fraction of the 2.5_1-helix conformation compared to the PPII conformation.

We performed a 2D general correlation analysis on the PLL pH dependence UVRR spectra. The asynchronous spectrum shows enhanced spectral resolution. The 2D asynchronous spectrum reveals multiple components in the C_α-H b band and the AmII band whose origins are unclear. The cross peaks in the 2D asynchronous spectrum between the AmIII band and the other bands reveals that increasing pH induces three new structures: π-helix, α-helix and some turn structure.

We examined the salt effect on PLL conformation, and found that 2.5 M NaCl does not change the equilibrium between the PPII and 2.5_1-helix conformation by screening sidechain electrostatic repulsion. The result indicates that NaCl does not penetrate the region between the sidechain and the peptide backbone.

4.5 APPENDIX: TWO-STATE FIT RESULTS

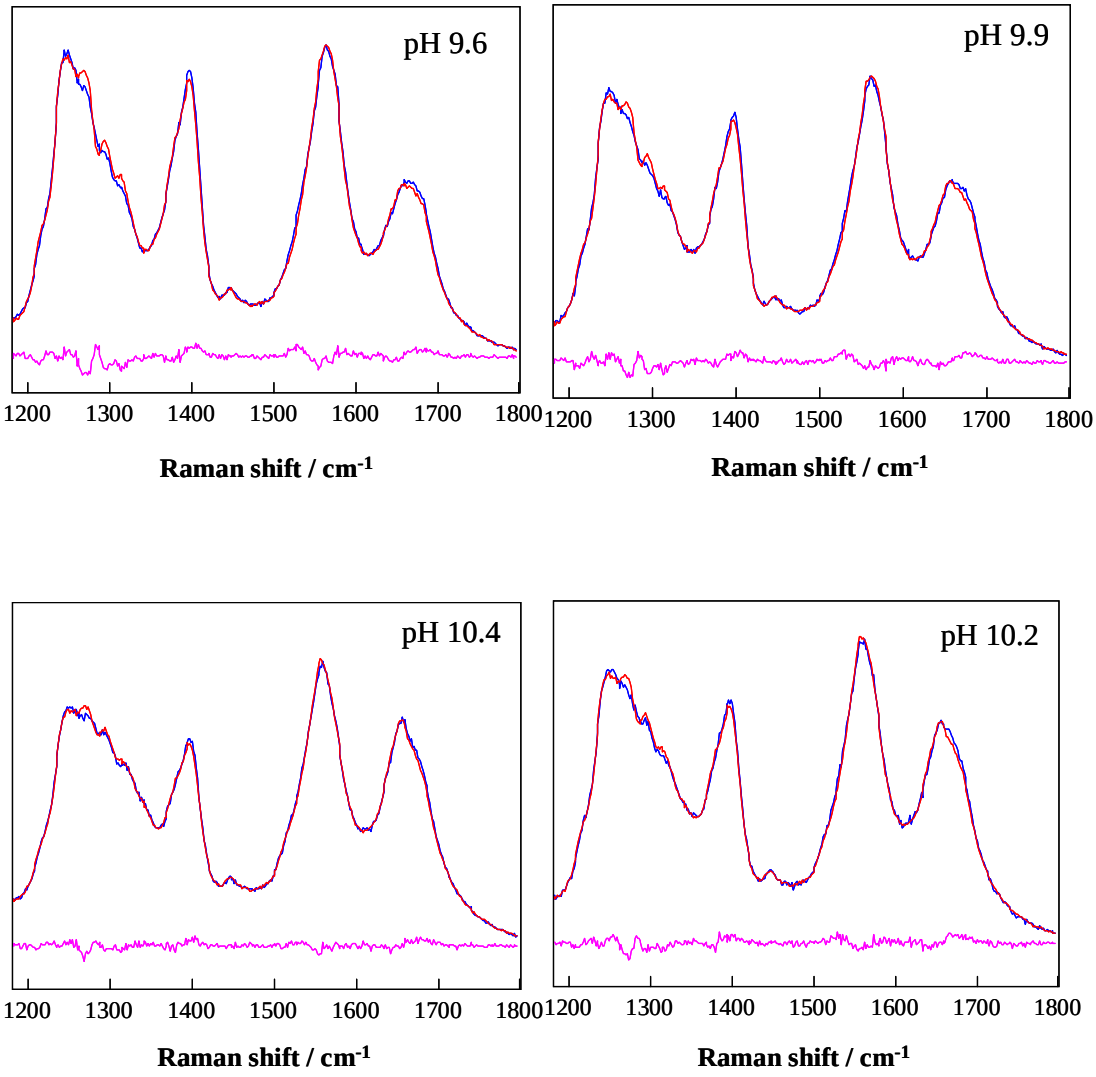

Figure 4.9. Comparison between observed (blue) and modeled (red) 204 nm UVRR of PLL at pH 9.6, 9.9,10.2 and 10.4 by using PLL UVRR pH 7.1 and 11.7 basis spectra. The residuals show the differences between the modeled and observed spectra.

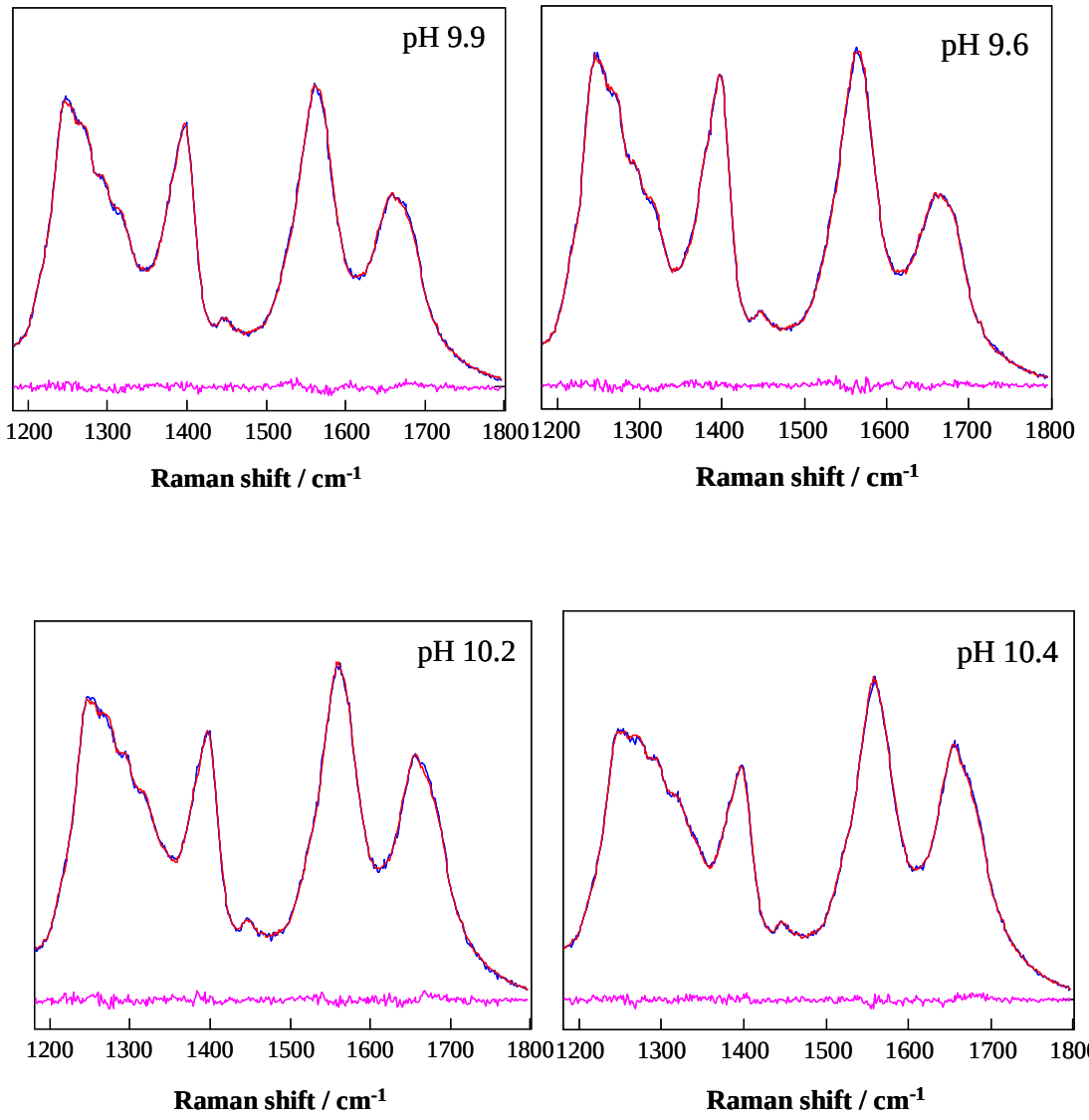

Figure 4.10. Comparison betweenobserved (blue) and modeled (red) 204 nm UVRR of PLL at pH 9.6, 9.9,10.2 and 10.4 by using PLL UVRR pH 9.1 and 11.7 basis spectra. The residuals show the differences between the modeled and observed spectra.

4.6 REFERENCES

(1) Baldwin, R. L.; Rose, G. D. *Trends Biochem. Sci.* **1999**, *24*, 26-33.

(2) Creighton, T. E., (Editor) *Protein Structure, Second Edition*; W.H. Freeman: New York, 1997.

(3) Dill, K. A. *Biochemistry* **1985**, *24*, 1501-9.

(4) Dill, K. A. *Protein Sci.* **1999**, *8*, 1166-1180.

(5) Dobson, C. M.; Sali, A.; Karplus, M. *Angew. Chem. Int. Ed.* **1998**, *37*, 868-893.

(6) Anfinsen, C. B. *Science* **1973**, *181*, 223-30.

(7) Anfinsen, C. B.; Scheraga, H. A. *Adv. Prot. Chem.* **1975**, *29*, 205-300.

(8) Haber, E.; Anfinsen, C. B. *J. Biol. Chem.* **1962**, *237*, 1839-44.

(9) Dill, K. A.; Ozkan, S. B.; Shell, M. S.; Weikl, T. R. *Annu. Rev. Biophys.* **2008**, *37*, 289-316.

(10) Suarez, M.; Jaramillo, A. *J. R. Soc. Interface* **2009**, *6*, S477-S491.

(11) Morra, G.; Meli, M.; Colombo, G. *Curr. Protein Pept. Sci.* **2008**, *9*, 181-196.

(12) Thirumalai, D.; O'Brien, E. P.; Morrison, G.; Hyeon, C. *Annu. Rev. Biophys.*, *39*, 159-183.

(13) Mikhonin, A. V.; Myshakina, N. S.; Bykov, S. V.; Asher, S. A. *J. Am. Chem. Soc.* **2005**, *127*, 7712-7720.

(14) Shi, Z.; Chen, K.; Liu, Z.; Kallenbach, N. R. *Chem. Rev.* **2006**, *106*, 1877-1897.

(15) Krimm, S.; Mark, J. E. *Proc. Nat. Acad. Sci. U. S. A.* **1968**, *60*, 1122-9.

(16) Ma, L.; Ahmed, Z.; Mikhonin, A. V.; Asher, S. A. *J. Phys. Chem. B* **2007**, *111*, 7675-7680.

(17) Davidson, B.; Fasman, G. D. *Biochemistry* **1967**, *6*, 1616-29.

(18) JiJi, R. D.; Balakrishnan, G.; Hu, Y.; Spiro, T. G. *Biochemistry* **2006**, *45*, 34-41.

(19) Bykov, S.; Lednev, I.; Ianoul, A.; Mikhonin, A.; Munro, C.; Asher, S. A. *Appl. Spectrosc.* **2005**, *59*, 1541-1552.

(20) Lednev, I. K.; Karnoup, A. S.; Sparrow, M. C.; Asher, S. A. *J. Am. Chem. Soc.* **1999**, *121*, 8074-8086.

(21) Chi, Z.; Chen, X. G.; Holtz, J. S. W.; Asher, S. A. *Biochemistry* **1998**, *37*, 2854-2864.

(22) Noda, I. *Appl. Spectrosc.* **2000**, *54*, 994-999.

(23) Noda, I.; Ozaki, Y. *Two dimensional correlation spectroscopy-applicationa in vibrational and optical spectroscopy*; John Wiley & Sons, Ltd, 2004.

(24) Imahori, K.; Tanaka, J. *J. Mol. Biol.* **1959**, *1*, 359-64.

(25) Tinoco, I. J.; Halpern, A.; Simpson, W. T. *Polyamino Acids, Polypeptides, and Proteins*; University of Wisconsin Press: Madison, 1962.

(26) Jordan, T.; Spiro, T. G. *J. Raman Spectrosc.* **1995**, *26*, 867-76.

(27) Mikhonin, A. V.; Ahmed, Z.; Ianoul, A.; Asher, S. A. *J. Phys. Chem. B* **2004**, *108*, 19020-19028.

(28) Myshakina, N. S.; Ahmed, Z.; Asher, S. A. *J. Phys. Chem. B* **2008**, *112*, 11873-11877.

(29) Triggs, N. E.; Valentini, J. J. *J. Phys. Chem.* **1992**, *96*, 6922-31.

(30) Mikhonin, A. V.; Bykov, S. V.; Myshakina, N. S.; Asher, S. A. *J. Phys. Chem. B* **2006**, *110*, 1928-1943.

(31) Myer, Y. P. *Macromolecules* **1969**, *2*, 624-628.

(32) Chi, Z.; Chen, X. G.; Holtz, J. S. W.; Asher, S. A. *Biochemistry* **1998**, *37*, 2854-2865.

(33) Noda, I. *J. Am. Chem. Soc.* **1989**, *111*, 8116-18.

(34) Noda, I. *Appl. Spectrosc.* **1993**, *47*, 1329-36.

(35) Huang, H. *Anal. Chem.* **2007**, *79*, 8281-92.

(36) Jia, Q.; Wang, N.-N.; Yu, Z.-W. *Appl. Spectrosc.* **2009**, *63*, 344-353.

(37) Goto, Y.; Takahashi, N.; Fink, A. L. *Biochemistry* **1990**, *29*, 3480-8.

(38) Lund, M.; Vacha, R.; Jungwirth, P. *Langmuir* **2008**, *24*, 3387-3391.

(39) Xiong, K.; Asher, S. A. *J. Phys. Chem. A* **2010**, *in press*.

(40) Xiong, K.; Ma, L.; Asher, S. A. *Accepted by Biophys. Chem.*

(41) Lifson, S.; Roig, A. *J. Chem. Phys.* **1961**, *34*, 1963-74.

(42) Zimm, B. H.; Bragg, J. K. *J. Chem. Phys.* **1959**, *31*, 526-35.

(43) Dos, A.; Schimming, V.; Tosoni, S.; Limbach, H.-H. *J. Phys. Chem. B* **2008**, *112*, 15604-15615.

(44) Asciutto, E. K.; General, I. J.; Xiong, K.; Asher, S. A.; Madura, J. D. *Biophys. J.* **2010**, *98*, 186-196.

(45) Shanmugam, G.; Polavarapu, P. L. *J. Mol. Struct.* **2008**, *890*, 144-149.

CHAPTER 5

UV resonance Raman studies of the $NaClO_4$ dependence of poly-L-lysine conformation and hydrogen exchange kinetics

This Chapter was accepted by *Journal of Physical Chemistry B*. The co-authors are Lu Ma, Zhenmin Hong, Bhavya Sharma, Sanford Asher.

5.0 UV RESONANCE RAMAN STUDIES OF THE PERCHLORATE DEPENDENCE OF THE POLY-L-LYSINE CONFORMATION AND HYDROGEN EXCHANGE KINETICS

We used 204 nm excitation UV Resonance Raman (UVRR) spectroscopy to examine the effects of $NaClO_4$ on the conformation of poly–L–lysine (PLL). The presence of $NaClO_4$ induces the formation of α–helix, π–helix/bulge and turn conformations. The dependence of the $AmIII_3$ frequency on the peptide Ψ Ramachandran angle allows us to experimentally determine the conformational population distributions and the energy landscape of PLL along the Ramachandran Ψ angle. We also used UVRR to measure the $NaClO_4$ concentration dependence of PLL amide hydrogen exchange kinetics. Exchange rates were determined by fitting the D_2O exchanging PLL UVRR AmII' band time evolution. Hydrogen exchange is slowed at high $NaClO_4$ concentrations. The PLL AmII' band exchange kinetics at 0.0, 0.2 and 0.35 M $NaClO_4$ can be fit by single exponentials, but the AmII' band kinetics of PLL at 0.8 M $NaClO_4$ requires a double exponential fit. The exchange rates for the extended conformations were monitored by measuring the C_α–H band kinetics. These kinetics are identical to those of the AmII' band until 0.8 M $NaClO_4$ whereupon the extended conformation exchange becomes clearly faster than that of the α–helix–like conformations. Our results indicate that ClO_4^- binds to the PLL backbone to protect it from OH^- exchange catalysis. In addition, ClO_4^- binding also slows the conformational exchange between the

extended and α–helix–like conformations, probably by increasing the activation barriers for conformational interchanges.

5.1 INTRODUCTION

An understanding of the mechanism(s) of protein folding remains an important unsolved problem in structural biology.[1-6] The major underlying assumption is that the protein native structure is the most thermodynamically stable structure.[7-9] Thus, the protein primary sequence is expected to contain all of the information necessary to both specify the protein native structure and its folding mechanism(s). The well-known Levinthal paradox implies that there exist specific folding intermediates or pathways through which the protein quickly evolves into its final functional structure.[10]

The mechanisms of protein folding have been probed experimentally by techniques such as CD, NMR, IR, Raman, fluorescence and a variety of time resolved spectroscopies, mutational studies and hydrogen exchange methods.[11-16] Most recently, single molecule methods have probed the distributions of the unfolded and folded states by following the folding reaction of individual molecules.[17-20] Single molecule methods, such as optical tweezers and AFM, have been used to elucidate protein folding intermediates and the energy landscapes by using mechanical force as a denaturant.[17,21] Computational modeling has also made significant contributions to the understanding of protein folding.[22-24]

In the work here, we use UV resonance Raman (UVRR) spectroscopy to study the conformational distributions of poly-L-lysine (PLL) in the presence of different $NaClO_4$ concentrations. ClO_4^- induces an α-helix conformation at neutral and low pH values, where

the lysine side chains are positively charged.[25,26] Ma et al. recently observed that PLL adopts multiple α-helix-like conformations in the presence of ClO_4^-, including pure α-helix and π-bulge/helix conformations.[27]

We also determined the dependence of the PLL conformational population distributions and the energy landscapes on $NaClO_4$ concentration. We measured the hydrogen exchange behavior of the PLL peptide bond NH at pH 2.8 at different $NaClO_4$ concentrations. The results show that the exchange rates are $NaClO_4$ concentration dependent and that the hydrogen exchange behavior indicates that the PLL conformations are in rapid equilibrium until the highest $NaClO_4$ concentrations where two exchange rates are observed.

5.2 EXPERIMENTAL

5.2.1 Materials

Poly-L-lysine HCl (MW_{vis} = 20900, DP_{vis}= 127, MW_{MALLS} = 11400, DP_{MALLS} = 69, where DP_{vis} and DP_{MALLS} refer to the degree of polymerization measured by viscosity and multi-angle laser light scattering, respectively) was obtained from Sigma Co. and used without further purification. $NaClO_4$ was purchased from Sigma Co., and was used without further purification. D_2O (99.9 atom %D) was purchased from Cambridge Isotope Laboratories, Inc. Small aliquots of HCl and DCl solutions were used to adjust the solution pH values. DCl (99 + atom %D) was acquired from Aldrich. The UVRR spectra of PLL at different $NaClO_4$ concentrations were measured at 0.85 mg/ml peptide concentrations at pH 3, and the spectra were normalized to the Raman intensity of the symmetric stretching band of ClO_4^-.

5.2.2 UVRR Instrument

We used a Coherent Infinity Nd: YAG laser (Coherent, Inc.) to produce 355 nm light pulses (3rd harmonic) at a 100 Hz repetition rate with a pulse width of 3 ns. This beam was Raman shifted to 204 nm (5th anti-Stokes) using a 1-m tube filled with hydrogen (60 psi), giving 2 mW average power.[28,29] A Pellin Broca prism was used to select the 204 nm excitation. The sample was circulated in a free surface, temperature controlled stream to avoid heating or accumulation of photochemical degradation products formed by the high peak power laser pulses. The Raman scattered light was imaged into a subtractive double spectrometer.[28] The dispersed UV light was detected by the liquid nitrogen cooled, Unichrome coated, back-thinned CCD with a >30% quantum efficiency in the deep UV (Princeton Instruments Spec-10:400B). More details on the UVRR apparatus are given by Bykov et al.[28]

5.2.3 CD Measurements

Circular dichroism (CD) spectra were measured by using a Jasco J-710 spectropolarimeter. The spectra were measured by using a temperature controlled 0.2 mm path length cell with 0.87 mg/ml PLL concentrations.

5.2.4 Hydrogen Exchange Experiment

1 ml pD 2.9 D_2O solutions containing 8.5 mg PLL and 0, 0.2, 0.35 or 0.8 M $NaClO_4$ concentrations were prepared and mixed rapidly with a 9 ml H_2O solution at pH 2.8 with the

same $NaClO_4$ concentrations. The dead times for all mixing experiment were 25 to 60 s. The time dependent UVRR spectra of the solutions at 0.85 mg/ml PLL concentration containing 0, 0.2, 0.35 or 0.8 M $NaClO_4$ were collected at 5 s intervals with 5 s data accumulation times. For samples containing $NaClO_4$, all Raman spectra are normalized to the intensity of the 932 cm^{-1} ClO_4^- Raman band. In the absence of $NaClO_4$ the AmI (AmI') band intensity was used as the internal intensity standard.

5.3 RESULTS AND DISCUSSION

5.3.1 $NaClO_4$ Dependence of 204 nm UVRR Spectra of PLL

Previous studies show that $NaClO_4$ converts unfolded PLL with charged side chains to α–helix–like conformations.[27] For example, 0.8 M $NaClO_4$ at pH 5.5 at 2.5 ºC converts normally extended PLL conformations to an ~86% α–helix–like content.[30] Fig. 5.1A shows 204 nm UVRR spectra of PLL at different $NaClO_4$ concentrations at pH 3 and 20 °C. In the absence of $NaClO_4$, as observed previously, PLL occurs in an equilibrium between extended polyproline II (PPII) and 2.5_1–helix conformations at low pH.[27,31] These conformations give rise to $AmIII_3$ bands at ~1245 cm^{-1} and ~1268 cm^{-1}, respectively as shown in Fig. 5.1B. As the $NaClO_4$ concentration increases the intensities of the AmIII bands between 1190 and 1300 cm^{-1}, the ~1400 cm^{-1} C_α–H b band, and the ~1567 cm^{-1} AmII band decrease. In addition, the AmI and AmII band frequencies downshift; 0.8 M $NaClO_4$ causes the AmI and AmII bands to downshift by 12 cm^{-1}, and the AmI bandshape narrows and becomes more

symmetric. These spectral changes indicate the formation of α–helical–like conformations as confirmed by the CD measurement in Fig. 5.2.

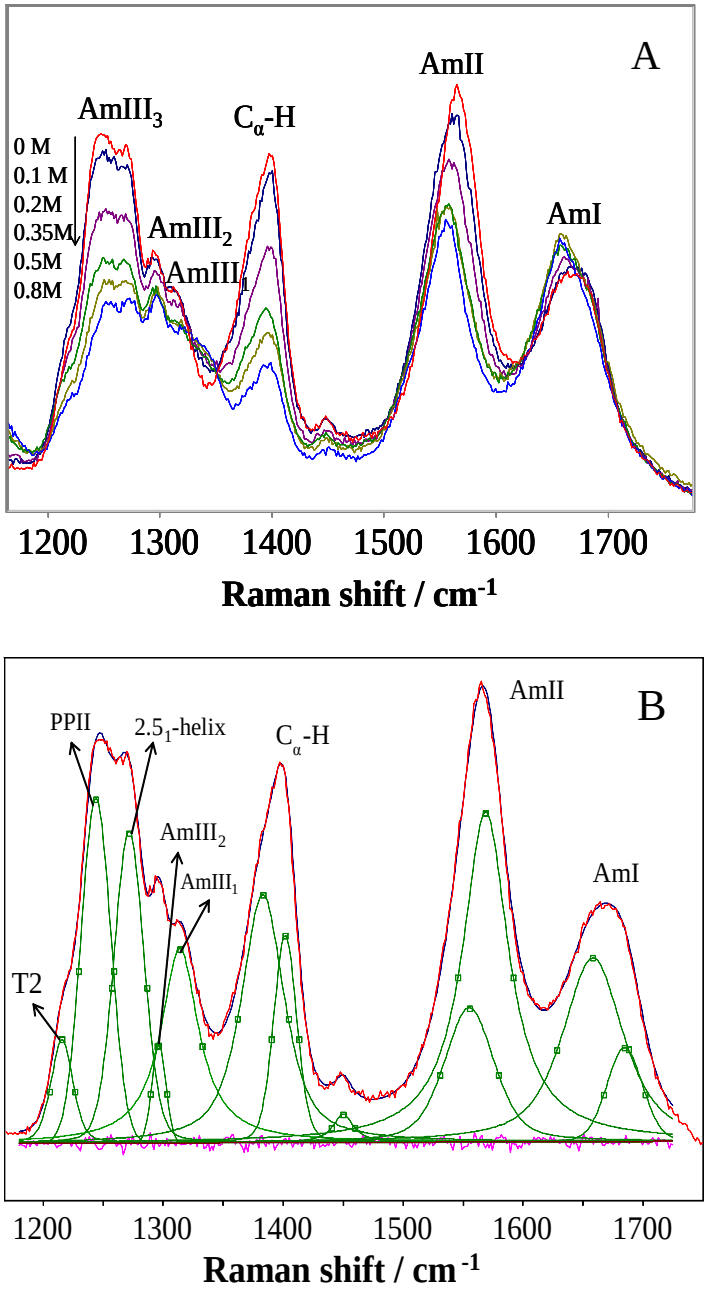

Figure 5.1. (A) 204 nm UVRR spectra of PLL at pH 3 and 20 °C at 0, 0.1, 0.2, 0.35, 0.5 and 0.8 M $NaClO_4$ concentrations. (B) Deconvolution of the 20 ºC 204 nm UVRR PLL spectrum in the absence of $NaClO_4$ at pH 3.

We previously believed that $NaClO_4$ converts charged PLL to a highly α–helical conformation by forming ion–pairs between ClO_4^- and the PLL $–NH_3^+$ side chains to neutralize the repulsions that destabilize α–helical conformations.[27,32-34] A simple Debye–Hückel screening mechanism was excluded because high NaCl concentrations negligibly impact the PLL conformation.[26,30] Ion–pair formation should dramatically decrease side chain electrostatic repulsions. This should decrease the 2.5_1–helix conformation content that is stabilized by side chain electrostatic repulsions.

Indeed our previous study of K10 (Ac–lys10–NH_2) demonstrated that the neutralization of the charged lysine side chains at increased pH significantly decreased the relative fraction of 2.5_1–helix compared to that of the PPII conformation.[30] However, surprisingly, the UVRR spectra of PLL showed that $NaClO_4$ does not decrease the relative fraction of 2.5_1–helix significantly compared to that of the PPII conformation. We frankly do not understand this result.

The C_α–H b bands that are resonantly enhanced in the extended PPII, β–sheet, and β–strand–like conformations, are not enhanced in the α–helix–like conformations. As a result, in Fig. 5.1A, the C_α–H b band shows a large intensity decrease relative to that of the AmII and AmIII bands. Using the C_α–H b band intensity to indicate the extended PLL concentration content, we subtract the appropriate amount of the extended PLL spectrum from the measured spectra, leaving the UVRR of the $NaClO_4$–induced α–helix conformation. This subtraction assumes that the extended conformation possesses an invariant UVRR spectrum as the $NaClO_4$ concentration increases; this assumption is supported by the fact that the UVRR difference spectra between successive additions of $NaClO_4$ are very similar, and

that the system appears 2–state from the Fig. 5.1 and Fig. 5.2 isosbestic points in the UVRR and the CD.

Fig. 5.3 shows the estimated α–helix–like fraction of PLL at different $NaClO_4$ concentrations obtained from the UVRR. The α–helix–like content fraction of PLL at different $NaClO_4$ concentrations, f_H, can also be calculated from the Fig. 5.2 CD spectra by utilizing the equation [29,35]:

$$f_H = \frac{\theta_{222} - \theta_r}{\theta_H - \theta_r} \quad (5.1)$$

θ_{222} is the molar ellipticity at 222 nm, which is assumed to be proportional to the helix content, θ_r and θ_H are the molar ellipticities of the extended and α–helix–like conformations. Here, θ_r was experimentally measured as 2854 deg cm^2 $dmol^{-1}$, and θ_H = 32200 deg cm^2 $dmol^{-1}$ is the mean residue ellipticity as averaged over several polypeptides.[36]

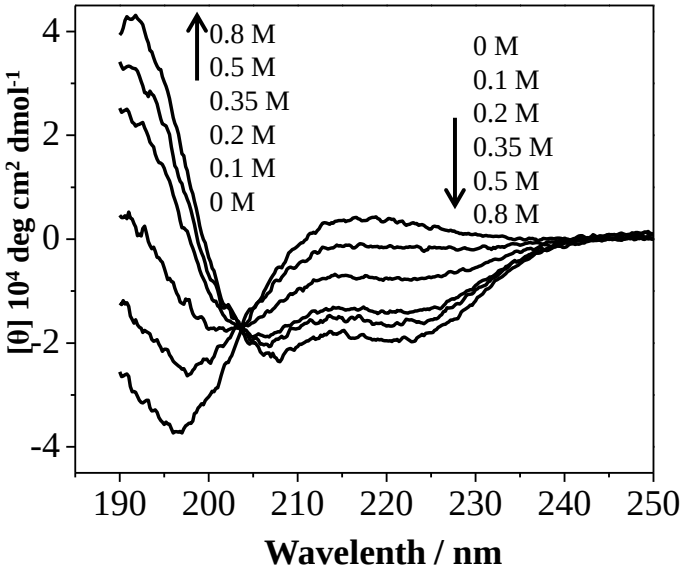

Figure 5.2. $NaClO_4$ concentration dependence of 0.87 mg/ml PLL CD spectra at pH 3 and 20 ºC.

The α–helix–like fraction obtained from CD is smaller than that obtained from UVRR (Fig. 5.3). The 222 nm CD ellipticity results from interpeptide bond exciton coupling of the α–helical conformation electronic dipole transition moments. The ellipticity per residue decreases for short α–helices.[29,35,37]

In contrast, the Raman intensity is the sum of the intensities from each peptide bond. We calculated the α–helix fraction by assuming that there only exist two conformations, either an extended conformation or an α–helix–like conformation. We used the C_α–H b band intensity to calculate the PLL extended conformational fraction. We do not expect phenomena such as hypochromism to alter the extended conformation peptide bond Raman cross sections.

We calculated the UVRR α–helix–like conformation fraction from $f_H = 1–f_{extended}$. The α–helix–like conformational fractions calculated from the UVRR include α–helix–like turns that do not give significant contributions to the 222 nm ellipticity. Thus, the Raman indicates a higher α–helix–like fraction than CD (Fig. 5.3).

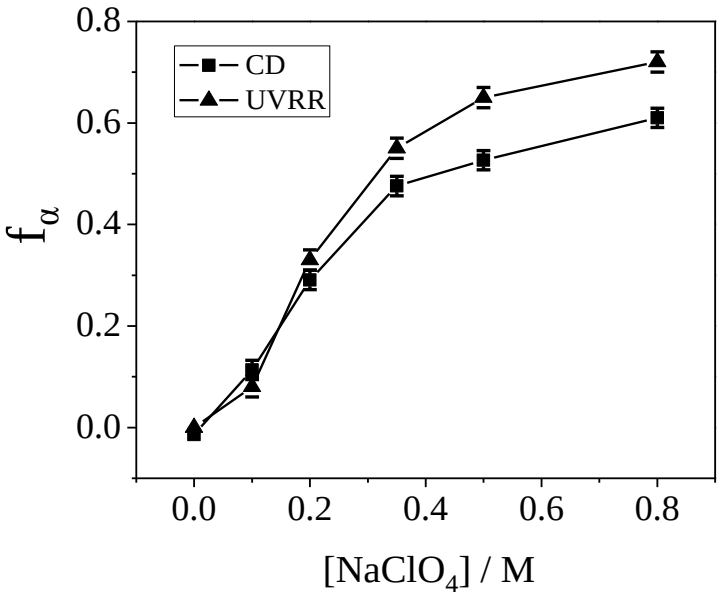

Figure 5.3. Comparison of PLL α–helix–like conformation fraction calculated from CD and UVRR at different $NaClO_4$ concentrations at pH 3 and 20 °C.

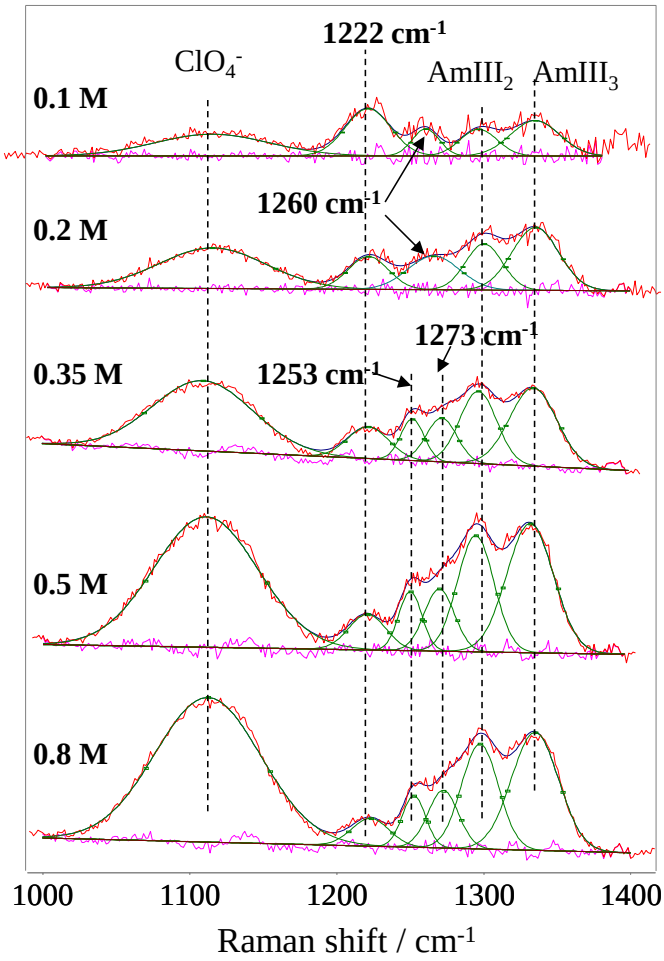

Figure 5.4. $NaClO_4$ concentration dependence of the AmIII region of the 204 nm UVRR spectra of the calculated α–helix–like PLL conformations at pH 3 and 20 °C. See text for details.

Fig. 5.4 shows the calculated α–helix–like PLL AmIII region UVRR spectra. The AmIII region of the α–helix–like PLL spectra is well modeled by Gaussian bands. The 1110 cm^{-1} band derives from the ClO_4^- asymmetric stretching band, while the $AmIII_1$ and $AmIII_2$ bands are located at 1332 cm^{-1} and 1294 cm^{-1}. As shown in Fig. 5.4 the $AmIII_3$ band spectral region depends on the $NaClO_4$ concentration. At 0.1 and 0.2 M $NaClO_4$ concentrations, the $AmIII_3$ region resolves into two bands at 1222 cm^{-1} and 1260 cm^{-1}. In contrast, at 0.35, 0.5

and 0.8 M $NaClO_4$, the $AmIII_3$ region resolves into three bands at 1222 cm^{-1}, 1253 cm^{-1} and 1273 cm^{-1}.

5.3.2 $NaClO_4$ Dependence of PLL Ψ Angle Distribution

Using the method developed by Mikhonin et al,[38] we can calculate the Ramachandran Ψ angle distribution from the $AmIII_3$ band frequency distribution if we know the peptide bond hydrogen bonding states.[38-40] Fig. 5.5 shows the $NaClO_4$ concentration dependence of the Ψ angle distributions of PLL calculated from the $AmIII_3$ bands deriving from the calculated α–helix–like spectra of Fig. 5.4, and from the pure extended conformations of PLL in the absence of $NaClO_4$ of Fig. 5.1B.

Assuming α–helix–like intramolecular peptide bond hydrogen bonding, the 1273 cm^{-1}, 1260 cm^{-1} and 1253 cm^{-1} $AmIII_3$ bands are calculated to derive from conformations with average Ramanchandran Ψ angles of –60°, –43°, –36°.[38]

Thus, the 1273 cm^{-1} and 1253 cm^{-1} $AmIII_3$ bands derive from π–bulge and pure α–helix conformations, respectively. The 1260 cm^{-1} $AmIII_3$ band occurs at a frequency between that of the α–helix and π–bulge/helix conformation. It could derive from distorted α–helix or π–helix conformations.

The 1222 cm^{-1} $AmIII_3$ band could result from Ψ angles, of either 4° or 124°. Because the 1222 cm^{-1} $AmIII_3$ band does not also show the significant intensity in the C_α–H b band region that would be expected for this partially extended structure, we exclude the 124° Ψ angle possibility, and assume that the conformation is close to that of an α–helix. This conformation could derive from type I or I' and type II or II' turns from their i+2 residues

based on this Ψ value.[38] For brevity we label this turn conformation T1. We assume here equal Raman cross sections for α–helix, π–helix and T1 structures.

The extended conformation PLL spectra, measured in the absence of $NaClO_4$, shown in Fig. 5.1B shows three $AmIII_3$ bands. Two were assigned to the PPII and 2.5_1–helix conformations, as discussed above. The third $AmIII_3$ band appears as a shoulder at 1214 cm^{-1}. This band which we label T2 could also result from turn conformations, with Ψ angles of either 14° or 114°. However, it is unclear whether this turn conformation shows significant C_α–H b band intensity because of the overwhelming contributions of the PPII and 2.5_1–helix conformations.

Ψ = 14° could derive from a somewhat distorted type I, II, or II', i+2 residues, or type I' or III', i+1 and i+2 residues. Ψ = 114° could derive from a somewhat distorted type II, i+1 residues or a type VIII, i+2 residue.[38] Fig. 5.5 shows the Ψ distribution assuming that the T2 conformation possesses Ψ = 114° and that this conformation shows Raman bands with the same cross sections as the PPII and 2.5_1–helix extended conformations.

At 0.1 M $NaClO_4$ the Ψ angle distribution show only the distorted α–helix or π–bulge conformations and the T1 and T2 turn structures and the PPII and 2.5_1–helix structures. π–bulge structures are induced by increasing $NaClO_4$ concentration. Further, as the $NaClO_4$ concentration increases, the α–helix–like content increases, decreasing the extended conformation content. The relative concentrations of α–helix and π–bulge concentrations increase compared to that of the T1 turn structure.

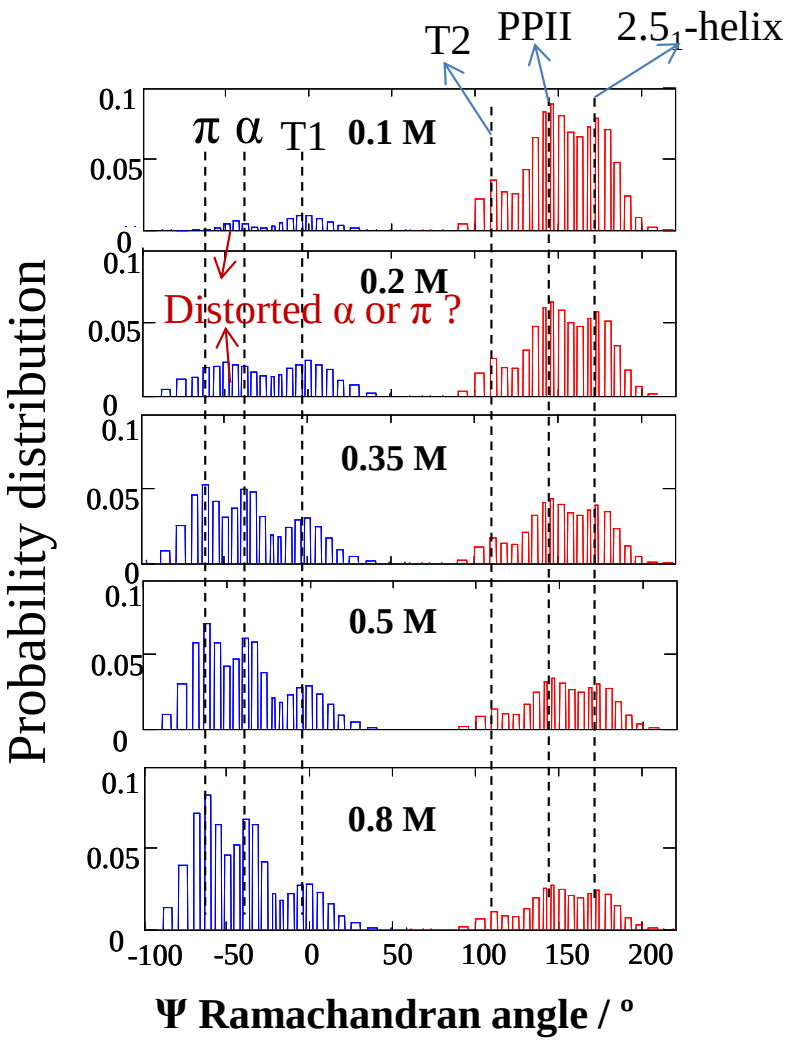

Figure 5.5. $NaClO_4$ concentration dependence of the Ramachandran Ψ angle distribution of PLL at pH 3 and 20 °C, assuming the T2 conformation at Ψ = 114°. The possible Ψ = 14° conformation is not shown. The extended structure Ψ angles are assumed to be those of PLL in the absence of $NaClO_4$ as in Fig. 5.1B.

5.3.3 Conformational Free Energy Landscape of PLL

We can use the calculated conformation population distribution of Fig. 5.5 to calculate the Gibbs free energy of the equilibrium conformations relative to the PPII conformation along

the Ψ Ramachandran angle folding reaction coordinate.[27,31] Fig. 5.6 shows the resulting energy landscape at different $NaClO_4$ concentrations at pH 3 and 20 °C. The energy landscape contains an α–helix–like conformational basin and an extended conformation energy basin.

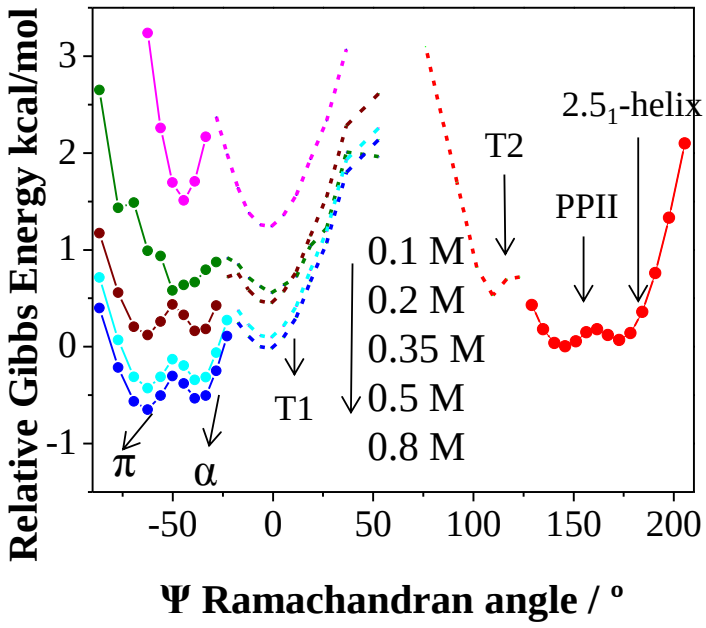

Figure 5.6. Calculated Gibbs free energy landscape for PLL at different $NaClO_4$ concentrations at pH 3 and 20 °C. The dotted lines show the turn regions, assuming that the T2 turn occurs at Ψ =114°.

At 0.1 M $NaClO_4$, the α–helical basin shows a double–well with a separate minima from the α–helix and the T1 turn structure. The α–helix and π–bulge conformations lie 1.5 kcal/mol above those of the PPII and 2.5_1–helix conformations. Increasing the $NaClO_4$ concentration lowers the α–helix–like conformation basin energy. At 0.2 M $NaClO_4$, the α–helix–like conformation is 0.58 kcal/mol above the PPII and 2.5_1–helix conformations. At 0.35 M $NaClO_4$, the α–helix or π–helix–like energy well splits into an α–helix, π–bulge and T1 triplet of energy minima. The α–helix, π–bulge and T1 triplet energies are similar to

those of the PPII and 2.5_1–helix conformations. At 0.8 M $NaClO_4$, the α–helix and π–bulge conformational energies are 0.55 and 0.65 kcal/mol below that of extended conformations, consistent with our previous study.[27] The relative energy of the T1 conformation energy decreases less than that of the α–helix and π–bulge conformations. The variations in shape of the PLL Gibbs free energy landscape with changing $NaClO_4$ concentration indicates that complex conformation changes occur as the $NaClO_4$ concentration increases.

5.3.4 UVRR Spectra of Protonated and Deuterated PLL

Deuteration of the PLL backbone N–H groups leads to significant PLL UVRR spectral changes[30] because the AmII, AmIII and C_α–H b bands involve significant N-H bending; deuteration removes the N–H in plane bending component, leaving an almost pure C–N s AmII' vibration at 1470 cm^{-1} and an AmIII' vibration at 935 cm^{-1} which has a large N–D bending component. Fig. 5.7 shows the pH 3 UVRR spectrum of PLL in the absence and presence of 0.8 M $NaClO_4$ in H_2O and D_2O. The AmIII, AmII and C_α–H b bands disappear and are replaced with the very strong AmII' band, and a weak AmIII' band (not shown). The UVRR spectra clearly differentiate between ND vs NH peptide bonds. The AmII' band is strong and well resolved, allowing for accurate quantitative analysis of the relative deuterated fraction.

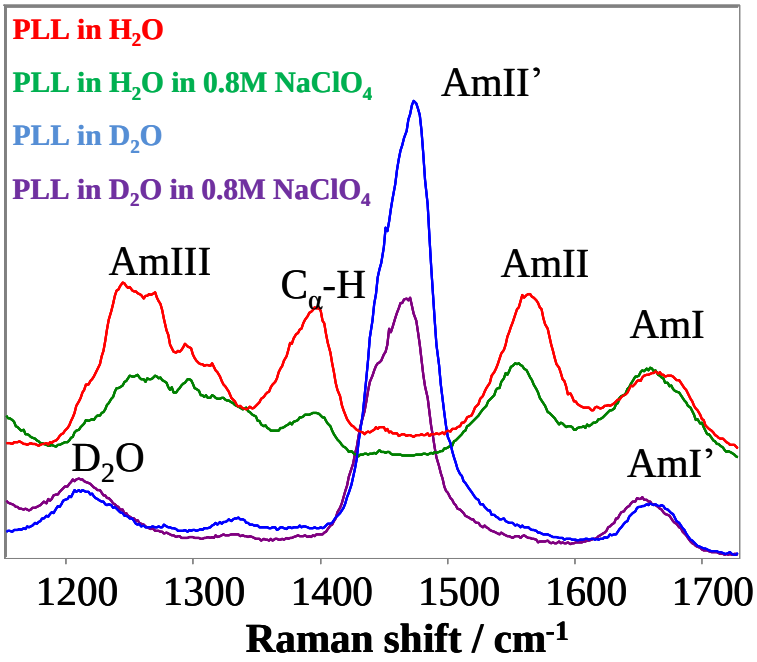

Figure 5.7. 204 nm UVRR spectra of PLL in the absence and presence of 0.8 M $NaClO_4$ in H_2O and D_2O at pH 3/pD 3 and at 20 °C.

5.3.5 $NaClO_4$ Dependence of PLL Amide Hydrogen Exchange Rate

We examined PLL hydrogen exchange at 0, 0.2, 0.35, 0.8 M $NaClO_4$ concentrations, by mixing PLL D_2O $NaClO_4$ solutions rapidly with H_2O $NaClO_4$ solutions. Fig. 5.8 shows the evolution of the UVRR on hydrogen exchange of PLL in the absence and presence of 0.8 M $NaClO_4$. The AmII' band gradually loses intensity upon replacement of N–D by N–H, while the AmII, C_α–H b and AmIII bands gain intensity.

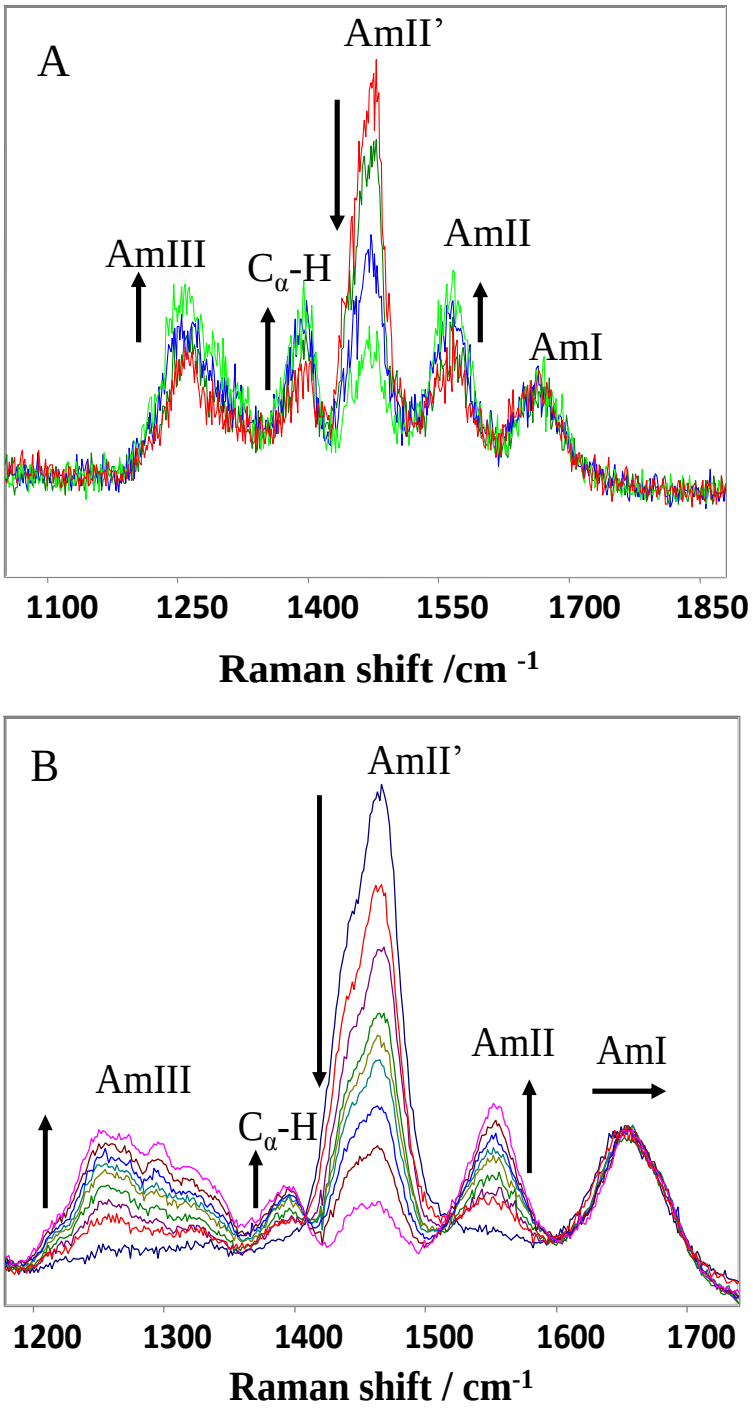

Figure 5.8. (A) pH 2.8 UVRR of PLL at 20 ºC hydrogen exchange at 28, 33, 43, and 103 s after H_2O addition in the absence of $NaClO_4$. (B) pH 2.8 UVRR PLL hydrogen exchange in 0.8 M $NaClO_4$ obtained at 3, 8, 12, 22, 32, 42, 64, 102 and 150 min after 0.8 M $NaClO_4$ H_2O solution addition.

Fig. 5.9 shows the normalized intensity decay of the AmII' band calculated as:

$$I_{N,AmII'}(t) = \frac{I_{AmII'}(t) - I_{AmII'}(\infty)}{I_{AmII'}(0) - I_{AmII'}(\infty)} \qquad (5.2)$$

where $I_{N,AmII'}(t)$ is the normalized AmII' intensity decay, whose value decreases from 1.0 to 0.0, $I_{AmII'}(t)$ is the experimentally observed AmII' band intensity at exchange time t, $I_{AmII'}(0)$ and $I_{AmII'}(\infty)$ are the AmII' band intensities at $t = 0$ and $t = \infty$. Since the AmII' band shapes at all exchange times for specific $NaClO_4$ concentration are almost identical, we utilized peak height intensities for analysis.

The 1459 cm^{-1} HOD bending band partially overlaps the AmII' band. Since the H_2O/D_2O rapidly reaches equilibrium, the HOD bending band contribution to the AmII' band intensity is constant at all times during the PLL hydrogen exchange. Thus, the HOD band subtracts off during the data analysis using eqn. 5.2.

As the $NaClO_4$ concentration increases, hydrogen exchange slows (Fig. 5.9). The apparent exchange rate is calculated by fitting the normalized AmII' band intensities. The AmII' intensity decay curves at 0, 0.2, and 0.35 M $NaClO_4$ concentrations at pH 2.8 are well fit by single exponentials with apparent exchange rates of 0.95, 0.11, 0.063 min^{-1}, respectively. The best single exponential fitting to the AmII' 0.8 M exchange curve gave an apparent exchange rate of 0.014 min^{-1}. However, Fig. 5.9 shows that the 0.8 M exchange curve does not fit well to a single exponential. Excellent fitting was obtained with a double exponential that give apparent rates of 0.022 min^{-1} and 0.00097 min^{-1} with weighting factors of 0.77 and 0.23 for the two exponents, respectively, as discussed below.

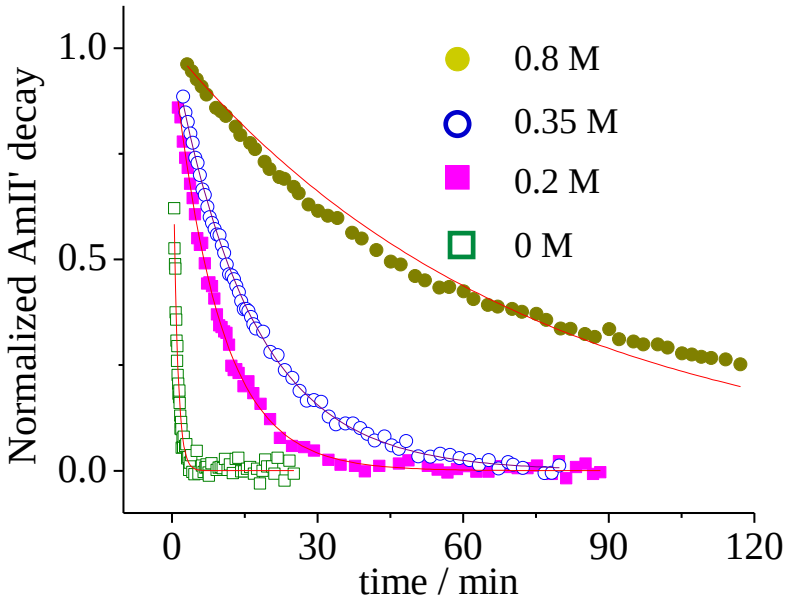

Figure 5.9. (A) Time dependence of normalized AmII' band intensity of PLL due to H–exchange at pH 2.8 at 20 °C at different $NaClO_4$ concentrations. The thin solid lines show single exponential fitting.

We also monitored the normalized intensity increase upon exchange that occurs for the C_α–H b band ($I_{N,C-H}(t)=(I_{C-H}(t)-I_{C-H}(0))/(I_{C-H}(\infty)-I_{C-H}(0))$) that is ploted together with $1-I_{N,AmII'}(t)$ in Fig. 5.10. At 0.0, 0.2 and 0.35 M $NaClO_4$ concentrations, the AmII' and C_α–H b band kinetics fully overlap.

We also monitored the normalized intensities of the 1567 cm^{-1} AmII band and the 1250 cm^{-1} and 1267 cm^{-1} components of the $AmIII_3$ band. At 0.0, 0.2 and 0.35 M $NaClO_4$ concentrations, the AmII and the $AmIII_3$ band kinetics overlap those of the AmII' band. However, at 0.8 M $NaClO_4$, the $I_{N,C-H}(t)$ kinetics are faster than that of $1-I_{N,AmII'}(t)$ as shown in Fig. 5.10. The AmII band kinetics is very close to that of the AmII' band, while the 1250 cm^{-1} and 1267 cm^{-1} $AmIII_3$ band kinetics fall between the $I_{N,C-H}(t)$ and $1-I_{N,AmII'}(t)$ kinetics (not shown).

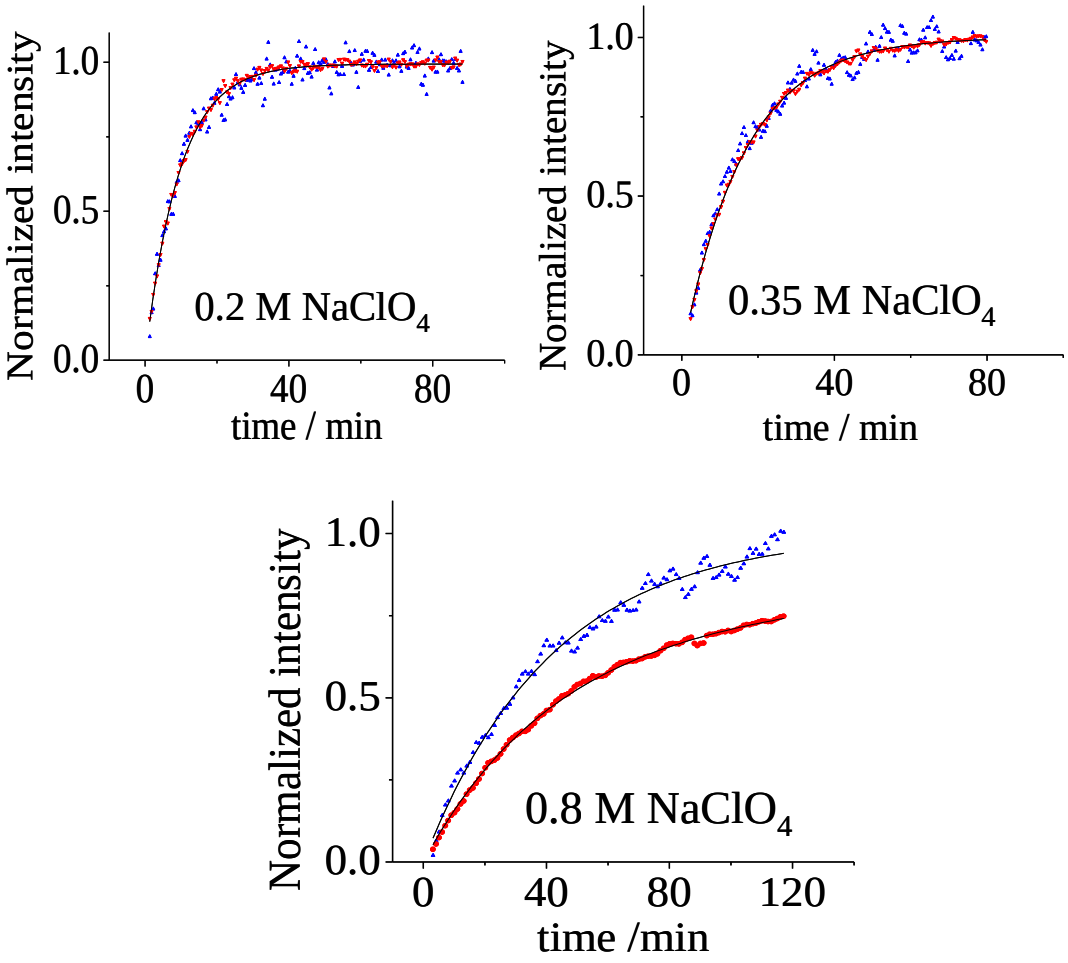

Figure 5.10. Comparison of $I_{N,C\text{-}H}$ (t) (blue) and 1–$I_{N,AmII'}$ (t) (red), exchange kinetics of the C_α–H b band and AmII' band at pH 2.8 at 20 °C. The black lines are single exponential (0.2, 0.35 M $NaClO_4$) and double exponential (0.8 M $NaClO_4$) fitting curves.

In the presence of $NaClO_4$ PLL has multiple conformations in equilibrium (α, π, turn, PPII, 2.5_1–helix etc.). All conformations with NH peptide bonds contribute to the AmII and AmIII bands, with the α–helical–like conformations contributing with lower Raman cross sections. Uniquely, the C_α–H b band is contributed only by NH peptide bond extended conformations. All ND peptide bonds contribute to the AmII' band, with the α–helical conformation showing a lower Raman cross section.

The exchange rates of peptide bond NH in the extended conformations can be selectively calculated from the C_α–H b band exchange kinetics shown in Fig. 5.10. At 0.0, 0.2 and 0.35 M, identical exchange rates are observed for the C_α–H b band from the extended structure, as from the AmII' band contributed by the predominant α-helix conformation. In sharp contrast, in 0.8 M $NaClO_4$, the extended conformation monitored 0.024 min^{-1} single exponential C_α–H b band calculated exchange rate is almost twice faster than that of the mainly α–helix AmII' band of 0.014 min^{-1}. As discussed above, the hydrogen exchange rates of peptide bond NH in the extended conformations slow as $NaClO_4$ concentration increases. The Am II and AmIII monitored D/H exchange kinetics show a poorer S/N because the magnitude of the spectral changes are attenuated by the overlapping slow α–helix exchange rates, and by the weaker, broader AmIII bands that contain partially overlapping contributions of α-helix-like and extended conformations.

The H/D exchange rates for PLL in solution should follow the scheme:

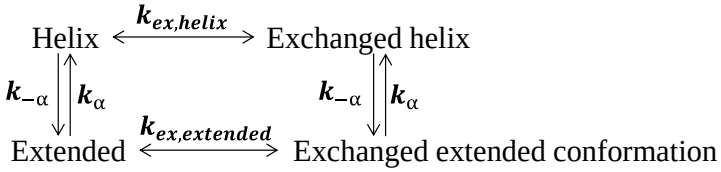

where 'Helix' and 'Extended' represent the α–helix–like and extended conformations, $k_{ex,helix}$ and $k_{ex,extended}$ refer to the H/D exchange rate constants of the peptide bond NH in the α–helix–like and extended conformations, respectively, k_α and $k_{-\alpha}$ are rate constants for the conformational transformation between the α–helix–like and extended conformations, and the equilibrium constant K= $k_{-\alpha}$ / k_α = [*extended*] / [*helix*]. At 0.0 M $NaClO_4$, only the extended conformation exists. At 0.2, 0.35, and 0.8 M $NaClO_4$, K= $k_{-\alpha}$ / k_α can be calculated to be 2.0, 0.82, and 0.39, respectively.

The overlapping time dependencies of the normalized intensities of the AmII', C_α–H b, AmII, and the 1250, 1267 cm^{-1} $AmIII_3$ band kinetics for 0.2 and 0.35 M $NaClO_4$ concentrations indicate that the hydrogen exchange rates for the extended and α–helix–like conformations are either identical, or the conformational interconversion rate is significantly faster than our H/D exchange measurement time scale. Since we expect the α–helix–like conformation to have a very slow D/H rate, we must conclude that we are actually monitoring the D/H exchange of the extended conformation, and that conformational exchange is very fast between the α–helix–like conformation and extended conformations.

However, the 0.8 M $NaClO_4$ solution PLL sample of Fig. 5.10 shows faster kinetics for the extended conformation C_α–H b band than for the predominantly α–helix AmII' band indicating that the extended structure undergoes D/H exchange faster than the α–helix **and** that the conformational interconversion rates are slow compared to the D/H exchange rates.

Thus, the conformational interconversion rate of PLL decreases as the $NaClO_4$ concentration increases. ClO_4^- binding probably increases the activation barriers restricting the conformational interconversion rate. Previous studies showed that peptide conformational dynamics could be influenced by the presence of salts.[41] Further, Dzubiella et al. MD simulations showed that the α–helical (un)folding kinetics of a ala–based peptide are slowed by the binding of ions to peptide charged groups.[42]

The 0.8 M $NaClO_4$ AmII' band normalized intensity time dependence is not well fit to a single exponential, presumably because the extended conformation and α–helix–like conformations have different exchange rates. The double exponential fit to $1–I_{N,AmII'}(t)$:

$$1 - I_{N,AmII'}(t) = 1 - ae^{-k_1 t} - (1-a)e^{-k_2 t} \quad (5.3)$$

where k_1=0.022 ± 0.001min^{-1}, k_2 =0.00097 ± 0.00128min^{-1} and a=0.77 ± 0.04.

The amide NH exchange rate obtained from the excellent single exponential fit to the C_α–H b band exchange kinetics is k=0.024 min^{-1}, which is very close to the k_1 rate obtained from the AmII' band kinetics. This similarity suggests that the k_1 kinetics derives from the D/H exchange of the extended conformations, leaving the k_2 kinetics to derive from the α–helix–like conformations.

Assuming we have only extended and α–helix–like conformations we expect parameter a to be given as:

$$a = \frac{\sigma_{extended} f_{extended}}{\sigma_{extended} f_{extended} + \sigma_{helix} f_{helix}} \quad (5.4)$$

where $f_{extended}$ and f_{helix} are the PLL fraction of extended and α–helix–like conformations in the presence of 0.8 M $NaClO_4$. σ_{helix} and $\sigma_{extended}$ are the AmII' band cross sections of the α–helix–like and extended conformations.

Assuming that the Raman cross sections of the extended and α–helix–like conformations are identical in the presence and absence of $NaClO_4$, $\sigma_{extended}/\sigma_{helix}$ can be estimated from the measured pH~3 PLL UVRR AmII' band intensities in D_2O in the absence and presence of 0.8 M $NaClO_4$ (Fig. 5.7). Using the AmI' band as an internal intensity standard, the measured AmII' band integrated intensity ratio in the absence and presence of 0.8 M $NaClO_4$, $I_{AmII',0MClO4}/I_{AmII',0.8MClO4}$ is measured to be 1.78±0.05. Since

$$\frac{I_{AmII',0MClO_4}}{I_{AmII',0.8MClO_4}} = \frac{f_{extended,0MClO_4}\sigma_{extended,AmII'} + f_{helix,0MClO_4}\sigma_{helical,AmII'}}{f_{extended,0.8ClO_4}\sigma_{extended,AmII'} + f_{helix,0.8MClO_4}\sigma_{helical,AmII'}} \quad (5.5)$$

Given our determined PLL extended conformational fractions at 0.0 and 0.8 M $NaClO_4$ are 100% and 28%, we estimate the AmII' band Raman cross section ratio of the extended conformation to the α–helix–like conformation is 2.55±0.15. Using this cross section ratio

and eqn. 5.4, we calculate a = 0.50 ± 0.02, which is somewhat less than that of the fitted kinetic result (0.77). This indicates our 2–state H/D exchange model fails to fully account for the PLL exchange kinetics.

5.3.6 $NaClO_4$ Decreases the H/D Exchange Rates of Extended Conformation Peptide Bonds

Fig. 5.11, which shows the $NaClO_4$ concentration dependence of the exponential exchange rates, shows that increasing $NaClO_4$ concentrations rapidly decreases the H/D exchange rate of the peptide bond ND. We can model this dependence at 0, 0.2 and 0.35 M $NaClO_4$ concentrations where the conformational exchange rates are fast by assuming that ClO_4^- is a competitive inhibitor of the PLL H/D exchange. In the Appendix we calculate the impact of ClO_4^- binding on the extended PLL D/H exchange rate by modeling our observed exchange rate, k_{obs} of Fig. 5.11:

$$\frac{k_{obs}}{f_{extended}} = \frac{k_{ex}}{1 + K[ClO_4^-]} \quad (5.6)$$

Fitting the apparent exchange rate constant, k_{obs} at different $NaClO_4$ concentrations (Fig. 5.11) gives an intrinsic D/H exchange rate of k_{ex} = 0.95 ± 0.03, and a ClO_4^- association equilibrium constant to extended PLL of K = 21 ± 4. Thus, ClO_4^- binds to extended PLL at a site close to the peptide bond N–D to protect it against D/H exchange that is primarily catalyzed by OH^-. This base catalyzed reaction occurs through abstraction of the amide NH by direct interaction with OH^-.[43] The model above predicts that increasing the pH should speed up the D/H exchange rate because of an increased competing OH^- concentration. We find that the D/H exchange of PLL at pH 6.5 in 0.8 M $NaClO_4$ is faster than the dead time of

our exchange measurement (< 1min); the pH 6.5 in 0.8 M $NaClO_4$ PLL UVRR is identical to that at pH 2.8, indicating identical PLL conformations.

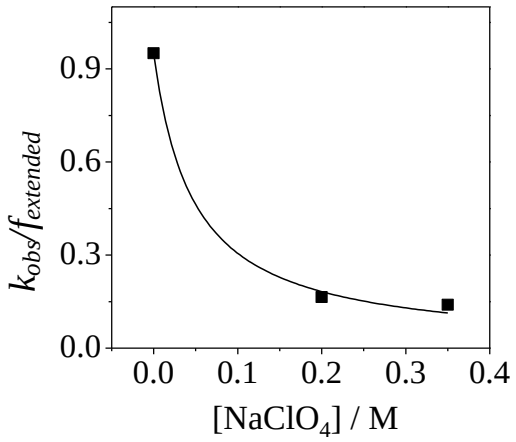

Figure 5.11. $NaClO_4$ concentration dependence of extended PLL exchange rates. The solid line shows the eqn. 5.6 fitting result.

The ClO_4^- induced decrease in the peptide bond NH exchange rates in the extended PLL conformations indicates a specific ClO_4^- binding geometry that protects the backbone peptide bond ND from exchange. Fig. 5.12 shows how ClO_4^- ion could interact both with extended conformation peptide bond ND and the neighboring lysine $-NH_3^+$ group through hydrogen bonding and electrostatic interactions to transiently form stable ring structures that protects the amide NH from exchange.

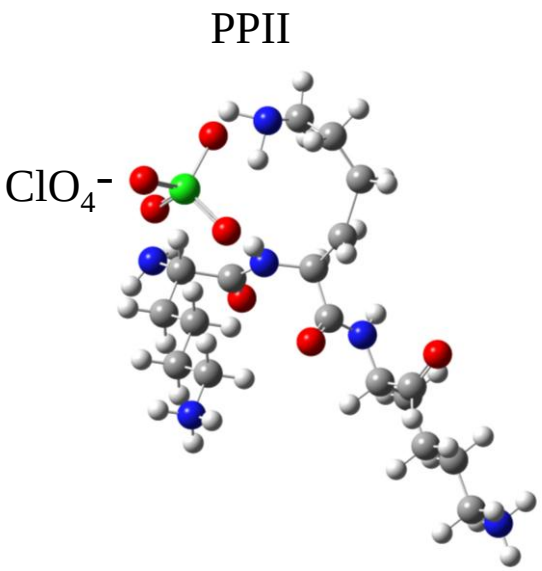

Figure 5.12. Interactions between ClO_4^- and PLL in the PPII conformation to protect the peptide NH from exchange. The ClO_4^- ion binds to the amide NH and neighboring lysine $-NH_3^+$ group to form a ring structure.

5.4 CONCLUSION

We examined the impact of $NaClO_4$ on poly–L–lysine's conformational equilibrium and its hydrogen exchange kinetics. The presence of $NaClO_4$ induces charged PLL to fold into α–helical–like conformations. Extended conformations such as the PPII and 2.5_1–helix conformations dominate the PLL equilibria at low $NaClO_4$ concentrations. In contrast, at higher $NaClO_4$ concentrations α–helical–like conformations that consist of turn, α–helix and π–helix/bulge conformations dominate. The conformational population Ψ angle distribution and the Gibbs free energy landscape of PLL were calculated along the Ramachandran Ψ angle folding coordinate.

We find that the D/H exchange kinetics of PLL at 0, 0.2, 0.35 and 0.8 M $NaClO_4$ concentrations slow as the $NaClO_4$ concentration increases. The kinetics of the AmII' and C_α–H b bands are identical at 0, 0.2 and 0.35 M $NaClO_4$ concentrations which indicates that the conformational interconversion rates are significantly faster than our H/D exchange measurement time scale.

At 0.8 M $NaClO_4$ concentration the AmII' band intensity kinetics requires a double exponential fit. In addition, the C_α–H b band extended structure D/H kinetics are faster than that of the AmII' band indicating that the PLL conformational interconversion rate is slowed by $NaClO_4$. The exchange rate of the extended structure is much faster than that of the α–helix structure. These results allow us to determine the association constant of perchlorate to the extended PLL conformation, and allow us to propose a binding geometry.

A**CKNOWLEDGMENT**

This work is supported by NIH Grant No. 1R01EB009089.

5.5 APPENDIX: NACLO$_4$ INHIBITS H/D EXCHANGE OF EXTENDED PLL AT LOW PH

Our results in Fig. 5.11 that show a slowing H/D exchange rate as the ClO_4^- concentration increases indicates that the deuterated amide ND peptide bonds in PLL are protected from exchange by binding of ClO_4^- and PLL to form the ND–ClO_4 complexes. The exchange process of the extended conformations is described by

$$ND{-}ClO_4 \underset{k_a}{\overset{k_{-a}}{\rightleftharpoons}} ND + ClO_4^- \overset{k_{ex}}{\rightleftharpoons} NH + ClO_4^- \underset{k_{-a}}{\overset{k_a}{\rightleftharpoons}} NH{-}ClO_4$$

The first and third steps are the association reactions that occur between extended conformations of PLL and ClO_4^-, where k_a and k_{-a} are the association and dissociation rate constants. k_{ex} is the D to H exchange rate constant. The ClO_4^- association and dissociation steps are very fast and the reaction is assumed to be in ClO_4^- exchange equilibrium.

The equilibrium association reaction constant between extended PLL and ClO_4^- is

$$K = \frac{k_a}{k_{-a}} = \frac{[ND - ClO_4]}{[ND][ClO_4^-]} \qquad (5\text{-A1})$$

So that

$$[ND - ClO_4] = K[ND][ClO_4^-] \quad (5\text{-A2})$$

$$[ND - ClO_4] + [ND] = K[ND][ClO_4^-] + [ND] \quad (5\text{-A3})$$

$$[ND] = \frac{[ND] + [ND - ClO_4]}{1 + K[ClO_4^-]} \quad (5\text{-A4})$$

During the H/D exchange process, at low and modearate ClO_4^- concentrations (0.2 and 0.35 M) we can assume fast conformational exchange such that the extended and α–helix–like conformations are in equilibrium. Thus, the extended conformational fraction is:

$$f_{extended} = \frac{[ND] + [ND - ClO_4]}{[ND] + [ND - ClO_4] + [\alpha - D] + [\alpha - D - ClO_4]} \quad (5\text{-A5})$$

where [α–D] and [α–D–ClO_4] are the unbound and bound ClO_4^- states of α–helix–like conformations. The measured overall hydrogen exchange rate is

$$-\frac{d([ND] + [ND - ClO_4] + [\alpha - D] + [\alpha - D - ClO_4])}{dt} = k_{ex}[ND] \quad (5\text{-A6})$$

The hydrogen exchange rate of the extended conformation is obtained from eqn. (5-A6):

$$-\frac{d([ND]+[ND-ClO_4])}{dt} = f_{extended}\, k_{ex}\, [ND] \qquad \text{(5-A7)}$$

Substituting eqn. (5-A4) into (5-A7) yields

$$-\frac{d([ND]+[ND-ClO_4])}{dt} = f_{extended}\; k_{ex}\; \frac{[ND]+[ND-ClO_4]}{1+K[ClO_4^-]} \qquad \text{(5-A8)}$$

Reorganizing (5-A8),

$$-\frac{d([ND]-[ND-ClO_4])}{[ND]-[ND-ClO_4]} = \frac{f_{\,extended}\; k_{ex}}{1+K[ClO_4^-]}dt \quad \text{(5-A9)}$$

Thus, the apparent exchange rate constant of the extended conformation is a function of the ClO_4^- concentration:

$$k_{obs} = \frac{f_{extended} k_{ex}}{1+K[ClO_4^-]} \quad \text{(5-A10)}$$

Rearrange the eqn. (5-A10), and eqn. 5.6 is obtained.

5.6 REFERENCE

(1) Baldwin, R. L.; Rose, G. D. *Trends Biochem. Sci.* **1999**, *24*, 26-33.

(2) Creighton, T. E., (Editor) *Protein Structure, Second Edition*; W.H. Freeman: New York, 1997.

(3) Dill, K. A. *Biochemistry* **1985**, *24*, 1501-9.

(4) Dill, K. A. *Protein Sci.* **1999**, *8*, 1166-1180.

(5) Dobson, C. M.; Sali, A.; Karplus, M. *Angew. Chem. Int. Ed.* **1998**, *37*, 868-893.

(6) Dill, K. A.; Ozkan, S. B.; Shell, M. S.; Weikl, T. R. *Annu. Rev. Biophys.* **2008**, *37*, 289-316.

(7) Anfinsen, C. B. *Science* **1973**, *181*, 223-30.

(8) Anfinsen, C. B.; Scheraga, H. A. *Adv. Prot. Chem.* **1975**, *29*, 205-300.

(9) Haber, E.; Anfinsen, C. B. *J. Biol. Chem.* **1962**, *237*, 1839-44.

(10) Levinthal, C. *J. Chim. Phys.* **1968**, *65*, 44-45.

(11) Royer, C. A. *Chem. Rev.* **2006**, *106*, 1769-1784.

(12) Gruebele, M. *Annu. Rev. Phys.l Chem.* **1999**, *50*, 485-516.

(13) Ervin, J.; Sabelko, J.; Gruebele, M. *J. Photochem. Photobiol., B: Biol.* **2000**, *54*, 1-15.

(14) Amunson, K. E.; Ackels, L.; Kubelka, J. *J. Am. Chem. Soc.* **2008**, *130*, 8146-8147.

(15) Barth, A.; Zscherp, C. *Q. Rev. of Biophys* **2002**, *35*, 369-430.

(16) Buchner, G. S.; Murphy, R. D.; Buchete, N.-V.; Kubelka, J. *Biochim. Biophys. Acta, Proteins and Proteomics* **2011**, *1814*, 1001-1020.

(17) Borgia, A.; Williams, P. M.; Clarke, J. *Annu. Rev. Biochem.* **2008**, *77*, 101-125.

(18) Schuler, B. *ChemPhysChem* **2005**, *6*, 1206-1220.

(19) Schuler, B.; Lipman, E. A.; Eaton, W. A. *Nature* **2002**, *419*, 743-747.

(20) Rhoades, E.; Gussakovsky, E.; Haran, G. *Proc. Nat. Acad. Sci. U. S. A.* **2003**, *100*, 3197-3202.

(21) Cecconi, C.; Shank, E. A.; Bustamante, C.; Marqusee, S. *Science* **2005**, *309*, 2057-2060.

(22) Suarez, M.; Jaramillo, A. *J. R. Soc. Interface* **2009**, *6*, S477-S491.

(23) Morra, G.; Meli, M.; Colombo, G. *Curr. Protein Pept. Sci.* **2008**, *9*, 181-196.

(24) Thirumalai, D.; O'Brien, E. P.; Morrison, G.; Hyeon, C. *Annu. Rev. Biophys.*, *39*, 159-183.

(25) Dearborn, D. G.; Wetlaufer, D. B. *Biochem. Biophys. Res. Commun.* **1970**, *39*, 314-320.

(26) Painter, P. C.; Koenig, J. L. *Biopolymers* **1976**, *15*, 229-240.

(27) Ma, L.; Ahmed, Z.; Mikhonin, A. V.; Asher, S. A. *J. Phys. Chem. B* **2007**, *111*, 7675-7680.

(28) Bykov, S.; Lednev, I.; Ianoul, A.; Mikhonin, A.; Munro, C.; Asher, S. A. *Appl. Spectrosc.* **2005**, *59*, 1541-1552.

(29) Lednev, I. K.; Karnoup, A. S.; Sparrow, M. C.; Asher, S. A. *J. Am. Chem. Soc.* **1999**, *121*, 8074-8086.

(30) Ma, L.; Ahmed, Z.; Asher, S. A. *J. Phys. Chem. B* **2011**, *115*, 4251-4258.

(31) Mikhonin, A. V.; Myshakina, N. S.; Bykov, S. V.; Asher, S. A. *J. Am. Chem. Soc.* **2005**, *127*, 7712-7720.

(32) Ebert, G.; Kuroyanagi, Y. *Polymer* **1982**, *23*, 1147-1153.

(33) Ebert, G.; Kuroyanagi, Y. *Polymer* **1982**, *23*, 1154-1158.

(34) Goto, Y.; Takahashi, N.; Fink, A. L. *Biochemistry* **1990**, *29*, 3480-3488.

(35) Woody, R. W. In *Circular Dichroism and the Conformational Analysis of Biomolecules*; Fasman, G. D., Ed.; Plenum Press: New York, 1996.

(36) Reed, J.; Reed, T. A. *Analytical Biochemistry* **1997**, *254*, 36-40.

(37) Ozdemir, A.; Lednev, I. K.; Asher, S. A. *Biochemistry* **2002**, *41*, 1893-1896.

(38) Mikhonin, A. V.; Bykov, S. V.; Myshakina, N. S.; Asher, S. A. *J. Phys. Chem. B* **2006**, *110*, 1928-1934.

(39) Asher, S. A.; Ianoul, A.; Mix, G.; Boyden, M. N.; Karnoup, A.; Diem, M.; Schweitzer-Stenner, R. *J. Am. Chem. Soc.* **2001**, *123*, 11775-11781.

(40) Asher, S. A.; Mikhonin, A. V.; Bykov, S. B. *J. Am. Chem. Soc.* **2004**, *126*, 8433-8440.

(41) Dzubiella, J. *J. Phys. Chem. B* **2010**, *114*, 7098-7103.

(42) von Hansen, Y.; Kalcher, I.; Dzubiella, J. *J. Phys. Chem. B* **2010**, *114*, 13815-13822.

(43) Dempsey, C. E. *Prog. Nucl. Magn. Reson. Spectrosc.* **2001**, *39*, 135-170.

CHAPTER 6

Resolution Enhancement Mechanism in Generalized Two-Dimensional Correlation Spectroscopy

This Chapter was submitted to Applied Spectrosocpy. The co-authors are Lu Ma, Vitali Sikirzhytski, Zhenmin Hong, Igor Lednev, Sanford Asher.

6.0 RESOLUTION ENHANCEMENT MECHANISM IN GENERALIZED TWO-DIMENSIONAL CORRELATION SPECTROSCOPY

Generalized two-dimensional correlation spectroscopy (2D COS) can be used for resolution enhancement to differentiate highly overlapped spectral bands. Despite recent extensive 2D COS studies, the origin of the 2D spectral features and the resolution enhancement mechanism are not understood completely. In this work, we studied 2D COS of simulated spectra and developed new insights into the dependence of the 2D COS spectral features on the overlapping band separations, intensities and bandwidths, and the band intensity change rates. We elucidate the origins of the spectral features of the overlapping band 2D COS spectra, and identify the conditions required to resolve overlapping bands.

6.1 INTRODUCTION

Two-dimensional correlation spectroscopy (2D COS) was first introduced by Noda,[1-5] as a mathematical technique to investigate the behavior of a system in response to external perturbations (temperature, pH, concentration, time etc.). 2D COS has been successfully applied to analyze NMR, IR, Raman, UV-Vis, fluorescence spectra etc.[4-7] 2D COS establishes correlations between spectral intensity variations within a set of spectra by generating two-dimensional maps that are known as the 2D synchronous and asynchronous

spectra. Information such as the similarity, direction, and sequential order of correlated spectral intensity variations can be extracted by studying the 2D correlation peak features.[5,8] 2D COS enhances spectral resolution by spreading highly overlapped band features along a second dimension.[7,9-11] 2D COS has been shown to be a powerful tool to study spectra of complex systems such as polymers, colloids, proteins, peptides, and pharmaceuticals.[12-14] The presence of multiple overlapping bands is revealed by the occurrence of multiple correlation peaks in the 2D synchronous and asynchronous spectra.[12-14]

Despite the numerous studies, the resolution enhancement mechanism of 2D COS is still not completely understood. 2D synchronous or asynchronous correlated peaks occur if the intensities of two spectral features change in-phase or out-of-phase with each other.[5] Although it is generally expected that the number of correlation peaks will be equal to the number of overlapping bands, this result does not always occur. For example, Yu et al. surprisingly found the presence of three correlation peaks in the 2D COS spectra of simulated spectra where an overlapping narrow band was embedded within a broad band.[15]

In the work here, we examine the dependence of the 2D COS spectral features on the overlapping band separations, band intensities and bandwidths, and the rates of band intensity changes. We identify the conditions required to resolve overlapping bands.

6.2 EXPERIMENTAL SECION

6.2.1 2D Correlation Analysis

Noda proposed a practical method to compute generalized 2D correlation spectra.[5,16] Assuming a set of *m* spectra collected over perturbation *t* at equally spaced increments, the 2D synchronous $\Phi(\nu_1,\nu_2)$ and asynchronous $\Psi(\nu_1,\nu_2)$ correlation intensities at ν_1 and ν_2 are calculated:

$$\Phi(\nu_1,\nu_2) = \frac{1}{m-1}\tilde{y}(\nu_1)^T \tilde{y}(\nu_2) \quad (6.1)$$

$$\Psi(\nu_1,\nu_2) = \frac{1}{m-1}\tilde{y}(\nu_1)^T N \ \tilde{y}(\nu_2) \quad (6.2)$$

where $\tilde{y}(\nu_i)$ is the dynamic spectral intensity matrix,

$$\tilde{y}(\nu_i) = \tilde{y}(\nu_i,t) = \begin{bmatrix} \tilde{y}(\nu_i,t_1) \\ \tilde{y}(\nu_i,t_2) \\ \cdots \\ \tilde{y}(\nu_i,t_m) \end{bmatrix} \quad (6.3)$$

$\tilde{y}(\nu_i,t_j)$ is the dynamic spectral signal at ν_i and time t_j defined by the following equation:

$$\tilde{y}(\nu_i,t_j) = y(\nu_i,t_j) - \frac{1}{m}\sum_{k=1}^{m} y(\nu_i,t_k) \quad (6.4)$$

where $y(\nu_i,t_j)$ is the measured spectral signal at ν_i and time t_j. N in eqn. (6.2) is the Hilbert-Noda matrix, given by

$$N = \frac{1}{\pi}\begin{bmatrix} 0 & 1 & \frac{1}{2} & \frac{1}{3} & \ldots \\ -1 & 0 & 1 & \frac{1}{2} & \ldots \\ -\frac{1}{2} & -1 & 0 & 1 & \ldots \\ -\frac{1}{3} & -\frac{1}{2} & -1 & 0 & \ldots \\ \ldots & \ldots & \ldots & \ldots & \ldots \end{bmatrix} \qquad (6.5)$$

The synchronous spectrum is the inner product of two dynamic spectral vectors measured at two different spectral frequencies, ν_1 and ν_2. The asynchronous spectrum is the inner product of the dynamic spectral vectors and the orthogonal Hilbert-Noda matrix.

The 2D correlation spectra here were calculated as discussed above. We will consider here only those cross-peaks located below the correlation diagonal and label them as (ν_1, ν_2), where ν_1, ν_2 refer to the abscissa and ordinate spectral frequencies.

6.2.2 Simulations

The simulated spectra used here were composed of 13 Gaussian bands $I_{i0}(\nu) = A_i e^{-\frac{(\nu-\nu_{ci})^2}{2w_i^2}}$ as shown in Fig. 6.1A, where w_i determines the full bandwidth at half height ($FWHH = 2\sqrt{2\ln 2}w_i$), ν_{ci} is the band center frequency, ν is the spectral frequency, and A_i is the maximum amplitude of the *i*th Gaussian band. The *i*th band intensity decreases exponentially with time as $f_i(t) = e^{-k_i t}$. In the following discussion, B*i* refers to the *i*th band.

The Gaussian band parameters and their intensity change functions are summarized in Table 6.1. The first five bands have identical maximum intensities and bandwidths and are separated by 100 cm^{-1}. The other eight bands are paired to form 4 overlapping bands B6/B7,

B8/B9, B10/B11 and B12/B13. B6 and B7 are separated by 30 cm^{-1}, while B8 and B9, B10 and B11, B12 and B13 are separated by 8 cm^{-1}. All bands have w =14 cm^{-1}, except for B9 and B11 where w = 11 cm^{-1}, and B13 with w=5 cm^{-1}. All bands have A= 100, except for B11 where A= 36.

The B1 to B5 band intensity change rate constants k are 0.05, 0.085, 0.1, 0.15, and 0.2 sec^{-1}, respectively. For B6, B8, B10, and B12, k=0.05 sec^{-1}, and for B7, B9, B11, and B13 k =0.2 sec^{-1}.

Fig. 6.1B shows the simulated spectra

$$I(\nu,t) = \sum_{i=1}^{m} f_i(t) I_{i0}(\nu) \qquad (6.6)$$

where m=13 is the number of the Gaussian bands, and $f_i(t)$ is defined as the **intensity change coefficient** calculated as $f_j(t) = e^{-k_i t}$.

The simulation consists of 21 spectra with spectrum 1 the starting spectrum at t = 0 *sec*. The time interval between spectra is 1 *sec*. The spacing between spectral data points is 2 cm^{-1}.

Table 6.1. Gaussian band parameters and the band intensity change functions.

	f(t)	ν_c (cm^{-1})	*A*	*w* (cm^{-1})
B1	$e^{-0.05t}$	1370	100	14
B2	$e^{-0.085t}$	1470	100	14
B3	$e^{-0.1t}$	1570	100	14
B4	$e^{-0.15t}$	1670	100	14
B5	$e^{-0.2t}$	1770	100	14
B6	$e^{-0.05t}$	1870	100	14

B7	$e^{-0.2t}$	1900	100	14
B8	$e^{-0.05t}$	2000	100	14
B9	$e^{-0.2t}$	2008	100	11
B10	$e^{-0.05t}$	2100	100	14
B11	$e^{-0.2t}$	2108	36	11
B12	$e^{-0.05t}$	2200	100	14
B13	$e^{-0.2t}$	2208	100	5

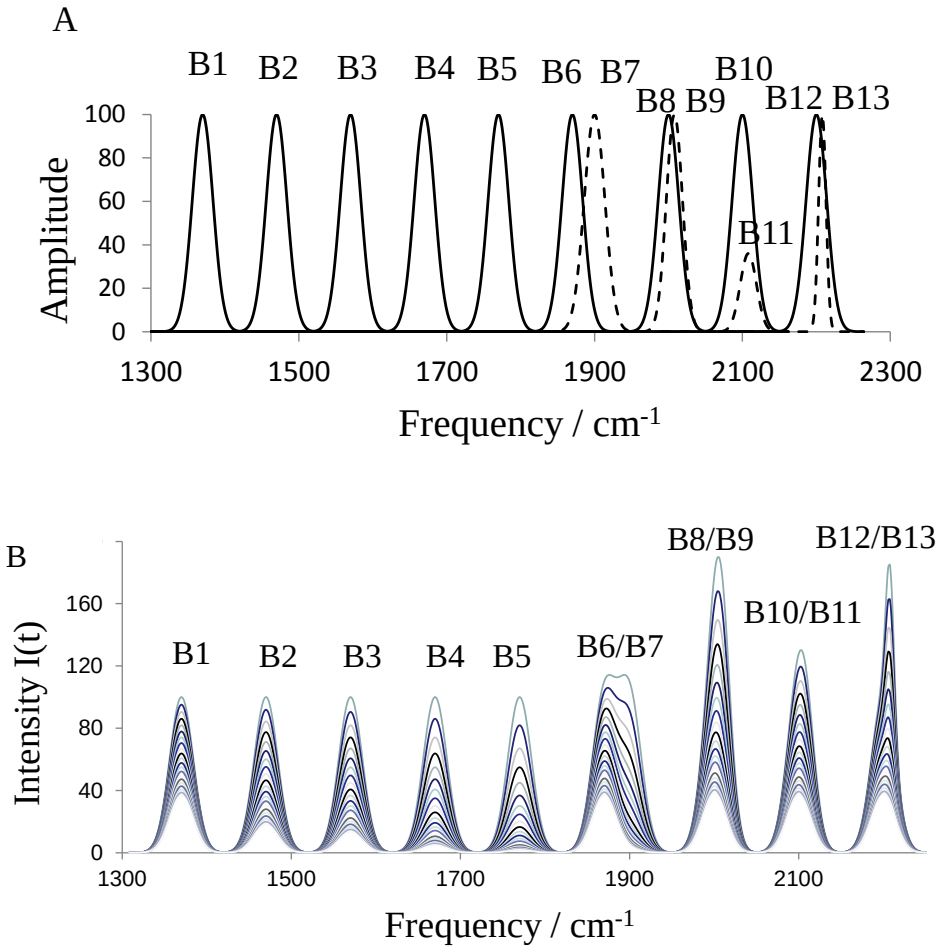

Figure 6.1. (A) 13 Gaussian band spectra. (B) Simulated spectra.

6.2.3 Spectral Normalization

The normalized spectral intensity $F(\nu,t)$ is calculated:

$$F(\nu,t)=[I(\nu,t)-I(\nu,0)]/[I(\nu,T)-I(\nu,0)] \qquad (6.7)$$

where $I(\nu,t)$ is the spectral intensity at t.[17] Normalization makes the spectral intensities range from 0 to 1 over the total perturbation time T. The results of spectral signal intensity normalization are shown in Fig. 6.2. Eqn. (6.7) can be rewritten:

$$I(\nu,t) = K(\nu)F(\nu,t) + b \qquad (6.8)$$

where $K(\nu) = I(\nu,T) - I(\nu,0)$, and $b = I(\nu,0)$. The **normalized half-intensity (NHI)** is defined as the normalized intensity at t=T/2, as shown in Fig. 6.2B.

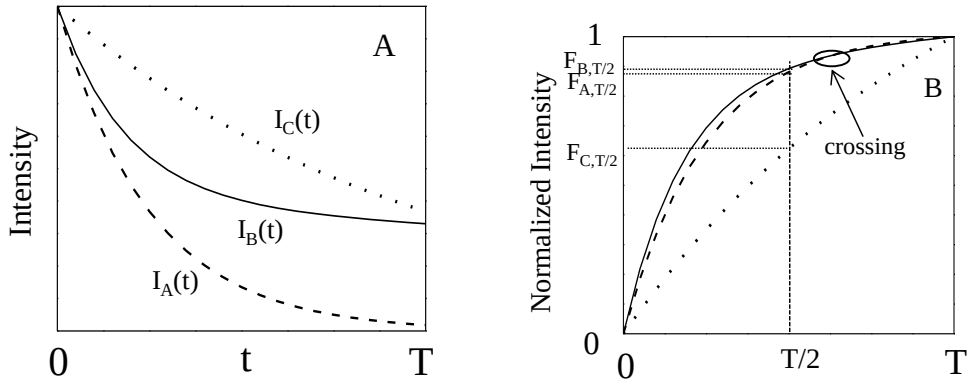

Figure 6.2. Example of spectral intensity normalization. (A) Time dependence of intensities of bands $I_A(t) = e^{-0.2t}$, $I_B(t) = 0.4e^{-0.01t} + 0.6e^{-0.27t}$ and $I_C(t) = e^{-0.05t}$. (B) Normalized intensity time dependence of these bands. $F_{A,T/2}$, $F_{B,T/2}$ and $F_{C,T/2}$ refer to the NHI of these bands. The black oval shows the region where the normalized intensities of band *A* and *B* cross.

Recently, as a further interpretation of Noda's sequential rule,[5] Yu et al proposed the following correlation of the signs of the synchronous and asynchronous cross-peaks to the **relative values of the NHI** at v_1 and v_2 (Fig. 6.2)[17]: *if* $\Phi(v_1, v_2)\Psi(v_1, v_2) > 0$*, then the spectral NHI at* v_1 *is larger than that at* v_2*; If* $\Phi(v_1, v_2)\Psi(v_1, v_2) < 0$*, then the spectral NHI at* v_1 *is smaller than that at* v_2. The relationship was verified for spectra consisting of non-overlapping bands where the *band intensities change monotonically* and where the *normalized intensity time dependencies do not cross* (Fig. 6.2B).[17]

6.3 RESULTS AND DISCUSSION

6.3.1 2D Correlation Result of Simulated Spectra

Significant resolution enhancement is provided by 2D COS. Fig. 6.1B shows that only the overlapping B6/B7 bands can be visually resolved in the one dimensional spectra. Fig. 6.3 shows the 2D COS spectra generated by correlating the simulated spectra of the non-overlapping bands B1 to B5 with the overlapping bands B6 to B13. The synchronous and asynchronous spectral correlation peak features differ for different overlapping bands, due to differences in band separations, band intensities, bandwidths, and temporal intensity changes (Fig. 6.3).

Fig. 6.3A shows the 2D COS synchronous spectra. The positive signs of the auto-peaks and cross-peaks in the synchronous spectrum indicate that the spectral intensity changes of all bands occur in the same direction. In this case, the 2D COS synchronous

spectrum does not provide more information than does the original one-dimensional spectrum; no resolution improvement occurs.

A. 2D synchronous spectrum

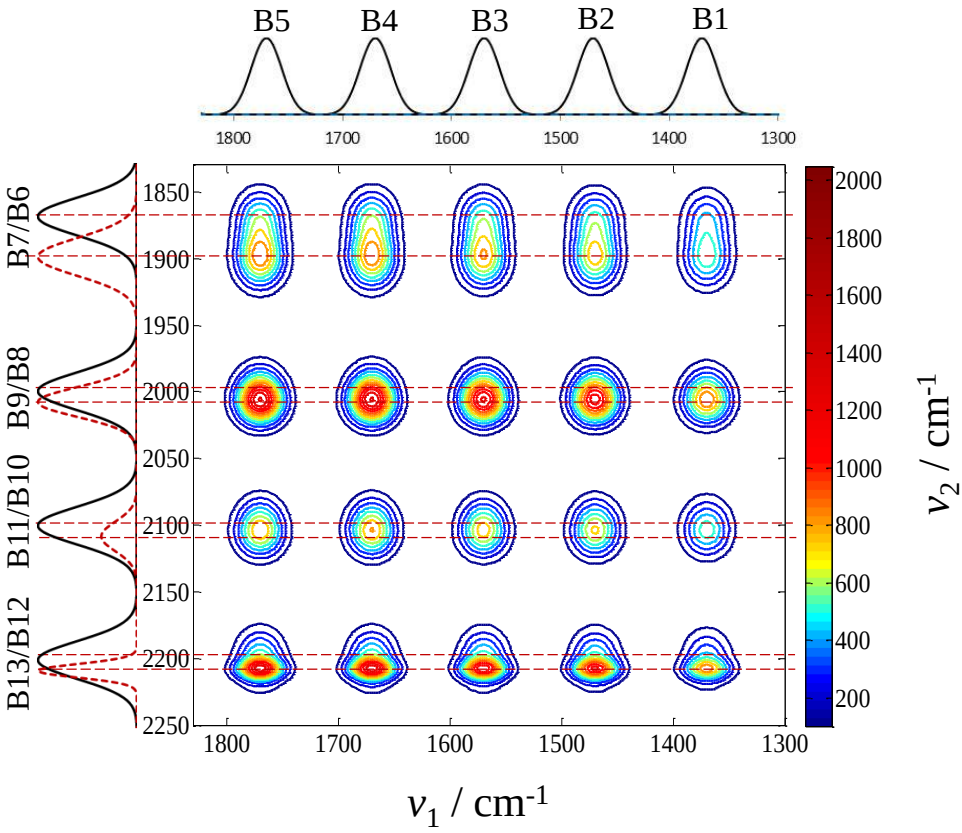

B. 2D asynchronous spectrum

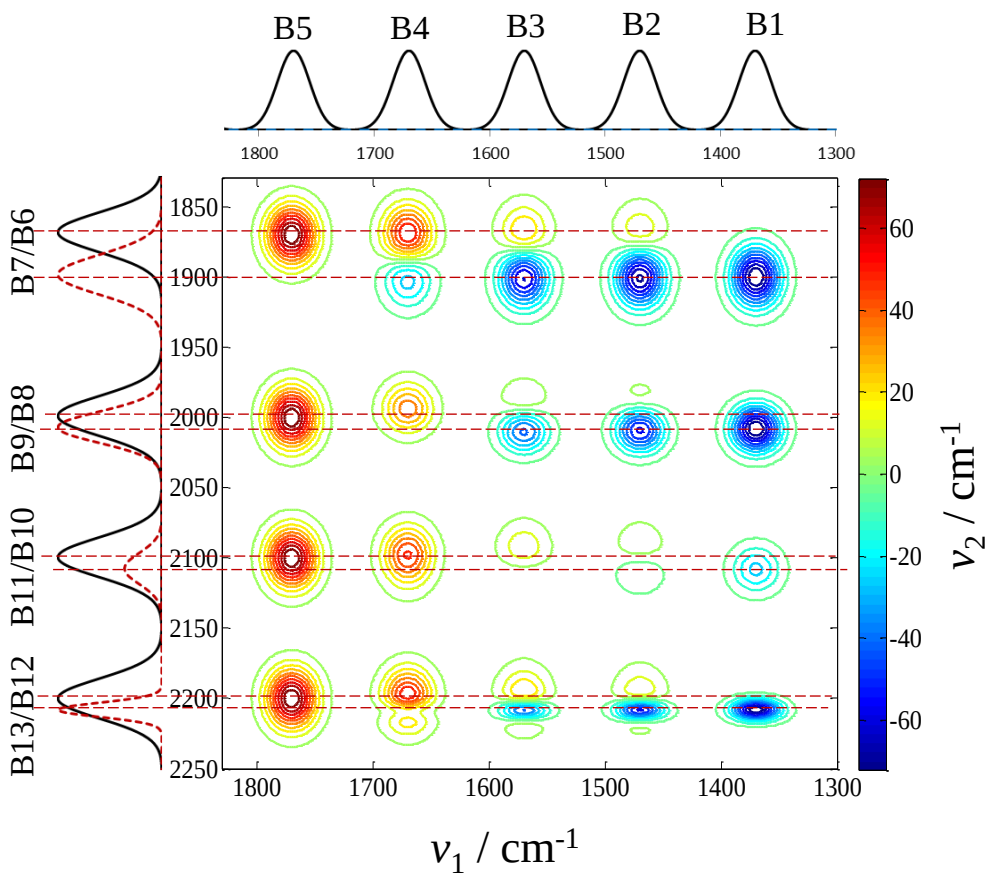

Figure 6.3. 2D COS (A) Synchronous and (B) Asynchronous spectrum calculated from the simulated spectra of Fig. 6.1B. The dashed horizontal lines indicate the Gaussian band maxima.

The occurrence of doublet asynchronous cross-peaks with different signs in the (B2, B6/B7), (B3, B6/B7), (B4, B6/B7), (B2, B8/B9), (B3, B8/B9), and (B2, B10/B11) correlation regions in the Fig. 6.3B, 2D asynchronous spectrum, clearly resolve these overlapping bands. However, the cross-peak maxima and minima do not always correspond to the center frequencies of the overlapping Gaussian bands.

In the (B1, B6/B7), (B5, B6/B7), (B1, B8/B9), (B4, B8/B9), (B1, B10/B11), and (B3, B10/B11) correlation regions, the 2D asynchronous spectrum shows only single negative or

positive cross-peaks (Fig. 6.3B). The low values of the correlations in these regions indicate that the correlated bands have similar intensity change rates.

In the (B5, B8/B9), (B4, B10/B11), (B5, B10/B11) and (B5, B12/B13) asynchronous correlation regions, single cross-peaks dominate the entire overlapping band frequency region. The 2D COS asynchronous spectrum does not resolve the underlying overlapping bands.

More complex triplet cross-peaks (positive, negative and positive) are observed in the (B2, B12/B13) and the (B3, B12/B13) asynchronous correlation regions. Triplets of cross-peaks are expected to result from three underlying components instead of the two overlapping Gaussians here. Similar 2D COS results were previously reported by Yu et al.[15] Further complexity is evident in the (B4, B12/B13) correlation region that shows two positive cross-peaks instead of the positive and negative doublet cross-peaks commonly expected.

6.3.2 Modeling of the Effect of Band Overlap on Spectral Normalized Intensity

Yu et al[17] indicates that the normalized band intensities play an important role in determining the 2D COS spectral features. Here we have examined the mechanism of formation of 2D correlation spectra to develop deeper insight.

Given the intensities of two Gaussian bands at frequency ν and at $t=0$, $I_{1,0}(\nu)$ and $I_{2,0}(\nu)$, an intensity matrix can be defined as:

$$I_0(\nu) = [I_{1,0}(\nu) \quad I_{2,0}(\nu)] \qquad (6.9)$$

An intensity change coefficient matrix is defined as:

$$f = \begin{bmatrix} f1 \\ f2 \end{bmatrix} = \begin{bmatrix} f_{1,0} & f_{1,1} & f_{1,2} & \cdots & f_{1,n} \\ f_{2,0} & f_{2,1} & f_{2,2} & \cdots & f_{2,n} \end{bmatrix} \qquad (6.10)$$

where the $f1$ and $f2$ vectors consist of component $f_{i,j}$, which are the intensity change coefficients of the ith band for the jth time or perturbation step. The spectral intensity of the overlapping bands can be calculated as:

$$I(\nu) = I_0(\nu) f = \begin{bmatrix} I_{1,0}(\nu) & I_{2,0}(\nu) \end{bmatrix} \begin{bmatrix} f_{1,0} & f_{1,1} & f_{1,2} & \cdots & f_{1,n} \\ f_{2,0} & f_{2,1} & f_{2,2} & \cdots & f_{2,n} \end{bmatrix} \qquad (6.11)$$

and rewritten as:

$$I(\nu) = [I_{1,0}(\nu) f_{1,0} + I_{2,0}(\nu) f_{2,0} \quad I_{1,0}(\nu) f_{1,1} + I_{2,0}(\nu) f_{2,1} \quad \cdots \quad I_{1,0}(\nu) f_{1,n} + I_{2,0}(\nu) f_{2,n}]$$

(6.12)

For the jth perturbation time step, the normalized intensity at frequency ν:

$$F_j(\nu) = \frac{I_{1,0}(\nu) f_{1,j} + I_{2,0}(\nu) f_{2,j} - I_{1,0}(\nu) f_{1,0} - I_{2,0}(\nu) f_{2,0}}{I_{1,0}(\nu) f_{1,n} + I_{2,0}(\nu) f_{2,n} - I_{1,0}(\nu) f_{1,0} - I_{2,0}(\nu) f_{2,0}} \qquad (6.13)$$

The normalized intensity $F_{i,j}(\nu)$ of a single Gaussian band i at the jth time step would be written:

$$F_{i,j}(\nu) = \frac{I_{i,0}(\nu) f_{i,j} - I_{i,0}(\nu) f_{i,0}}{I_{i,0}(\nu) f_{i,n} - I_{i,0}(\nu) f_{i,0}} = \frac{f_{i,j} - f_{i,0}}{f_{i,n} - f_{i,0}} \qquad (6.14)$$

It can be seen that $F_{i,j}(\nu)$ does not depend on frequency. Eqn. (6.14) can be rewritten as:

$$f_{i,j} = (f_{i,n} - f_{i,0}) F_{i,j} + f_{i,0} = \lambda_i F_{i,j} + \delta_i \qquad (6.15)$$

where $\lambda_i = f_{i,n} - f_{i,0}$ and $\delta_i = f_{i,0}$. Substituting eqn. (6.15) into (6.13), the normalized intensities of overlapping bands at the jth time step can be expressed as follow:

$$F_j(\nu) = \frac{\lambda_1 I_{1,0}(\nu) F_{1,j} + \lambda_2 I_{2,0}(\nu) F_{2,j} - \lambda_1 I_{10}(\nu) F_{1,0} - \lambda_2 I_{20}(\nu) F_{2,0}}{\lambda_1 I_{1,0}(\nu) F_{1,n} + \lambda_2 I_{2,0}(\nu) F_{2.n} - \lambda_1 I_{10}(\nu) F_{1,0} - \lambda_2 I_{20}(\nu) F_{2,0}} \qquad (6.16)$$

Since $F_{1,0} = F_{2,0} = 0$ and $F_{1,n} = F_{2,n} = 1$, then $F_j(\nu)$ can be simplified:

$$F_j(\nu) = \frac{\lambda_1 I_{1,0}(\nu) F_{1,j} + \lambda_2 I_{20}(\nu) F_{2,j}}{\lambda_1 I_{1,0}(\nu) + \lambda_2 I_{2,0}(\nu)} \qquad (6.17)$$

For Gaussian bands with $I_{i0}(\nu) = A_i \cdot e^{-\frac{(\nu-\nu_{ci})^2}{2w_i^2}}$, $F_j(\nu)$ is

$$F_j(\nu) = \frac{\lambda_1 A_1 e^{-\frac{(\nu-\nu_{c1})^2}{2w_1^2}} F_{1,j} + \lambda_2 A_2 e^{-\frac{(\nu-\nu_{c2})^2}{2w_2^2}} F_{2,j}}{\lambda_1 A_1 e^{-\frac{(\nu-\nu_{c1})^2}{2w_1^2}} + \lambda_2 A_2 e^{-\frac{(\nu-\nu_{c2})^2}{2w_2^2}}} \qquad (6.18)$$

The normalized spectral intensity $F_j(\nu)$ is a function of the Gaussian center frequencies, ν_{ci}, bandwidths, w_i, band amplitudes A_i, and λ_i.

6.3.3 Normalized Intensities of Simulated Spectra

Fig. 6.4A shows the time and frequency dependence of the normalized simulated spectral intensities, $F_j(\nu)$. The normalized spectral intensities at the different time steps show somewhat similar profiles, except at *t*=0 and *t*=20 *sec* that are given by horizontal lines of fixed value. The NHI value of $F_{10}(\nu)$ given by $F_{T/2}(\nu) = F_{10}(\nu)$ at *t=10 sec*, is shown in Fig. 6.4B. $F_{T/2}(\nu)$ for each of the non-overlapping B1 to B5 bands have single values that are independent of frequency, except in the wings where the adjacent band intensities begin to dominate. $F_{T/2}(\nu)$ in overlapping band regions is frequency dependent.

Fig. 6.4C compares the time dependence of the normalized spectral intensity, $F_j(v)$ of the non-overlapping band B3 to that $F_j(v)$ of overlapping band B12/B13 at frequencies 2162, 2202 and 2210 cm^{-1}. The normalized spectral intensities $F_j(v)$ monotonically increase with time. The normalized intensities $F_j(2162\ cm^{-1})$ at all times are smaller than those of the B3 band. However, as v increases, the $F_j(v)$ time dependence curve shows an increasing curvature as shown in Fig. 6.4C. The B3 band $F_{B3,j}$ crosses that of $F_j(2202\ cm^{-1})$ (Fig. 6.4C). The normalized intensity time dependence of the B3 band crosses $F_j(v)$ in the B12/B13 overlapping band frequency region, as well as in the other regions that are indicated by the Fig. 6.4B thick black vertical bars.

Fig. 6.4D shows the frequency dependence of the NHI, $F_{T/2}(v)$ in the frequency region between 1830 and 2250 cm^{-1}. In the overlapping B6/B7 frequency region, for $v <$ 1850 cm^{-1}, $F_{T/2}(v)$ has the value associated with NHI of the isolated B6 band $F_{B6,T/2}$. As the frequency increases, the B7 band begins to dominate, and $F_{T/2}(v)$ reaches the maximum value associated with isolated single B7 band.

The B8/B9 and B10/B11 doublet bands overlap more than do the B6/B7 bands. Further, bands B9 and B11 are narrower than are bands B8 and B10 (Table 6.1). The result is that bands B8 and B10 dominate only in the low frequency wings. Thus, the NHI of the overlapping B8/B9 and B10/B11 bands never reach the NHI values of the isolated B9 and B11 bands.

Band B13 is much narrower than is band B12, and their band center frequencies are close (Table 6.1). In areas 3 and 4, B12 dominates, and $F_{T/2}(v)$ has the value of the isolated

band B12, $F_{B12,T/2}$. Between area 3 and area 4 $F_{T/2}(\nu)$ shows a narrower peak due to the narrow B13 band contribution.

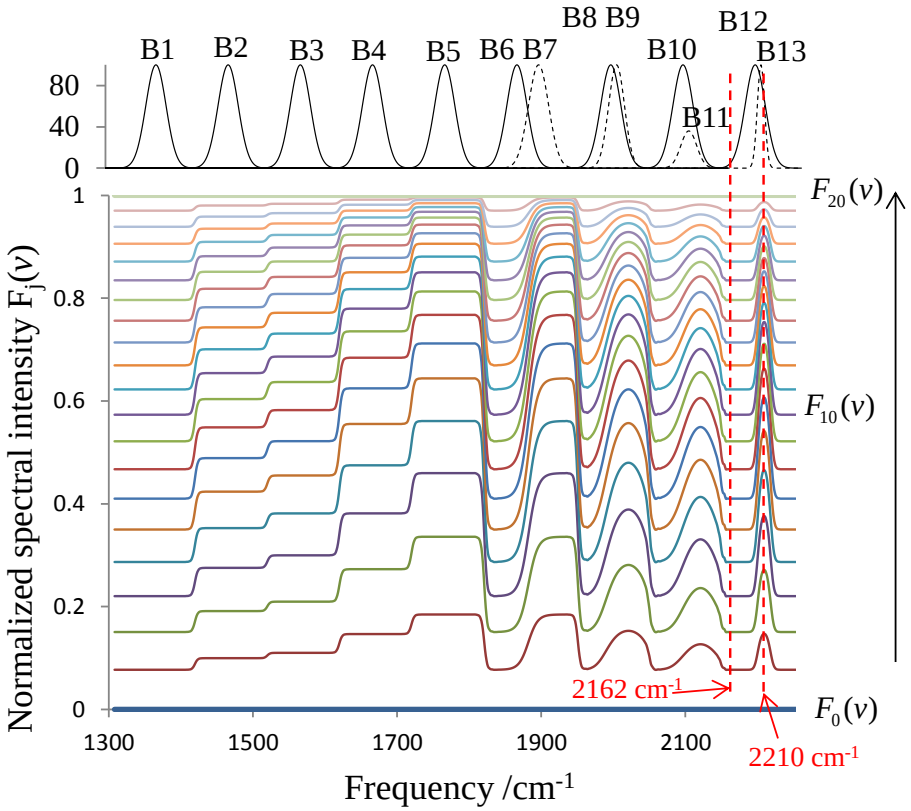

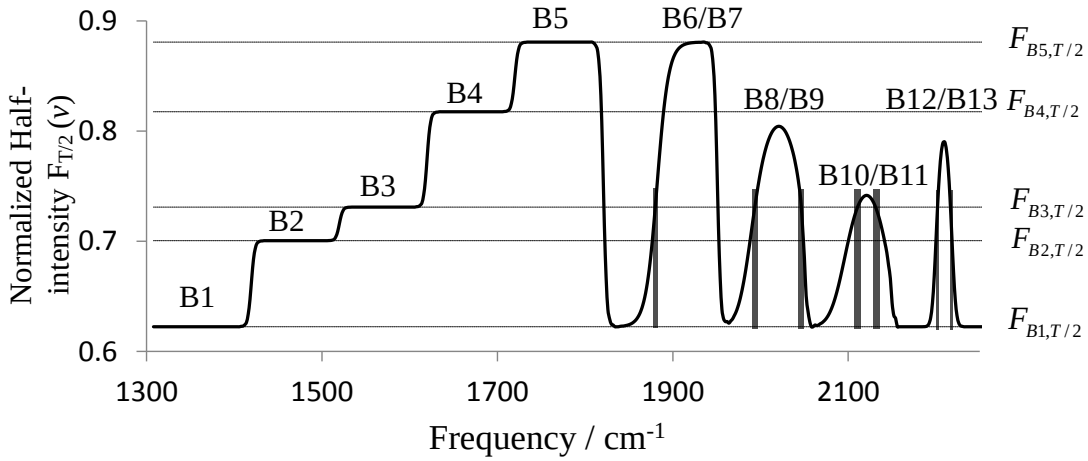

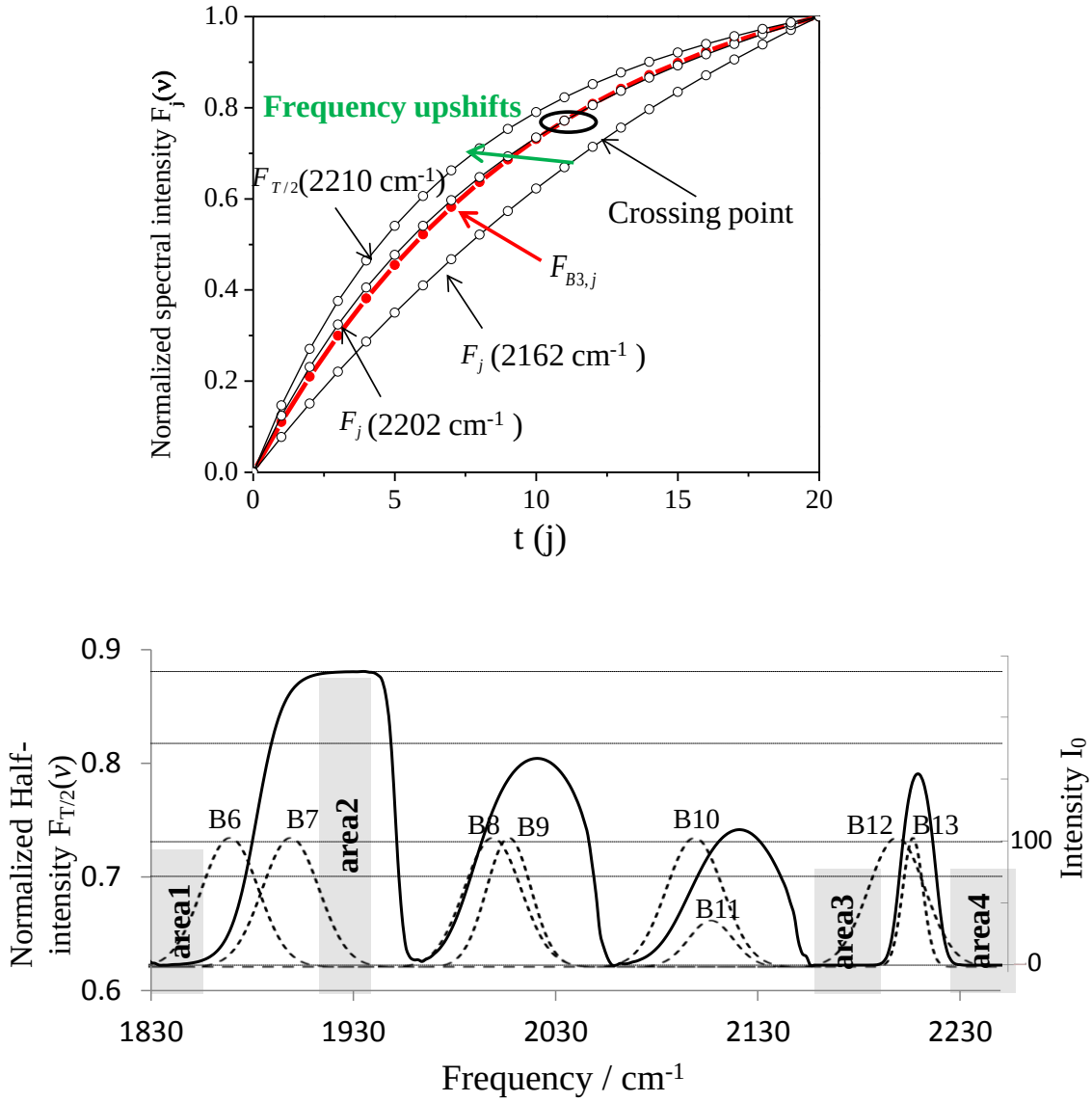

Figure 6.4. (A) Frequency dependence of normalized spectral intensities at different time steps. (B) NHI $F_{T/2}(\nu)$ frequency dependence of the simulated spectra. The five horizontal lines indicate the NHI of bands B1 to B5. The thick black vertical bars indicate spectral regions where the time dependence of $F_{B3,j}$ and $F_j(\nu)$ cross. (C) Time dependence of B3 band $F_{B3,j}$ (1570 cm^{-1}), and of $F_j(\nu)$ at 2162, 2202 and 2210 cm^{-1}. The green arrow indicates the direction of increasing frequency from 2162 to 2210 cm^{-1}. (D) NHI $F_{T/2}(\nu)$ frequency dependence overlaid on the simulated Gaussian bands. The shaded bars indicate frequency regions where bands do not overlap, where single bands dominate.

6.3.4 Interpretation of Asynchronous Spectral Features

Yu and coauthors discussed the relationship between the 2D COS spectra calculated from the original spectra and from the normalized spectra.[17]

$$\Phi(\nu_1,\nu_2) = K(\nu_1)K(\nu_2)\Phi'(\nu_1,\nu_2) \qquad (6.19)$$

$$\Psi(\nu_1,\nu_2) = K(\nu_1)K(\nu_2)\Psi'(\nu_1,\nu_2) \qquad (6.20)$$

Where $K(\nu_i) = I(\nu_i,T) - I(\nu_i,0)$ is the total spectral intensity change at frequency ν_i; $\Phi'(\nu_1,\nu_2) = \frac{1}{m-1}\tilde{F}(\nu_1)^T\tilde{F}(\nu_2)$ and $\Psi'(\nu_1,\nu_2) = \frac{1}{m-1}\tilde{F}(\nu_1)^T N\tilde{F}(\nu_2)$ are the synchronous and asynchronous correlation intensities of the normalized spectra, respectively; m is the number of spectra, $\tilde{F}(\nu_i)$ is the normalized dynamic spectral intensity matrix:

$$\tilde{F}(\nu_i) = \tilde{F}(\nu_i,t) = \begin{bmatrix} \tilde{F}(\nu_i,t_1) \\ \tilde{F}(\nu_i,t_2) \\ \cdots \\ \tilde{F}(\nu_i,t_m) \end{bmatrix} \qquad (6.21)$$

$\tilde{F}(\nu_i,t_j)$ is the normalized dynamic spectral intensity at frequency ν_i and time t_j defined by:

$$\tilde{F}(\nu_i,t_j) = F(\nu_i,t_j) - \frac{1}{m}\sum_{k=1}^{m} F(\nu_i,t_k) \qquad (6.22)$$

Normalization does not affect the relative values of the NHI.[17]

Eqn. (6.20) shows that the asynchronous correlation signs and intensity depend on $K(\nu_1)K(\nu_2)$ and $\Psi'(\nu_1,\nu_2)$. If $K(\nu_1)K(\nu_2)$ is positive, the signs of $\Psi'(\nu_1,\nu_2)$ and $\Psi(\nu_1,\nu_2)$, and $\Phi(\nu_1,\nu_2)$ and $\Phi'(\nu_1,\nu_2)$ are identical. Following Yu's hypothesis,[17] given the positive values of $\Phi(\nu_1,\nu_2)$ and $\Phi'(\nu_1,\nu_2)$ in our case, if the NHI at ν_1 is larger than that at

ν_2, $\Psi'(\nu_1,\nu_2)$ and $\Psi(\nu_1,\nu_2)$ will be positive, while if the NHI at ν_1 is less than that at ν_2, $\Psi'(\nu_1,\nu_2)$ and $\Psi(\nu_1,\nu_2)$ will be negative. If the NHI of the two correlated signals are equal, $\Psi'(\nu_1,\nu_2)=0$. The larger the NHI difference between the two correlated bands, the larger will be $\Psi'(\nu_1,\nu_2)$.[5]

$K(\nu_1)K(\nu_2)$ is the product of the total intensity changes at frequencies ν_1 and ν_2 over the overall perturbation time range. The smaller the intensity changes, the smaller will be the $\Psi(\nu_1,\nu_2)$ correlation intensity. At frequencies with low intensities, $K(\nu_i)\approx 0$, and the correlation intensity $\Psi(\nu_1,\nu_2) \approx 0$. Thus, the correlation intensity maximum occurs at a frequency where $K(\nu_1)K(\nu_2)\Psi'(\nu_1,\nu_2)$ is a maximum. The maximum values of $K(\nu_1)K(\nu_2)$ and $\Psi'(\nu_1,\nu_2)$ occur at frequencies that are not necessarily at the Gaussian center frequencies (Fig. 6.3D). Thus, the maximum value of $K(\nu_1)K(\nu_2)\Psi'(\nu_1,\nu_2)$ will not necessarily occur at the Gaussian center frequency (Fig. 6.3D).

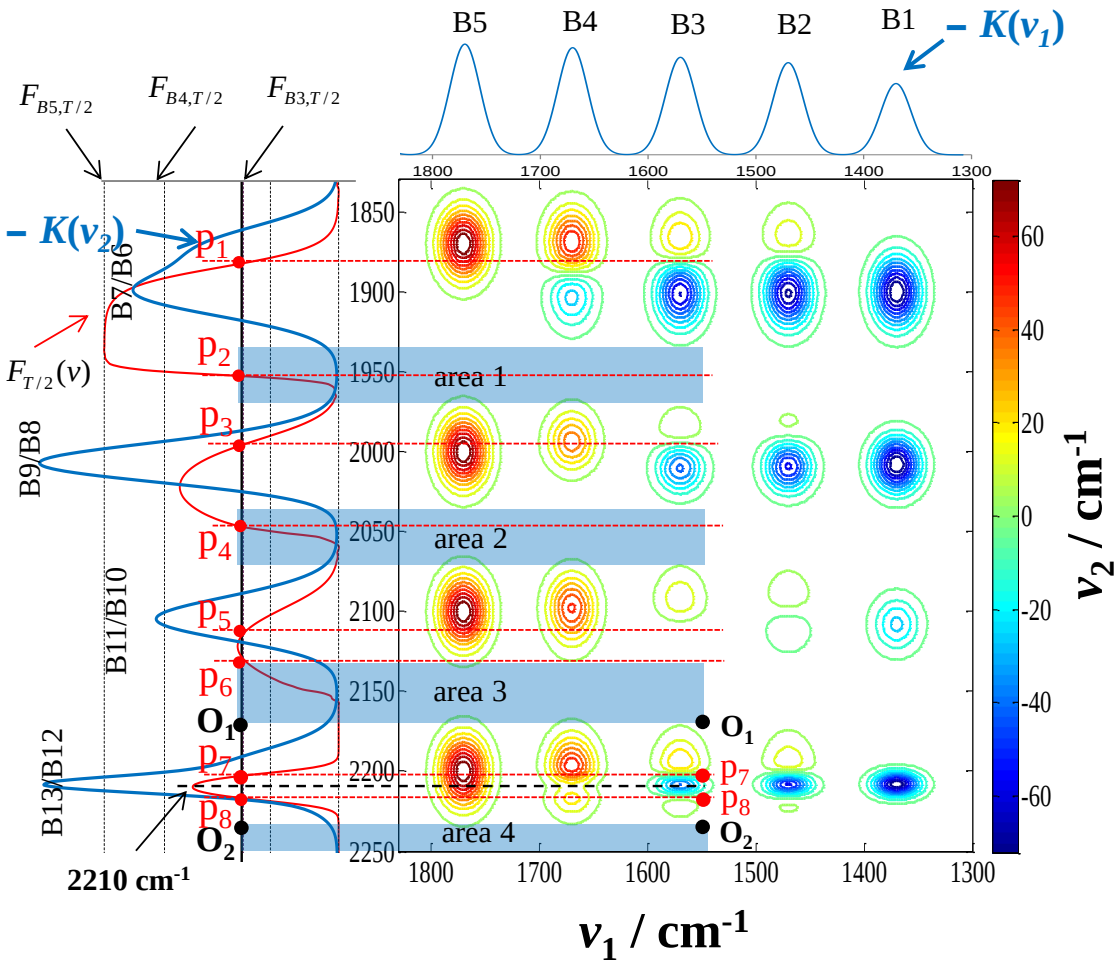

Figure 6.5. Asynchronous 2D correlation spectrum and the NHI frequency dependence, $F_{T/2}(\nu)$. $F_{T/2}(\nu)$ along left vertical axis (red curve) overlaid with the difference spectrum between the simulated spectra at *t*=0 and *t*=20 *sec* ($-K(\nu_2) = I(\nu_2,0) - I(\nu_2,20)$, blue line) in the overlapping band regions. The four horizontal blue shaded areas indicate regions of small $-K(\nu_2)$ values. O_1 and O_2 label the edges of areas 3 and 4. The black vertical line indicates the value of the NHI of the B3 band, $F_{B3,T/2}$. Points p1 to p8, along the black vertical line indicate frequencies where $F_{B3,T/2} \approx F_{T/2}(\nu)$. p1=1882 cm^{-1}, p2=1952 cm^{-1}, p3=1994 cm^{-1}, p4=2046 cm^{-1}, p5=2112 cm^{-1}, p6=2128 cm^{-1}, p7=2202 cm^{-1}, p8=2216 cm^{-1}. The top horizontal spectrum shows the B1 to B5 band difference spectrum between at *t*=0 and *t*=20 *sec* ($-K(\nu_1) = I(\nu_1,0) - I(\nu_1,20)$).

The 2D asynchronous spectral features can be predicted from the calculated NHI and the $K(\nu_1)K(\nu_2)$ values. For example, taking the correlation between the B3 band and the overlapping bands, in the frequency regions [p1, p2], [p3, p4] and [p7, p8], $F_{B3,T/2}$ is smaller than $F_{T/2}(\nu)$ (Fig. 6.5). Thus, given Yu's hypothesis,[17] with a positive value of $K(\nu_1)K(\nu_2)$, $\Psi'(\nu_1,\nu_2)$ and $\Psi(\nu_1,\nu_2)$ will be negative. Asynchronous cross-peaks $\Psi(\nu_1,\nu_2)$ are expected to be positive in frequency regions where $F_{B3,T/2}$ is larger than $F_{T/2}(\nu)$. However, the $K(\nu_1)K(\nu_2)$ values in the four blue shaded areas of Fig. 6.5 are very small, since $-K(\nu_2)$ small. Thus, the correlation intensities $\Psi(\nu_1,\nu_2)$ between the B3 band and the overlapping bands in these areas will be very small.

The asynchronous correlation peak intensities $\Psi(\nu_1,\nu_2)$ also depend on the relative values of $F_{T/2}(\nu)$ and $F_{B3,T/2}$. In the frequency region [p5, p6], $F_{B3,T/2}$ is only slightly smaller than $F_{T/2}(\nu)$. Thus, the 2D correlation will give vanishingly small cross peaks. These conclusions are verified by the calculated 2D asynchronous spectrum.

At frequencies around points p1 to p8 (Fig. 6.5), the time dependencies of the normalized intensities cross that of the band B3 (black vertical bars in Fig. 6.4B). This crossing makes the signs of $\Psi(\nu_1,\nu_2)$ not predictable by Yu et al.'s hypothesis. As shown in Fig. 6.4C, the time dependence curvatures increase as the frequency increases. Thus, the differences in the normalized intensities between the B3 band and overlapping bands between 2162 and 2210 cm^{-1} decrease monotonically ($F_{B3,T/2}-F_{T/2}(\nu)$) as the frequency increases. Thus, the 2D asynchronous correlation intensities $\Psi(\nu_1,\nu_2)$ decrease monotonically: from positive to negative in the frequency range over 2162 to 2210 cm^{-1}. At

frequencies very close to p7=2202 cm^{-1}, the 2D correlation asynchronous intensities will be very small. Similar situations will occur whenever the normalized intensities of correlated bands cross.

Interpretation of the (B3, B12/B13) correlation spectral feature. In the overlapping B12/B13 band frequency region, the B13 band is much narrower than the B12 band, and the separation between these bands is small (Fig. 6.4D). The overlapping B12/B13 band $F_{T/2}(\nu)$ peak has a much narrower bandwidth than does $-K(\nu_2)$ (Fig. 6.5). Between points O_1 and p7 (Fig. 6.5), $F_{B3,T/2}$ is larger than that of the B12/B13 band $F_{T/2}(\nu)$. Thus, the asynchronous cross-peak $\Psi(\nu_1,\nu_2)$ will be positive. In contrast, in the frequency region between p7 and p8, $F_{B3,T/2}$ is smaller than $F_{T/2}(\nu)$, forcing the asynchronous cross-peak $\Psi(\nu_1,\nu_2)$ to be negative. In the frequency region between p8 and O_2, $F_{B3,T/2}$ is again larger than $F_{T/2}(\nu)$. The values of $K_1(\nu_1)K_2(\nu_2)$ are sufficient large to generate a positive cross-peak. Thus, triplet asynchronous cross-peaks are generated in the (B3, B12/B13) correlation region.

Interpretation of the (B4, B12/B13) correlation spectral feature. Fig. 6.5 shows that in the overlapping B12/B13 band region $F_{B4,T/2}$ is always larger than $F_{T/2}(\nu)$. Thus, positive asynchronous cross-peaks will occur. However, since the difference between $F_{B4,T/2}$ and $F_{T/2}$ (2210 cm^{-1}) is small, $\Psi'(\nu_1,\nu_2)$ will be small. Thus, the asynchronous correlation intensity $K_1K_2\Psi'(\nu_1,\nu_2)$ at 2210 cm^{-1} will be weak. The correlation of band B4 with the overlapping B12/B13 bands generates two positive asynchronous cross-peaks, with a minimum between them at 2210 cm^{-1}.

Overlapping band resolution. It can be seen in Fig. 6.5 that all of the overlapping bands are clearly resolved in correlations with the B2 and B3 bands. In contrast, the

correlation with band B5 does not give clear resolution. Good resolution requires that the NHI of a single correlating band have a value between the maximum and minimum of the NHI of the overlapping correlating bands. These observations suggest a useful 2D COS method to analyze highly overlapping bands. Spectral resolution would be enhanced by correlating complex spectra with simulated single band spectra with variable intensity change rates.

6.4 CONCLUSIONS

Our study shows that spectral normalized intensities are important in determining the 2D COS spectral intensities. The signs and number of 2D cross-peaks are related to the normalized half-intensity (NHI) differences and the total intensity changes of the correlated bands. These insights into the origin of the 2D spectral features will help interpret the 2D asynchronous COS spectra. Our results indicate a method to help resolve overlapping bands. This method would correlate the overlapping band regions with a series of discrete bands of different intensity change rates.

ACKNOWLEDGMENT

This work is supported by NIH Grant No. 1R01EB009089.

ABBREVIATIONS USED

2D COS Two-dimensional correlation spectroscopy

NHI Normalized half-intensity

LIST OF SYMBOLS

A_i	Maximum amplitude of the *i*th Gaussian band
f	An intensity change coefficient matrix
f_i	Intensity change coefficient of the band B*i*
$f_{i,j}$	Intensity change coefficient of the *i*th band for the *j*th time step
$F_{i,j}(\nu)$	Normalized intensity of a single Gaussian band *i* at the *j*th time step
$F_j(\nu)$	Normalized intensity at *j*th time step at frequency *v*
$\tilde{F}(\nu_i)$	Normalized dynamic spectral matrix
$F_{Bi,T/2}$	Normalized half-intensity of B*i* band
$F_{T/2}(\nu)$	Normalized half-intensity at frequency *v*
$I_0(\nu)$	Intensities matrix of simulated Gaussian bands at frequency *v.*
$I_{i,0}(\nu)$	Intensities of simulated Gaussian band *i* at frequency *v*
$I(\nu,t)$	Intensity of simulated spectra at frequency *v* and at time *t.*
k_i	Intensity change rate constant of band B_i
K_i	Total intensity change of spectra during the perturbation at v_i
m	Number of spectra collected over perturbation
w_i	Full band width at half height $= 2\sqrt{2\ln 2}w_i$
$y(\nu_i,t_j)$	Measured spectral signal at ν_i and time t_j
$\tilde{y}(\nu_i)$	Dynamic spectral intensity matrix

$\tilde{y}(\nu_i, t_j)$ Dynamic spectral signal at ν_i and time t_j.

λ_i Total change of intensity change coefficient of band B*i* during the perturbation period.

ν Frequency

ν_{ci} Gaussian center frequency

$\Phi(\nu_1, \nu_2)$ Synchronous correlation intensity

$\Phi'(\nu_1, \nu_2)$ Synchronous correlation intensity of normalized spectra

$\Psi(\nu_1, \nu_2)$ Asynchronous correlation intensity

$\Psi'(\nu_1, \nu_2)$ Asynchronous correlation intensity of normalized spectra

6.5 APPENDIX I: SYNCHRONOUS AND ASYNCHRONOUS SPECTRA OF SIMULATED SPECTRA IN THE FULL FREQUENCY RANGE

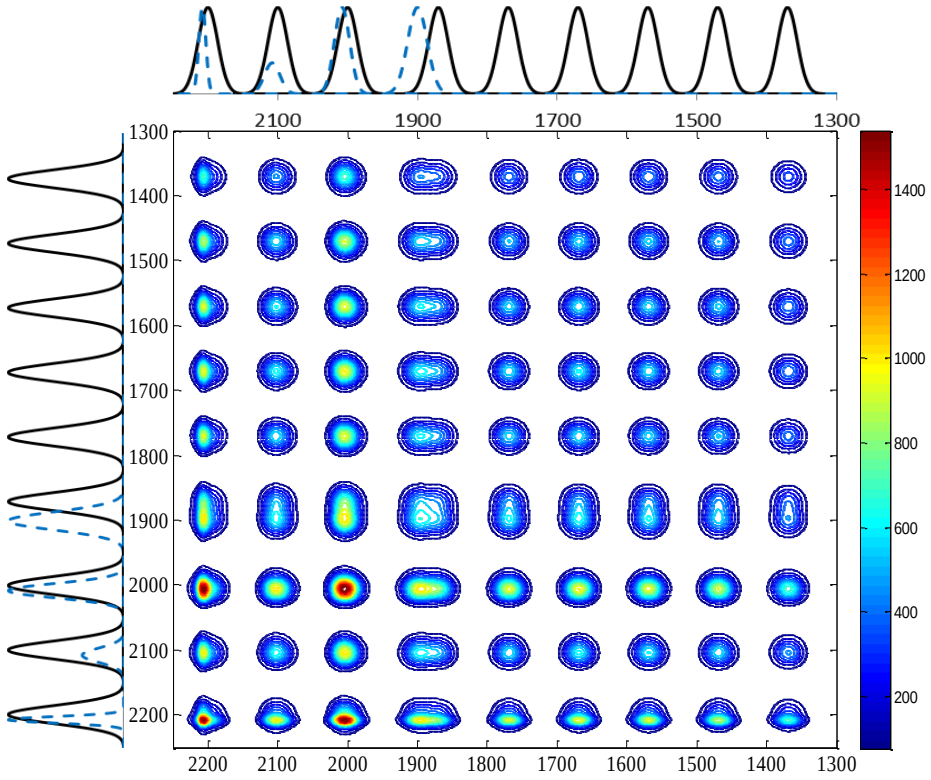

Figure 6.6. 2D COS synchronous correlation spectra generated from simulated spectra shown in Fig.6. 1B in the full frequency range.

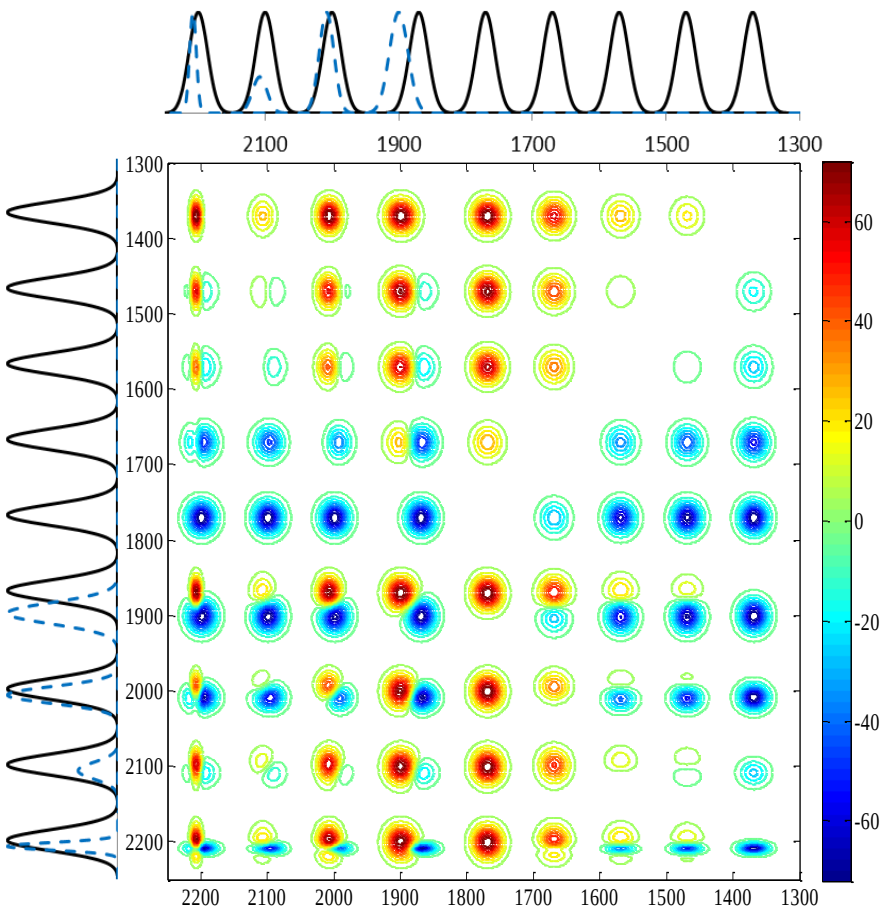

Figure 6.7. 2D COS asynchronous correlation spectra generated from simulated spectra shown in Fig. 6. 1B in the full frequency range.

6.6 APPENDIX II: HISTORY BACKGROUND AND THEORY OF GENERALIZED TWO-DIMENSIONAL CORRELATION SPECTROSCOPY

6.6.1 History Background

Generalized two dimensional correlation spectroscopy (2D COS) has become a versatile and widely used tool for the detailed analysis of various spectroscopic data. This seemingly straight-forward idea of spreading the spectral information onto the second dimension by applying the well-established classical correlation analysis methodology has particular advantage in sorting out the convoluted information content of highly complex sample systems.

2D COS was inspired by the great success of 2D NMR. The desire is to extend 2D NMR powerful concept into general optical spectroscopy applications. However, the practical application of this idea has been limited for a long time, since the characteristic time scale of molecular vibrations is on the order of ps or faster. Direct adaptation of NMR procedure based on pulsed excitations to conventional vibrational spectroscopy becomes available until the ultra-fast optical pulse laser becomes possible in the recent years.

A conceptual breakthough in the development of practical optical 2D spectroscopy was realized for IR studies in 1986 by Noda. [1]It was developed separately from 2D NMR with a significantly different experimental approach, not limited by the manipulation of pulse-based signals. It can detect the various relaxation processes, that are much slower than vibrational relaxations but closely associated with molecular scale phenomena.

However, one of the major shortcomings of the above 2D correlation approach was that the time-dependent behavior of dynamic spectral intensity variations must be a simple

sinusoid. To overcome this limitation, Noda in 1993 expanded the concept of 2D vibration correlation spectroscopy to include a much more general form of spectroscopic analysis, now known as the **generalized 2D correlation spectroscopy**.[4] The type of spectral signals analyzed by the newly proposed 2D correlation method became virtually limitless, ranging from IR, Raman, X-ray, UV-vis, fluorescence, and many more, even to fields outside of spectroscopy, such as chromatography. Perturbations involve a variety of physical origins, such as temperature, concentration, pH, pressure, or any combination thereof. Heter-spectral correlation among different spectroscopic techniques, such as IR-Raman and IR-NIR, has also been developed.

6.6.2 Basic Theory

The detailed background of generalized 2D COS was described in the literature by Noda et al.[4,5] In this appendix, we explain only the basic conceptions and principal of 2D COS.

In a generalized 2D correlation spectroscopy experiment, a series of a perturbation-induced dynamic spectra are collected first in a systematic manner, e.g., in sequential order during a process. Such a set of spectra $y(\nu,t)$ observed as a function of the perturbation variable t (e.g., time, temperature, or concentration) during the interval between T_{min} and T_{max}, is then transformed into a set of 2D correlation spectra by a form of cross correlation analysis. The dynamic spectrum $\tilde{y}(\nu,t)$ of a system induced by the application of an external perturbation is formally defined as

$$\tilde{y}(\nu,t) = \begin{cases} y(\nu,t) - \bar{y}(\nu) & for \quad T_{\min} \le t \le T_{\max} \\ 0 & otherwise \end{cases} \qquad \text{(A6-1)}$$

where $\bar{y}(\nu)$ is the reference spectrum of the system. Reference spectrum is customary to set $\bar{y}(\nu)$ to be the stationary or averaged spectrum given by

$$\bar{y}(\nu) = \frac{1}{T_{\max} - T_{\min}} \int_{T_{\min}}^{T_{\max}} y(\nu, t) dt \qquad \text{(A6-2)}$$

The intensity of 2D correlation spectrum $X(\nu_1, \nu_2)$ represents the quantitative measure of a comparative similarity or dissimilarity of spectral intensity variations $\tilde{y}(\nu, t)$ measured at two different spectral variables, ν_1 and ν_2, during a fixed interval. In order to simplify the mathematical manipulation, $X(\nu_1, \nu_2)$ is treated as a complex number function $X(\nu_1, \nu_2) = \Phi(\nu_1, \nu_2) + i\Psi(\nu_1, \nu_2)$ comprising two orthogonal (i.e., real and imaginary) components, known respectively as the synchronous and asynchronous 2D correlation intensities. The generalized 2D correlation function is defined below

$$\Phi(\nu_1, \nu_2) + i\Psi(\nu_1, \nu_2) = \frac{1}{\pi(T_{\max} - T_{\min})} \int_0^{\infty} \tilde{Y}_1(\omega) \tilde{Y}_2^*(\omega) d\omega \qquad \text{(A6-3)}$$

The synchronous and asynchronous correlation intensities are formally defined in Eq. (A6-3). The term $\tilde{Y}_1(\omega)$ is the forward Fourier transform of the spectral intensity variations $\tilde{y}(\nu_1, t)$ observed at a given spectral variable ν_1 with respect to the external variable t. It is given by

$$\tilde{Y}_1(\omega) = \int_{-\infty}^{\infty} \tilde{y}(\nu_1, t) e^{-i\omega t} dt = \tilde{Y}_1^{\mathrm{Re}}(\omega) + i\tilde{Y}_1^{\mathrm{Im}}(\omega) \qquad \text{(A6-4)}$$

where $\tilde{Y}_1^{\mathrm{Re}}(\omega)$ and $\tilde{Y}_1^{\mathrm{Im}}(\omega)$ are, respectively, the real and imaginary components of the Fourier transform. It is useful to remember that the real component $\tilde{Y}_1^{\mathrm{Re}}(\omega)$ is an even function of T_{min} and T_{max}, while $\tilde{Y}_1^{\mathrm{Im}}(\omega)$ is an odd function. The Fourier frequency ω represents the individual frequency component of the variation of $\tilde{y}(\nu_1, t)$ traced along the

external variable t. According to Eq. (1), the above Fourier integration of the dynamic spectrum is actually bound by the finite interval between T_{min} and T_{max}. The conjugate of the Fourier transform $\tilde{Y}_2^*(\omega)$ of the spectral intensity variation $\tilde{y}(\nu_2,t)$ observed at another spectral variable ν_2 is given by

$$\tilde{Y}_2(\omega)=\int_{-\infty}^{\infty}\tilde{y}(\nu_2,t)e^{+i\omega t}dt=\tilde{Y}_{21}^{\mathrm{Re}}(\omega)+i\tilde{Y}_2^{\mathrm{Im}}(\omega) \qquad \text{(A6-5)}$$

Once the appropriate Fourier transformation of the dynamic spectrum $\tilde{y}(\nu_1,t)$ defined in the form of Eq. (A6-1) is carried out with respect to the variable t, Eq. (A6-3) will directly yield the synchronous and asynchronous correlation spectrum, $\Phi(\nu_1,\nu_2)$ and $\Psi(\nu_1,\nu_2)$.

The above method to calculate the 2-D correlation spectroscopy by Fourier transform is complex. A practical method for computing generalized 2D correlation spectra was presented by Noda, in which the Hilbert transformation was employed.[4,18] The synchronous and asynchronous 2D correlation intensities are then calculated by:

$$\Phi(\nu_1,\nu_2)=\frac{1}{m-1}\sum_{j=1}^{m}\tilde{y}_j(\nu_1)\tilde{y}_j(\nu_2) \qquad \text{(A6-6)}$$

$$\Psi(\nu_1,\nu_2)=\frac{1}{m-1}\sum_{j=1}^{m}\tilde{y}_j(\nu_1)\cdot\tilde{z}_j(\nu_2) \qquad \text{(A6-7)}$$

With the need for a discrete orthogonal spectrum $\tilde{z}_j(\nu_2)$, which can be obtained from the dynamic spectrum $\tilde{y}_k(\nu_2)$ by using a simple linear transformation operation

$$\tilde{z}(\nu_2)=\frac{1}{m-1}\sum_{k=1}^{m}N_{jk}\tilde{y}_k(\nu_2) \qquad \text{(A6-8)}$$

where

$$N_{jk}=\begin{cases}0 & if \quad j=k\\ 1/\pi(k-j) & otherwise\end{cases} \qquad \text{(A6-9)}$$

In the matrix notation, the above dynamic spectra can be written as

$$\tilde{y}(\nu) = \begin{bmatrix} \tilde{y}(\nu, t_1) \\ \tilde{y}(\nu, t_2) \\ \cdots \\ \tilde{y}(\nu, t_m) \end{bmatrix} \qquad \text{(A6-10)}$$

Synchronous and asynchronous spectra can be calculated as follows

$$\Phi(\nu_1, \nu_2) = \frac{1}{m-1} \tilde{y}(\nu_1)^T \tilde{y}(\nu_2) \quad \text{(A6-11)}$$

$$\Psi(\nu_1, \nu_2) = \frac{1}{m-1} \tilde{y}(\nu_1)^T N \ \tilde{y}(\nu_2) \quad \text{(A6-12)}$$

where N is the Hilbert-Noda transformation matrix, given by

$$N = \frac{1}{\pi} \begin{bmatrix} 0 & 1 & \frac{1}{2} & \frac{1}{3} & \cdots \\ -1 & 0 & 1 & \frac{1}{2} & \cdots \\ -\frac{1}{2} & -1 & 0 & 1 & \cdots \\ -\frac{1}{3} & -\frac{1}{2} & -1 & 0 & \cdots \\ \cdots & \cdots & \cdots & \cdots & \cdots \end{bmatrix} \qquad \text{(A6-13)}$$

Simply speaking, the synchronous spectrum is represented by the inner product of two dynamic spectrum vectors measured at two different spectral variable, ν_1 and ν_2, and the asynchronous spectrum is an inner product of the dynamic vectors and its orthogonal Hilbert-Noda matrix.

Fig. 6.8 shows the schematic contour map of synchronous and asynchronous spectra. The synchronous and asynchronous contour spectra consist of positive or negative correlation peaks located at diagonal (autopeaks in synchronous spectrum) and off-diagonal positions (cross-peaks). The synchronous peak develops when the spectral intensity changes synchronously and it reflects that there is strong cooperation or interaction between different

molecular groups. The asynchronous correlation spectra represent the coincidental changes or out of phase changes of the intensity of the two correlated spectra, respectively. The asynchronous cross-peak develops if the Fourier frequency components of the spectral intensity variation have different phases. 2D COS spectra show great advantage in differentiating overlapped bands.

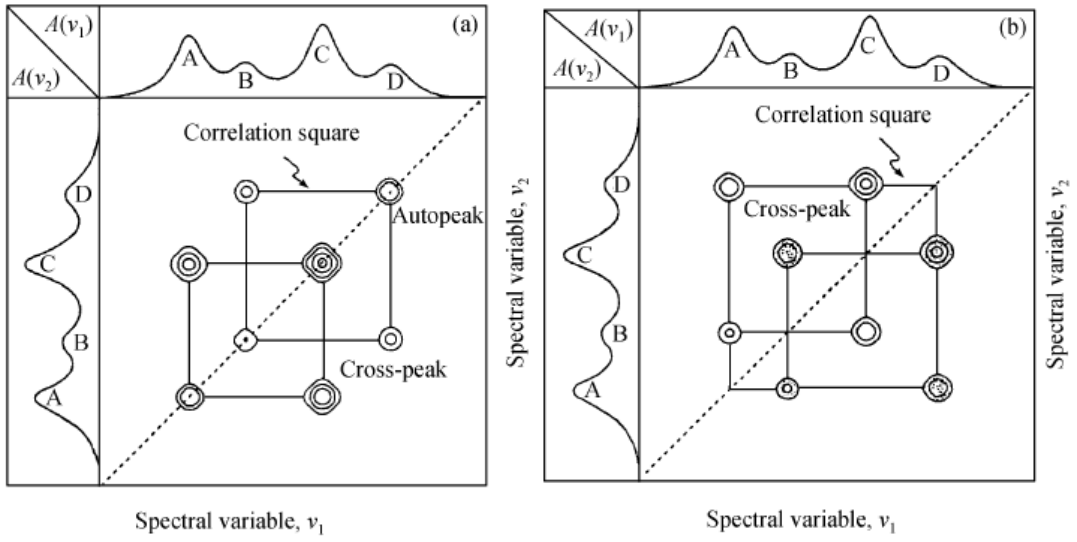

Figure 6.8. Schematic contour map of 2D COS synchronous (a) and asynchronous (b) spectra.[21]

6.7 APPENDIX III: NORMALIZATION DOES NOT CHANGE THE CONCLUSION OF NORMALIZED HALF-INTENSITY ORDER.[19]

As discussed in the main text, the relationship between measured $y(\nu,t)$ and normalized $F(\nu,t)$ spectral intensity is

$$y(\nu,t) = K(\nu)\cdot F(\nu,t) + b \qquad \text{(A6-14)}$$

where $K(\nu) = y(\nu, T_{\max}) - y(\nu, T_{\min})$, and $b(\nu) = y(\nu, T_{\min})$

The normalized dynamic spectral intensity can be derived:

$$\tilde{y}(\nu,t) = y(\nu,t) - \frac{1}{T_{\max} - T_{\min}} \int_{T_{\min}}^{T_{\max}} y(\nu,t)dt$$

$$= K(\nu)F(\nu,t) + b(\nu) - \frac{1}{T_{\max} - T_{\min}} \int_{T_{\min}}^{T_{\max}} \left[K(\nu)F(\nu,t) + b(\nu)\right]dt$$

$$= K(\nu)F(\nu,t) - \frac{K(\nu)}{T_{\max} - T_{\min}} \int_{T_{\max}}^{T_{\min}} F(\nu,t)dt$$

$$= K(\nu)\left[F(\nu,t) - \frac{1}{T_{\max} - T_{\min}} \int_{T_{\max}}^{T_{\min}} F(\nu,t)dt \right]$$

$$= K(\nu)\tilde{F}(\nu,t) \qquad \text{(A6-15)}$$

It shows that the dynamic spectral intensity is proportional to its normalized form.

Substitute Eq. (A6-15) into Eq. (A6-6) and (A6-7), the synchronous and asynchronous spectra are:

$$\Phi(\nu_1,\nu_2) = \frac{K(\nu_1)K(\nu_2)}{m-1} \sum_{j=1}^{m} \tilde{F}_j(\nu_1)\tilde{F}_j(\nu_2) = K(\nu_1)K(\nu_2)\Phi'(\nu_1,\nu_2) \qquad \text{(A6-16)}$$

$$\Psi(\nu_1,\nu_2) = \frac{K(\nu_1)K(\nu_2)}{m-1} \sum_{j=1}^{m} \tilde{F}_j(\nu_1)\tilde{Z}_j(\nu_2) = K(\nu_1)K(\nu_2)\Psi'(\nu_1,\nu_2) \qquad \text{(A6-17)}$$

where $\Phi'(\nu_1,\nu_2) = \frac{1}{m-1} \sum_{j=1}^{m} \tilde{F}_j(\nu_1)\tilde{F}_j(\nu_2)$ and $\Psi'(\nu_1,\nu_2) = \frac{1}{m-1} \sum_{j=1}^{m} \tilde{F}_j(\nu_1)\tilde{Z}_j(\nu_2)$ are named as normalized synchronous and asynchronous correlation intensity, respectively.

The eqn. (A6-16) and (A6-17) show that if $K(\nu_1)K(\nu_2) > 0$, the signs of Φ and Ψ are identical to that of Φ' and Ψ', respectively. If $K(\nu_1)K(\nu_2) < 0$, the signs of Φ and Ψ are both opposite to that of Φ' and Ψ', respectively. As a result, the sign of $\Phi'(\nu_1,\nu_2)\Psi'(\nu_1,\nu_2)$

is the same as that of $\Phi(\nu_1,\nu_2)\Psi(\nu_1,\nu_2)$, so the normalization does not affect the relative values of the NHI.

6.8 REFERENCES

(1) Noda, I. *Bull. Am. Phys. Soc.* **1986**, *31*, 520.

(2) Noda, I. *J. Am. Chem. Soc.* **1989**, *111*, 8116-18.

(3) Noda, I. *Appl. Spectrosc.* **1990**, *44*, 550-61.

(4) Noda, I. *Appl. Spectrosc.* **1993**, *47*, 1329-36.

(5) Noda, I.; Ozaki, Y. *Two dimensional correlation spectroscopy - applicationa in vibrational and optical spectroscopy*; John Wiley & Sons, Ltd, 2004.

(6) Ashton, L.; Czarnik-Matusewicz, B.; Blanch, E. W. *J. Mol. Struct.* **2006**, *799*, 61-71.

(7) Czarnecki, M. A.; Czarnik-Matusewicz, B.; Ozaki, Y.; Iwahashi, M. *J. Phys. Chem. A* **2000**, *104*, 4906-4911.

(8) Noda, I. *AIP Conference Proceedings* **2000**, *503*, 3-17.

(9) Czarnecki, M. A.; Maeda, H.; Ozaki, Y.; Suzuki, M.; Iwahashi, M. *J. Phys. Chem. A* **1998**, *102*, 9117-9123.

(10) Czarnecki, M. A.; Maeda, H.; Ozaki, Y.; Suzuki, M.; Iwahashi, M. *Appl. Spectrosc.* **1998**, *52*, 994-1000.

(11) Ozaki, Y.; Noda, I. *J.Near Infrared Spectrosc.* **1996**, *4*, 85-99.

(12) Noda, I. *J. Mol. Struct.* **2006**, *799*, 2-15.

(13) Noda, I. *J. Mol. Struct.* **2010**, *974*, 3-24.

(14) Shashilov, V. A.; Lednev, I. K. *J. Raman Spectrosc.* **2009**, *40*, 1749-1758.

(15) Yu, Z.; Wang, Y.; Liu, J. *Appl. Spectrosc.* **2005**, *59*, 388-391.

(16) Noda, I. *Appl. Spectrosc.* **2000**, *54*, 994-999.

(17) Jia, Q.; Wang, N.-N.; Yu, Z.-W. *Appl. Spectrosc.* **2009**, *63*, 344-353.

7.0 DISSERTATION SUMMARY

In chapter 3, 4 and 5, by using 204 nm UVRR, we examined the effect of solution environment on the PLL conformation, such as pH, salt and temperature etc.

We examined the impact of $NaClO_4$ on poly-L-lysine's conformational equilibrium. The presence of $NaClO_4$ induces charged PLL to fold into α-helical-like conformations. Extended conformations such as the PPII and 2.5_1-helix conformations dominate the PLL equilibria at low $NaClO_4$ concentrations. In contrast, at higher $NaClO_4$ concentrations α-helical-like conformations that consist of turn, α-helix and π-helix/bulge conformations dominate. We determined temperature dependence of the PLL conformations in the presence of $NaClO_4$. Increasing temperature induces the PLL α-helix and π-bulge/helix conformations melt into extended conformations (PPII and 2.5_1-helix). The conformational population Ψ angle distribution and the Gibbs free energy landscape of PLL were calculated along the Ramachandran Ψ angle folding coordinate.

The pH dependence of PLL UVRR spectra between pH 7.1 and 11.7 cannot be described by a two-state model, but requires at least one additional state. The $AmIII_3$ region fitting with pH 7.1 and 11.7 basis spectra reveals a small pH induced decrease in the relative fraction of the 2.5_1-helix conformation compared to the PPII conformation. We performed a 2D general correlation analysis on the PLL pH dependence UVRR spectra. The cross peaks in the 2D

asynchronous spectrum between the AmIII band and the other bands reveals that increasing pH induces three new structures: π-helix, α-helix and some turn structure.

We examined the effect of NaCl on PLL conformations. We find that even 2.5 M NaCl does not change the equilibrium between the PPII and 2.5_1-helix conformations by screening sidechain electrostatic repulsion.

We examined the PLL hydrogen exchange kinetics at different $NaClO_4$ concentrations. We find that the D/H exchange kinetics of PLL at 0, 0.2, 0.35 and 0.8 M $NaClO_4$ concentrations slow as the $NaClO_4$ concentration increases. Our results indicate that ClO_4^- forms a complex with the lysine sidechains and the PLL backbone to protect it from OH^- exchange catalysis. In addition, $NaClO_4$ binding also slows the conformational exchange between the extended and α-helix-like conformations. These results allow us to determine the association constant of perchlorate to the extended PLL conformation, and allow us to propose a binding geometry.

Hydrogen exchange experiment shows that the hydrogen exchange method combined with UVRR has great potential in investigating protein structure and protein dynamics. The great advantages of this method derive from the structure sensitivity of UVRR spectroscopy, and the significant different between UVRR spectra of protonated and deuterated peptide. This method is also able to determine exchange kinetics of both the extended and helical conformations simultaneously.

Chapter 6 focuses on generalized two-dimensional correlation spectroscopy (2D COS), a widely used mathematical technique. Resolution enhancement in differentiating highly overlapped spectroscopic bands is an important feature of generalized two-dimensional correlation spectroscopy (2D COS). Despite increasing attention given to theoretical and

practical aspects of 2D COS, the origin of the 2D spectral features for overlapping bands and the resolution enhancement mechanisms are not completely understood. In this thesis, we elucidate he 2D resolution enhancement mechanism and the conditions to resolve overlapping bands.

8.0 FUTURE WORK

As we discussed in chapter 3, 4 and 5, two questions remain unsolved. The first question is why high concentration NaCl has negligible impact on PLL conformation at low pH. This is a surprising result. Contrary to PLL system, NaCl increases the α-helical content significantly at pH 7 in the alanine-based, with 3-6 lysine residues inserted peptides models, such as $AcAKAAKAKAAKAKAAKANH_2$.[1] We proposed that Cl^- ion cannot penetrate the space between the neighboring charged lysine sidechains in PLL. However, we did not provide any further test of the hypothesis in the thesis. This hypothesis can be further tested by investigating the NaCl effect on PLL conformation at pH 9-10.5 where PLL sidechains are partially charged, and the average distance between neighboring charged sidechains increases. If the hypothesis is valid, we expect that the presence of NaCl would increase the α-helical conformation content of PLL under these conditions.

The second question is about the detailed mechanism through which the $NaClO_4$ induces α-helical PLL at low pH, but has slight impact on the relative fraction of the 2.5_1-helix compared to PPII conformation. This suggests that the interaction between $NaClO_4$ and PLL is more complicated than ion-pairing between ClO_4^- and the lysine $–NH_3^+$. If the ion-pairing is the only interacting manner, the sidechain electrostatic repulsion will decrease significantly, and 2.5_1-helix conformation relative content compared to the PPII conformation would decrease consequently. Our hydrogen exchange experiment result

suggests that ClO_4^- could interact with sidechain and mainchain simultaneously. More work is needed in order to understand the detailed interaction between $NaClO_4$ and PLL.

Our work shows that the hydrogen exchange method combined with UVRR has great power in studying protein dynamics. Future work for this method involves two aspects: developing a fast mixer and extending the application.

Hydrogen exchange is both acid and base catalyzed, and base catalysis is much more efficient than acid catalysis. Our current hydrogen experiment is limited to the measurements at low pH ~3, where the free amide proton exchange is slow enough to be determined in the time scale of minutes. The hydrogen exchange of the peptide/protein at high pH could be in *m*s or μs and the measurement requires a fast mixer.

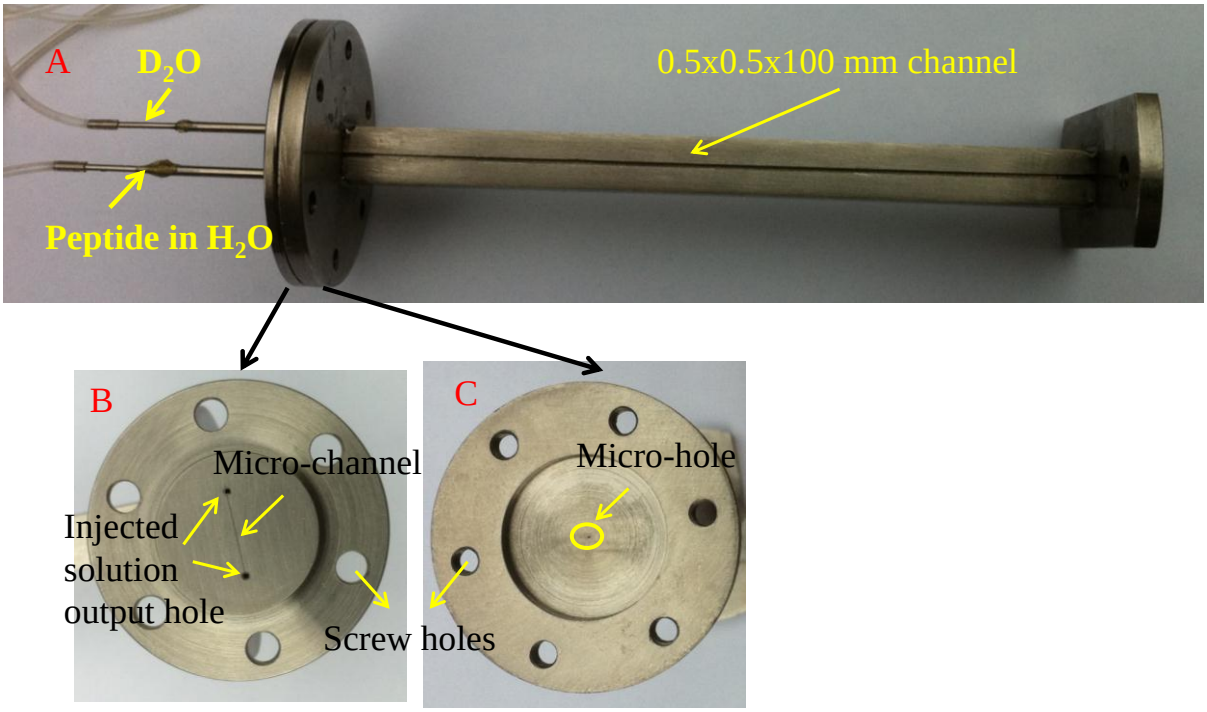

Inside view of the mixer.

Figure 8.1. The fast mixing device made by stainless steel. The two solutions are injected from the top tubings, and the mixed solution flow along a 0.5x0.5x100mm channel. (B) and (C) show the inside view of the mixer. The mixer is composed of two metal plates. The top plate (B) is convex with a 150

(width) x 50 (depth) μm micro-channel connecting two injecting holes, and the bottom plate (C) is concave with a 100 μm micro-hole in diameter in the center. A Teflon piece (not shown) with 1mm hole in the center is put between two plates of mixer to avoid leaking. The two plates are tightened by screws.

We have designed a primary fast mixing device as shown in Fig. 8.1. Two injected solutions are expected to flow in the micro-channel in a turbulent manner with high Reynolds number, and get mixed completely at the point of micro-hole. This mixer has the following advantages: the dead time is in *ms* time scale; the mixed solution is measured along metal channel, and there is no background contribution to the measured sample UVRR spectrum; since the mixer is made in metal, a temperature controller could be mounted on the devices.

The main problem of the current mixer is mixing instability which leads to bad reproducibility. The instability of the mixture directly corresponds to the instability of mixing process, which could be induced by instable flow rate of the solutions in micro-channel. This could be caused by Teflon piece sealed between two plates of the mixer. The stability of the mixer could be improved by removing the Teflon piece and making the mixer sealed directly by two polished plates. The stability of the mixer could also be improved by modifying the mixer parameters including the size of the micro-channel and micro-hole so that high Reynolds number solutions are obtained but generates low mixing pressure.

REFERENCES

(1) Marqusee, S.; Robbins, V. H.; Baldwin, R. L. *Proc. Nat. Acad. Sci. U. S. A.* **1989**, *86*, 5286-5290.